UNIVERSITY OF TWENTE & HYGEAR

Msc Sutstainable Energy Technology
FACULTY OF ENGINEERING TECHNOLOGY, SUSTAINABLE PROCESS TECHNOLOGY

Design and Optimization of a Carbon Capture Process

Author:
R.P.J. Overgaauw
- s2169134
- r.p.j.overgaauw@student.utwente.nl

Professors:
prof.dr.ir. D.W.F. Brilman
ir. E.A. Bramer
dr. M. Mehrali
HyGear Representatives:
ir. Hans ten Dam

Msc Thesis: 201700027 (30 EC)
Duration: 09-09-2024 → 03-04-2025

Abstract

This thesis presents the findings of a model-development study and a design optimization procedure for a Vacuum Swing Adsorption (VSA) cycle, capable of capturing CO_2 from HyGear's Steam Methane Reforming (SMR) flue gas. A previously developed dynamic VSA model has been improved through the addition of an equalization process, which provides the purity benefits of the common blowdown step without its energy requirement and yield trade-off. A mass balance convergence loop has been used to derive a function for the equalization pressure. As a result, the equalization pressure can be predicted given the adsorbent material and operating pressures. The validated model was used to study several influential parameters in the carbon capture process, namely the duration of individual phases, feed composition, feed velocity, and operating pressures. These variables have been tested using Activated Carbon and Zeolite 13X as adsorbent materials. The final design was evaluated based on three performance indicators: ≥80% recovery, food-grade purity (≥99.999%), and an energy consumption less than 150 kWh/-ton CO_2. This design is based on a $CO_2/N_2/H_2O$ mixture, with 12% CO_2 and a relative humidity of 100%. The presented design is also analyzed for its capital and operational costs, to derive a total capture cost in €/ton CO_2 for the system. In practice, the SMR flue gas also contains contaminants as NO_x and SO_x that need to be taken out prior to the carbon capture process. Hence, complementary purification methods are briefly discussed in the context of future process development. Overall, this study contributes to HyGear's broader goal of providing sustainable blue hydrogen.

Contents

1 Introduction

1.1 Global Warming and the Carbon Cycle

When it comes to limiting green house gas (GHG) emissions to reduce climate change, it is possible to identify a number of significant polluting industries. From open-access data study by *Our World in Data* is was found that that 75% of the global emissions is energy related[1]. To avoid irreversible damage done to our planet, numerous countries that are member of the International Energy Agency (IEA) have made zero emission pledges that are summarized in the Net Zero 2050 agreement [2]. These pledges form a call to action for all industrial sectors to research and develop sustainable alternatives for their current business-as-usual activities. In other words, this call to action unites a front of actors to proceed in an energy transition. Besides researching sustainable alternatives it is also important to find the means to limit GHG of all (industrial) emissions that are currently active. For instance, the optional pathways for emission reduction of CO_2 can be illustrated in a carbon cycle diagram as shown in Figure 1. This figure shows how Carbon Capture and Storage (CCS) and Carbon Capture and Utilization (CCU) technologies can affect the overall emissions of a certain industrial process, making it either neutral or positive in its emission rate. In addition, it is also possible to obtain a negative emission rate when applying CCS technologies in a Bio Energy process which is a so-called BECCS process (Bio Energy Carbon Capture and Storage). These pathways for CO_2 emission reduction form the context in which new sustainable technologies are being developed.

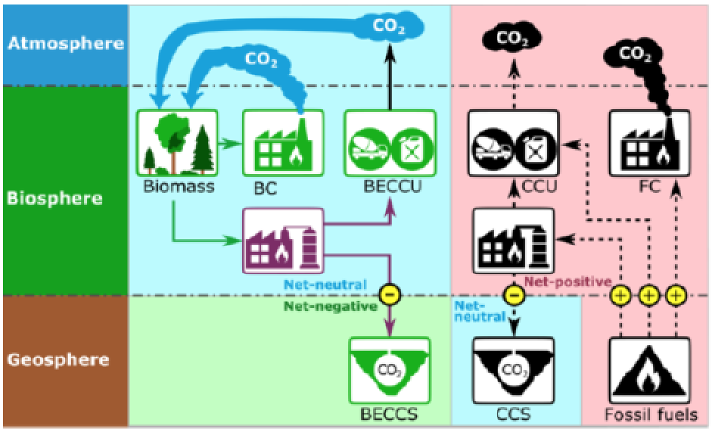

Figure 1: CO_2 emission cycles for fossil fuel and bio-energy industires, showing the net-emission when applying CCS and CCU technologies [3]

As the energy transition suggests, many parties take part in finding alternative energy sources (and fuels) to reach the climate goals of 2050 [2] and maintain energy security in a modern society. An example of such an alternative energy source is hydrogen, if it is produced sustainably. A color-based classification has been developed to categorize any produced hydrogen, depending on the used production technique and its ecological footprint. HyGear builds hydrogen production modules, that use natural gas. This type of hydrogen is labeled as grey hydrogen. In order to provide sustainable hydrogen, HyGear looking to add a carbon capture process to upgrade their grey hydrogen to carbon neutral (blue). For this hydrogen to be classified as blue, the captured carbon can be stored, for example, in salt caverns. Another pathway would be to use the CO_2 as a raw material, for instance by enhancing plant-growth in greenhouses with CO_2-enriched climates. Depending on the end-use of the captured CO_2, it is subjected to an additional liquefaction process or kept as a gaseous product stream.

1.2 HyGear's Hydrogen Production Technology

HyGear is a world leader in the production of on-site hydrogen and strives to produce this with the least amount of CO_2 as possible. One of the most conventional methods to do so is via steam methane reforming (SMR), where steam and hydrocarbons enter a reactor to form CO_2 and H_2[4]. This process is governed by two steps, the first being an endothermic steam reforming step which is done at temperatures around 850°C for optimal conversion [5]. During the steam reforming reaction, methane reacts with water vapor to form both CO and H_2. In the second step, a water gas shift takes place to increase the hydrogen recovery by converting the formed CO into CO_2. These two processes form the two governing reactions of the SMR process, which are written as:

$$CH_4 + H_2O \leftrightarrow CO + 3H_2 \tag{1}$$

$$CO + H_2O \leftrightarrow CO_2 + H_2 \tag{2}$$

The products of this process are fed to another system where hydrogen is separated from the gas mixture. The remaining stream is the so-called off-gas (or tail gas), that contains 20 to 30% CH_4 which is fed to a burner to supply the heat that is required for the SMR process. In order to separate the formed hydrogen from the carbon dioxide, and other unreacted components such as N_2, CO, or CH_4, HyGear uses a pressure swing adsorption (PSA) process. This process exploits the physical driving force of a species to adsorb onto the surface of an adsorbent material. With this technology, the heavier components are adsorbed and the lighter hydrogen is passed through the system. A flow diagram of a typical SMR process is shown in Figure 2. On the other hand, the remaining flue gas (released in the burner/reformer and when regenerating the adsorbent material) still releases CO_2 into the atmosphere. This is roughly 9 kg of CO_2 per kg of formed H_2[4]. In current SMR systems 60 till 75% of the total CO_2 is produced in the water gas shift and 40 to 25% in the burner during the reforming step [6],[7]. In the light of meeting the Net Zero emission goals it is, therefore, important to find ways to capture this stream of CO_2. Besides the environmental perspective, capturing carbon from an SMR process has also three economic benefits. The captured CO_2 can be sold as a product to several industries, the "grey" hydrogen is upgraded to "blue" hydrogen increasing its worth, and the avoided emissions can be sold as a tradable commodity through the introduced Emission Trading System[8].

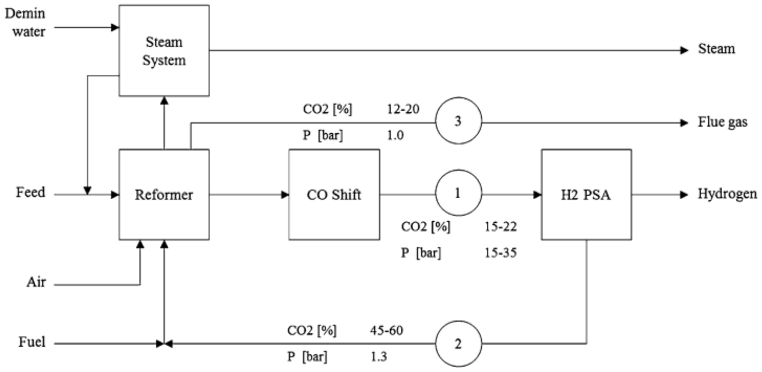

Figure 2: Overview of the SMR process, showing the pressure and CO_2 concentration of three potential streams to capture CO_2 from[9]

As a means to capture this CO_2, HyGear has developed an effective and efficient technology using a vacuum swing adsorption (VSA) process. In this process, CO_2 is adsorbed at atmospheric pressure and desorbed under lowered pressures to partial vacuum levels. The two adsorbent materials that are mostly researched by HyGear are Activated Carbon (AC) and Zeolite 13X (Ze13X). The proof of concept has already been demonstrated. The next phase, in upgrading their produced hydrogen to blue hydrogen, involves designing and optimizing the entire carbon capture system to reduce energy consumption while maximizing process recovery. As such this research focuses on designing and refining the VSA system to capture CO_2 from the flue gas and upgrade it to food-grade purity (>99%), making it a valuable and marketable product.

1.2.1 Development Challenges

HyGear provides its technological solutions as ready-to-use products, as shown in Figure 3, hence there is a priority in getting the technology integrated whilst maintaining performance, cost, energy efficiency, and space. On the other hand, this CO_2 capture technology could also be used as a stand-alone product that is applicable for flue gasses of similar composition as that of the SMR process. Developing a technology that can solve multiple problems is also beneficial from a business perspective. Therefore, it is of interest to find out which flue gas types could be of interest for HyGear's CO_2 capture technology. The typical SMR flue gas composition is given in Table 1, which forms the base-case for this research.

Table 1: Component based minimum and maximum concentrations in typical SMR flue gas streams

	CO_2	**N_2**	**O_2**	**H_2O**	**SO_x**	**NO_x**	**CO**
min %	10	70	2	10	0.005	0	0
max %	15	75	5	15	0.015	0.001	0.1

However, applying carbon capture technology to other flue gasses, such as those of post-combustion processes, likely require preliminary gas purification steps. Purification of e.g. NO_x and SO_x from the gas stream is important as these gasses may hinder the performance of the carbon capture process or damage the equipment. Hence, it is important to research applicable purification technologies when assessing the feasibility of the carbon capture technology in a broader context.

1.3 Current state of Development

Regarding carbon capture methods, current technologies can be categorized as either pre-combustion, oxy-fuel combustion, or post-combustion capture technologies all of which have gained attention. From these three, HyGear's VSA technology can be used as either a pre- or post-combustion process. The three applicable gas streams from which CO_2 can be captured are shown in Figure 2; 1. the syngas after the water gas shift, 2. the off-gas before it is fed to the burner/reformer, 3. the flue gas of the system.

Out of these streams, the first two are pre-combustion streams and the third is a post-combustion stream. Comparisons between these streams and their carbon capture potential (and respective costs) are often researched [9]. The concentration (and partial pressure) of CO_2 in pre-combustion gas streams is generally higher than that of post-combustion streams, as is also shown in Figure 2. A higher CO_2 concentration has a positive effect on the driving force for mass transfer and also on the equilibrium loading (capacity) of the adsorbate or solvent before saturation[10], consequently making the separation process easier. Although this may bring advantages in the energy requirements and efficiency, pre-combustion gas separation also brings challenges for the combustion process. For example, lowering the CO_2 content in a combustion process may favor the formation of NO_x which requires significant modifications to avoid.

Regarding the three potential streams, this means that capturing CO_2 out of stream 1 or 2 would require changes in hydrogen purification step (which is also a pressure swing adsorption step) and/or the reformer/burner. For the flue gas stream (stream 3) there are no additional changes required, which is also beneficial with regards to HyGear's commercialization plans. Another advantage for selecting the flue gas stream, is that it has the highest mass flow of CO_2 and, theoretically speaking, 100% of the CO_2 can be removed. Hence, post-combustion methods will be the main scope when analyzing the current state of development.

1.3.1 Post-Combustion Carbon Carbon Capture

Regarding post-combustion carbon capture processes, the four most common methods are adsorption, absorption, cryogenic distillation and membrane processes each having their own benefits and challenges[11],[12]. During absorption the CO_2 is absorbed into a liquid solvent, either by a physical driving force (Physical Absorption), or by undergoing a chemical reaction (Chemical Absorption). During absorption, CO_2 is dissolved forming carbamates and bi-carbamates until saturation/equilibrium. Available literature shows that the most mature CO_2 absorption technique that is suitable for large-volume industrial applications, is chemical absorption with amine based solvent: mono-ethanolamine (MEA)[11],[10]. Solvents are selected based on their selectivity to CO_2 over other gasses (e.g. N_2, O_2, NO_x, SO_x). With respect to this technique, its main drawbacks are related to the heat capacity of the in water dissolved solvent causing high energy requirements during the regeneration step. Furthermore, corrosion effects and solvent degradation through oxidation, or thermal processes, are additional challenges which researchers are trying to solve[13]. Available studies also show the potential of amine solvents to loose CO_2 absorption capacity due to accumulation on the amine compounds [14]. Both of these issues require solvent regulation, which is done by periodic injection/addition of new solvent into the installation/column. Part of the solvent is also lost in the exhaust of the solvent, due to evaporation, since amine compounds are volatile, releasing the CO_2 lean flue gas with additional harmful amine compounds into the environment[15]. This issue solved by subjecting the flue gas to a water wash step, in order to re-absorb the amines, but consequently increasing the system's complexity.

Figure 3: Example of Hygear's container packed products that allow for easy installment[16]

Cryogenic CO_2 separation processes use differences in phase transition at given temperatures and pressures, allowing CO_2 to be separated though cooling (below dew point) & condensation. Cryogenic distillation as an industrial post-combustion separation process, has a disadvantage because it is unsuitable when vast amounts of impurities and incondensable gasses are present. For such cases, an alternative but more complex method is to subject a liquefaction process and purge non-condensable gasses. Furthermore, these processes have a high cooling duty making them also unfavorable from an economical perspective.

In the context of membrane based CO_2 capture methods, the separation process is based on the permeability of the membrane. Different gasses have varying permeabilities (transport factors) for a given membrane, and the ratios of these permeabilities formulate the selectivity of the membrane (e.g. membranes with high permeability have faster cycle times but decreases the purity, and high selectivity membranes have higher purities but the process takes longer and requires more area to handle the feed stream). The selectivity (separation factor) for different gasses is influenced by the membrane's pore size, molecular size and weight of the gasses, as well as the affinity of the gas molecules to the membrane material: polarity, ability to have chemical interections like hydrogen-bonding, and solubility[17]. Gas permeability and selectivity, are inversely related and therefore form a trade-off in the R&D process of an optimal membrane.

Membrane separation technology is especially well developed in liquid separation applications. In the context of post-combustion carbon capture, membrane based gas separation mainly involves CO_2/N_2 (which would be H_2/CO_2 for pre-combustion)[17] where the most common mechanisms are membrane size sieving (using variations in the kinetic diameter of gasses) and solution-diffusion (exploiting differences in gas-to-membrane interactions). To give an example; membrane selectivity between CO_2/N_2 can be favored towards CO_2, by using polymers with polar groups as a membrane material to increase the CO_2 solubility (since CO_2 is slightly polar and N_2 is not). In addition, the kinetic diameter of CO_2 is smaller (0.33 nm) than that of N_2 (0.364 nm) favoring the diffusion of CO_2.

One of the main challenges for post-combustion CO_2 membrane separation, is that the CO_2 is present at low concentrations $\approx$15%, thus low partial pressures, which gives a low driving force for its permeability. This low partial pressure forms an issue as the membrane's performance is highly dependent on the partial pressure gradient of CO_2 and the other components gas stream. In these dilute scenarios, the membrane surface area and pressure differences over the membrane sides (pressurizing the feed gas) are increased to enhance separation performance, although this increases the overall costs and energy consumption[18]. To meet the purity and recovery targets membrane systems often consist of multiple stages. The last major challenge for membrane based separation deals with the impurities present in flue gas streams. These impurities cause fouling or degradation which requires membrane replacements or cleaning. As membranes are costly to make this forms another costly aspect to this process.

During adsorption, the adsorbate is adsorbed onto the surface of the adsorbent material through either physical interactions (e.g. Van Der Waal forces) or chemical interactions (e.g. chemical reactions forming covalent bonds). This method is effective for separation processes in dilute mixtures, as is the case for CO_2 capture out of SMR- and post-combustion flue gasses[19]. Out of the two, physical adsorption is favored as this process generally has a lower heat of adsorption which results in a lower energy consumption during the regeneration step. This heat of adsorption is also a measure of the component's affinity to the adsorbent material. The affinity of a component to the adsorbent material depends on the temperature. As the adsorption step is exothermic, the adsorption capacity is better (at a given pressure) for colder temperatures. Consequently, it may be required to cool the flue gas to ambient temperatures depending the feed conditions.

The regeneration step, to recover the adsorbed CO_2, is performed by either a swing in pressure, temperature, or both. In pressure swing systems, the adsorption step takes place at elevated pressures since adsorption capacities are higher at high pressures. The desorption step is then initiated by lowering the pressure, releasing the adsorbed CO_2 as a pure product stream. For a temperature swing, the adsorption takes place at low temperatures and the adsorbed CO_2 is released by elevating the temperature (favoring the endothermic side of the process). After the desorption step, the column has to be cooled again to return to optimal adsorption conditions. The heat/energy required for a temperature swing is generally costlier compared to a pressure-swing, and also has longer cycling times as the heating/cooling process takes longer than the pressure change[20]. The third method is a vacuum swing, where the adsorption takes place at near-ambient pressures and the CO_2 is released by lowering the pressure using vacuum pumps. This process allows for a simpler design and requires less energy than a pressure swing, knowing that the flue gas is at atmospheric pressure.

Due to the absence of water, in comparison to absorption, the heat/energy required for regeneration is much lower (lower heat capacity of the adsorbent). The lower heat capacity, and the fact that physical adsorption onto a surface does not chemically alter the adsorbent the way an amine-solvent is chemically altered, also brings a benefit of generating less secondary waste, because solvents generally degrade quicker than adsorbents[15]. Knowing that the there is little waste heat to use from the SMR process, in combination with the review of the optional techniques gives that adsorption via vacuum swing is the most applicable carbon capture method for the SMR flue gas.

1.4 Problem Definition and Research Goals

When looking at HyGear's business perspective and the current state of carbon capture technologies, it is clear that there is a potential market for carbon capture modules in systems such as steam methane reforming (upgrading the production of grey hydrogen, to carbon-neutral blue hydrogen). However, finding optimal designs and operating conditions for such systems is a difficult task. This signifies the importance of developing a dynamic model, capable of describing the adsorption/desorption cycle as a whole system to aid the development of this technology. Development of such a dynamic model has been initiated in previous research. In continuation of those efforts, the aim of this thesis is to perform a parameter study of the PSA process using the developed model and implement potential improvements. Having identified the most influential parameters, and their relation to the capture performance and energy consumption, it is possible to design an optimized PSA system for capturing CO_2 from the SMR flue gasses. The optimization is based on a set of performance indicators in terms of purity, recovery, and energy demand, targeting to reach:

- purity $\geq$ 99.999% (food-grade)
- recovery $>$ 80%
- energy demand $\leq$ 150 kWh/ton CO_2

Similar research and simulations are performed by HyGear on a daily bases using DWSIM, hence this tool will also be used for this thesis. The dynamic carbon capture process itself is programmed in Julia. Knowing that that there is a market for post-combustion carbon capture in general, a secondary objective is to analyze the system's commercial potential by defining the operational limit of the CO_2 inlet concentration. Defining this operational limit helps to identify for which flue gasses, and thus markets, this carbon capture system is attractive. Different flue gasses may also contain different components, like NO_x and SO_x, that can decrease the system's performance. Since the carbon capture process is the main scope of this research, literature based recommendations on potential NO_x and SO_x purification techniques are provided in Appendix A.4.

Achieving the discussed goals is done by following a research plan that divides the overall research goal into smaller steps. The used research plan is formulated below:

Research & Development

- Gain understanding in the conventional separation techniques, and their respective advantages & challenges.
- Describe the governing mechanics involved in vacuum swing adsorption processes and identify the most influential parameters.
- Research possible improvements that can be implemented to the model, as a means to reach the specified performance indicators.
- Implement the improvements and validate the model.
- Test and clarify the relation of important parameters to the carbon capture performance and energy consumption for the analyzed adsorption cycles.
- Present findings of the parameter study for the adsorption cycles and propose an optimized design for the carbon capture system.

Future Outlook

→ Discuss possible improvements on the model and/or other adsorption cycles that might have better carbon capture performances.

→ Provide a range of applicable feed compositions through a sensitivity study of the CO_2 flue gas concentration.

All in all these goals/steps form a chronological order which is followed during this study. Subsequently, these goals are addressed in dedicated sections throughout this report. Combined, this research aims to answer one main research question:

"Which system design, using vacuum swing adsorption, is capable of capturing CO_2 from HyGear's steam methane reforming flue gas in an energetically efficient manner ($\leq$150 kWh/ton CO_2) whilst achieving food grade purity CO_2 and high recovery ($\geq$80%), and what is the operating range for the inlet concentration of CO_2 at which the system's performance is maintained?"

2 Theoretical Background

This section covers the fundamental principles that are essential for understanding physical adsorption and characteristic aspects for Vacuum Swing Adsorption (VSA) processes. Moreover, material properties and requirements for the adsorbent are also discussed. In doing so, the governing mechanics involved in vacuum swing adsorption processes are described and most influential parameters are identified which will be studied in a later stage. Lastly, the current state of the VSA model will be covered and possible improvements will derived based on available literature.

2.1 Physical Adsorption Principles

As mentioned in the introduction, physical adsorption is based on the difference between molecules in adsorbing onto a surface of a specific material. For physical adsorption, the predominant forces are Van Der Waals forces; dispersion-repulsion forces and electrostatic interactions through polarity[19]. As the affinity of a molecule to adsorb onto an adsorbent's surface increases, so does the heat of adsorption released during this (spontaneous and thus exothermic) process. This relation forms an important aspect in designing and optimizing an adsorption process, because a better adsorption, therefore, also increases the energy requirement for the desorption step. Another effect to take into a count, is that the heat released during adsorption reduces the adsorption rate. Following Le Chatelier's principle, it can be explained that for an increase in temperature the endothermic reaction (desorption) is increasingly favored.
Efficient physisorbents are highly porous and can reach up to an effective surface area of 100 up to 1200 m^2/g[21]. The adsorption process is driven by a concentration gradient and continues, at a given temperature, until an equilibrium is reached (saturation). Such equilibria are described by adsorption isotherms. In the context of carbon capture, these isotherms show the relation between the gaseous CO_2 concentration expressed in partial pressure and the amount of adsorbed CO_2 expressed in mass CO_2 adsorbed per unit mass of adsorbent[19]. The shape of the isotherm depends of the interactions between the adsorbent material, CO_2, and other present gasses, which depend on both the properties of the material and the gasses in the mixture. These properties are further discussed in Section 2.2, where these are matched with the carbon capture process to select the most suitable adsorbents.

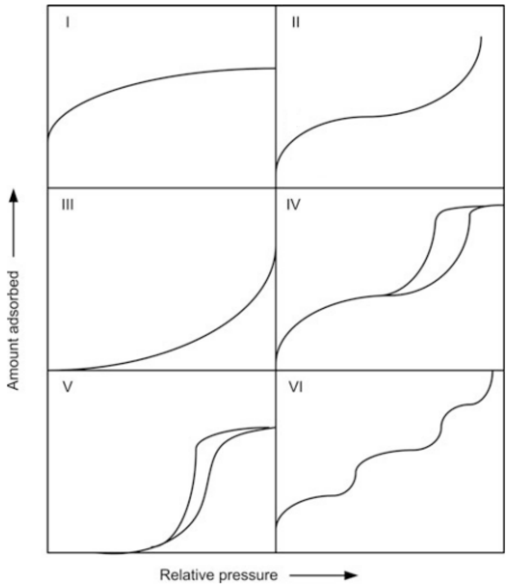

Figure 4: Sorption isotherm types according to IUPAC classification [22]

According to the IUPAC classification[22] for sorption isotherms, there are six isotherm types shown in Figure 4. Those that are related to this study are of type I, which are reversible isotherms where adsorption is limited to a monolayer on the surface. In addition, also type IV is of interest as the adsorption of water vapor shows this relation: after having filled a monolayer also multiple layers adsorb onto the surface, and hysteresis may occur due to capillary condensation into the adsorbent material[23]. The mostly used model to describe the type I adsorption isotherm is the Langmuir model. The Langmuir model is based on fractions of available and occupied adsorption sites on the adsorbent's surface, whilst assuming that lateral interactions do not take place in the monolayer of adsorbed species, that the heat of adsorption is constant, and that adsorption sites are homogeneously distributed over the surface. For a single species isotherm is described by:

$$\theta = \frac{q}{q_m} = \frac{bp}{1+bc} \tag{3}$$

where θ is the fraction of available sites, which is fraction of the adsorbent loading, q, divided by the maximal adsorbent loading q_m (for a monolayer). In the right hand side fraction, c is the adsorbates gaseous concentration in mol/m^3 (for this case CO_2) and b is the ratio of the adsorption and desorption rate constants; k_a/k_d.

2.2 Adsorbent Selection

As means to achieve effective and efficient CO_2 capture it is important to use a carefully selected adsorbent material. This selection is based on a material's CO_2 uptake capacity, selectivity, ease of regeneration (heat of adsorption), stability, durability, operating conditions, and costs[19]. To asses the feasibility of an adsorbent material it is important analyze the kinetic and electrostatic properties of gasses commonly present in steam methane reforming processes, because these properties provide information on the adsorbent-gas interactions plus the material's selectivity towards CO_2. Four important properties are shown in Table 2. The Kinetic Diameter of a gas is a measure of its effective size. For example, when there are significant differences in kinetic diameter it is useful to match the pore sizes of the adsorbent material with the gas of interest to increase the adsorbents selectivity. For this context, the kinetic diameters are relatively similar which indicates that the separation process cannot depend on size selectivity alone. However, what can be noted from the magnitude of the kinetic diameters is that the suitable adsorbent materials will likely have a microporous or mesoporous structure (micropores <2nm & mesopores 2-50nm & macropores >50nm)[24]. This is due to the interest in reversible isotherm behavior forming a monolayer, whereas macroporous materials often show multilayer behavior seen in isotherms of type II and IV in Figure 4[19].

Table 2: Kinetic and electrostatic properties of common gasses [19]

Molecule	**Kinetic diameter (nm)**	**Dipole moment (Debye)**	**Quadrupole moment (10^{-40} C m^2)**	**Polarizability (10^{-24} cm^3)**
CO_2	0.330	0	-13.71, -10.0	2.64, 2.91, 3.02
N_2	0.364	0	-4.91	0.78, 1.74
O_2	0.346	0	-1.33	1.57, 1.77
H_2O	0.280	1.85	6.67	1.45, 1.48
SO_2	0.360	1.63	-14.6	3.72, 3.89, 4.28
NO	0.317	0.16	-6.00	1.7
NO_2	0.340	0.316	–	3.02
CO	0.376	0.11, 0.37	-8.33, -6.92	1.95, 2.19
H_2	0.289	0	2.09, 2.2	0.81, 0.90
CH_4	0.380	0	0	2.6

Given the range of pore sizes of micro- and mesoporous adsorbents it is clear that the kinetic diameters of the gas species are much smaller. Hence the adsorption process is not kinetically controlled (diffusion through the pores is easy), but equilibrium controlled. Therefore, the temperature and partial pressures of the gasses will determine the adsorption process & capacity.

The differences in equilibria for adsorbate-adsorbent interactions, so-called equilibrium effects, are governed by electrostatic properties of the involved molecules and operation conditions. The dipole moment of a gas is the magnitude of a molecule's charge separation or polarity; the unevenness of the charge distribution. An uneven charge distribution, due to differences in electronegativity of atoms, means that there are partially positive and negative charges present in the molecule which are so-called poles. CO_2 has no dipole moment, since the linear symmetrical structure causes the polar C=O bonds to cancel out[19]. This means that the adsorbent materials which highly depend on charge selectivity (electrostatic attractions) will have a lower CO_2 adsorption in the presence of water vapor or impurities such as SO_2 and NO_x that do have strong dipole moments. Although the polarity of CO_2 is canceled out due to symmetry, the charge is still unevenly distributed which translates to a high quadrupole moment which is greater than that of the other gasses. Hence, an adsorbent that relies on electrostatic interactions with high quadrupole moments is suited for CO_2 when polar molecules, such as water vapor or impurities such as SO_2 and NO_x, are absent. Lastly, the polarizability is a measure of the ease with which a molecule's electron cloud can be distorted. High polarizability, which CO_2 has, enhances Van der Waals forces with the adsorbent material. This is another potential aspect that can improve CO_2 adsorption.

Using the latter information, it is worthwhile to evaluate the mostly researched (and used) adsorbent materials. In addition, it may be noted that the material selection involves a trade-off between crystalline and amorphous adsorbents [25]. Due to their stable lattice structure, crystalline materials have a distinct pore structure that may have a significant adsorption capacity. Through lattice alterations, it is possible to regulate the distribution and size of the pores to only let smaller molecules pass through (molecular sieving effect). Whereas, amorphous materials are very porous with large surface areas due to the lack of structure. This is a benefit in the context of CO_2 adsorption, although it also has a downside since amorphous materials may have lower stability and selectivity properties. Table 3 contains typical characteristics for adsorption materials. These, and other types of materials, are discussed below.

Table 3: Overview of typical adsorbent material properties [19],[26],[25]

Adsorbent	**Pore Diameter (nm)**	**Adsorption Temperature (°C)**	**CO_2 pressure (bar)**	**CO_2 Adsorption Capacity (mmol·g^{-1})**	**Heat of Adsorption (kJ/mol)**
Activated Carbon	1 - 2.5	25	1	1.5 - 4.8	15 - 30
Carbon Molecular Sieves	0.3 - 0.9	25	0.5	0.9 - 4.9	20 - 40
Silica Gel	2.2 - 2.6	25	1	0.8 - 4.8	10 - 25
Zeolites	0.8	25	1	0.75 - 4.66	40 - 65
Metal Organic Frameworks	0.4 - 2.4	25	0.5	0.6 - 7.2	20 - 50

Activated Carbon (AC) is traditionally synthesized from carbonaceaous material. Its pore size distribution, physical strength, and other properties depend on both the raw material and the activation procedure. As discussed, carbon capture via physical adsorption requires small pores in the micropore range. To achieve this and also maintain physical strength to sustain PSA operations, Activated Carbon is made using thermal activation of a dense form of carbon[27]. Since it is nonpolar, thus hydrophobic, and has a small surface polarity, it is suitable for CO_2 capture and does not degrade in the presence of water. In fact, Activated Carbon has a high capacity to adsorb it[19]. This porous material also has a lower heat of adsorption when compared to zeolites, for example, which is a benefit during the regeneration step[28].

Carbon Molecular Sieves (CMSs) are made out of similar raw materials as for Activated Carbon, although, one additional step is added to the production process. This step is hydrocarbon cracking which allows uniform and controllable pore structures[28]. The latter also explains that the production costs for CMS are higher compared to Activated Carbon. The achieved improvements in kinetic effects enhance the selectivity for smaller molecules, although, surface interactions stay similar to that of Activated Carbon[19]. A CMS is mostly used in the separation of high purity nitrogen from air[20].
Silica gel is a dehydrated amorphous solid, with a large surface area to volume ratio[28]. It is polar which helps with adsorbing water and hydrophilic components through hydrogen bonding. Silica gel also has a relatively low heat of adsorption for water[20]. These properties make Silica gel suitable for drying applications, but not for CO_2 adsorption specifically.
Zeolites are porous crystalline aluminosilicates, with a uniform pore size. They are suitable for size based separation methods, given that there is almost no pore distribution[20]. Zeolites being polar are suitable for carbon capture, by utilizing CO_2's strong quadrupole moment. On the other hand, the use of zeolites involves degradation challenges as zeolites dissolve in water (are hydrophilic)[25]. This issue with humid gas streams can be solved by increasing the silica/alumina ratio, for larger hydrophobicity. The drawback for such adjustments, is that the decreased polarity results in a lower affinity towards CO_2. Other solutions would be to remove the water vapor prior to adsorption, or use zeolite in a successive stage before which the gas is passed through a different column with, for instance, activated carbon that adsorbs the water.

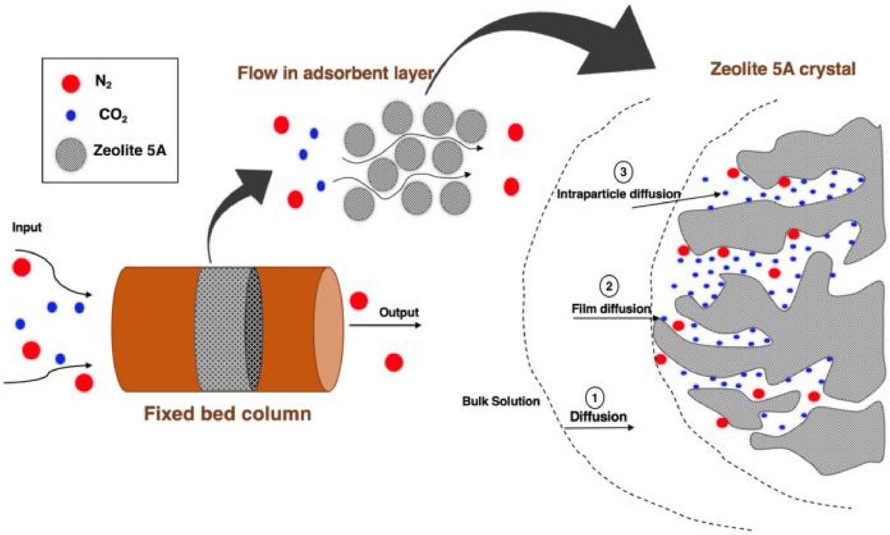

Figure 5: Adsorption process with the involved mechanisms for adsorbent material Zeolite 5A [29]

Metal Organic Frameworks (MOFs) is a new material type, with high surface to volume ratio. The choice of composition and type of metal make MOFs customizable adsorbents with tunable pore size distributions. Their adsorption properties can also be modified by the addition of functional groups to enhance selectivity towards CO_2 (e.g. adding of functional groups with strong permanent dipole moments -NO_2 & -CN to interact with the quadrupole moment of CO_2)[19]. Current development is focused on solving degradation issues when in contact with water and air[20].

Due to the wide range of adsorption capacities reported in available literature, it is not possible to select the best adsorbent material. Therefore, this study will focus on the two materials currently of most interest to HyGear: Activated Carbon (AC) and Zeolite 13X (Ze13X). These are also the most widely researched and have the highest technological readiness[25]. A visualization of the adsorption process and the discussed mechanisms is shown in Figure 5. It may also be noted that other material types are also being researched for carbon capture applications, such as calcium oxide, alkali-metal carbonate, amine-modified materials, and activated alumina[25]. These are excluded because they are either in an earlier stage of development, or require additional process heat.

The isotherm data for the components in the flue gas is obtained from previous experimental studies and is used to analyze the selectivity and adsorption capacity. Both Activated Carbon and Zeolite 13X are shown in Figure 6, where the isotherms are plotted for a range of 0 to 7 bar also showing the temperature dependence. From these plots can be seen that both have a favorable type I isotherm. Note that the isotherm for oxygen is not shown, to limit the number of lines as it is almost identical to the isotherm of nitrogen.

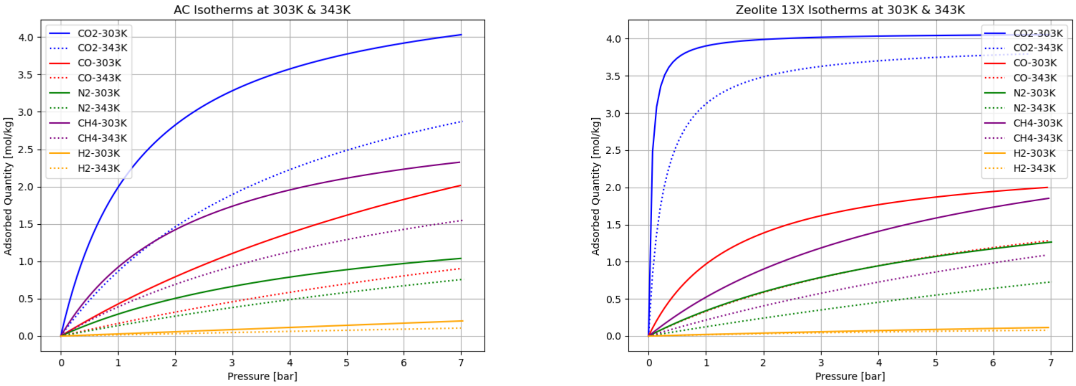

((a)) ((b))

Figure 6: Isotherm adsorption loading on Activated carbon (a) and Zeolite 13X (b) at 303K (lines) and 343K (dotted lines) for CO_2, CO, N_2, CH_4, and H_2[30]

In addition, the steepest isotherm is that of Zeolite 13X which is related to a larger heat of adsorption indicating that the regeneration step is also more energy intensive[25]. Lastly, the isotherms plots are shown individually for three temperatures (303K, 323K, and 343K), in the Appendix in Figures 48, 49, and 50.

2.3 Multicomponent Langmuir Model

The single Langmuir model from Equation 3 can be extended to the dual-site Langmuir model, that describes the adsorption on two distinct adsorption sites with each their own maximum capacity. Using two distinct sites accounts for the inhomogeneities on the adsorbents surface, leading to a variance in binding energies due to different functional groups or pore structures for example[31].

$$q = \frac{q_{b,m} bc}{1 + bc} + \frac{q_{d,m} dc}{1 + dc} \tag{4}$$

For a gas mixture of N species, that compete for the adsorption sites, the loading of species i is then derived as:

$$q_i^* = \frac{q_{b,m,i} \cdot b_i c_i}{1 + \sum_{i=1}^{N} b_i c_i} + \frac{q_{d,m,i} \cdot d_i c_i}{1 + \sum_{i=1}^{N} d_i c_i} \tag{5}$$

Regarding the exothermic nature of adsorption processes, it is important to consider temperature changes because an increasing temperature (in Kelvin) favors desorption. Such temperature effects can be described with the Arrhenius relation:

$$b_i = b_{0,i} \cdot \exp\left(-\frac{\Delta U_{b,i}}{RT}\right) \tag{6}$$

$$d_i = d_{0,i} \cdot \exp\left(-\frac{\Delta U_{d,i}}{RT}\right) \tag{7}$$

The isotherm of water, as discussed before, has a type II or IV isotherm due to capillary condensation into the pores (wether there is a hysteresis effect as type IV depends on the material). As a result multiple layers of water adsorb on the surface forming a meniscus. Consequently, the adsorption capacity for water is higher than what is assumed in monolayer Langmuir models. Hence the model may be altered by adding an extra term as proposed in available literature[32]. In addition, adsorption effects such as monolayer adsorption and capillary condensation are visualized in Appendix Figure 51.

$$q_i^* = \frac{q_{b,m,i} \cdot b_i c_i}{1 + \sum_{i=1}^{N} b_i c_i} + \frac{q_{d,m,i} \cdot d_i c_i}{1 + \sum_{i=1}^{N} d_i c_i} + q_{cc,m} \cdot tan^{-1}\left(\zeta \phi^{\beta \cdot T + \gamma_{cc}}\right) \tag{8}$$

The maximum monolayer adsorption constants of the two sites remain the same, whereas the added arc-tangent term is multiplied with, $q_{cc,m}$, the maximum amount of adsorbed water due to capillary condensation. ϕ is the relative humidity of the feed gas, whereas ζ, β, and γ_{cc} are fitting coefficients. Although this function can account for capillary condensation, it does not account for hysteresis effects that may occur. The adsorption isotherm for water is shown for multiple temperatures in Figure 7.

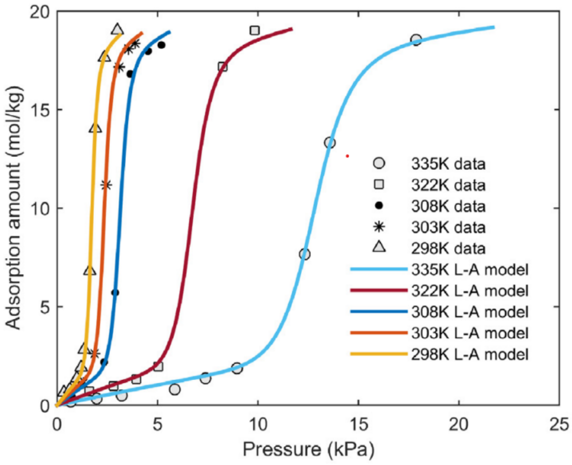

Figure 7: Water isotherm data on Active carbon for different temperatures[32]

Similar functions representing water adsorption on Ze13X are not reported, since most available literature focuses on the degradation effects. Therefore, the water adsorption isotherm parameters for this adsorbent material are given in Appendix Table 11 using the general double Langmuir model. However, as suggested in another study, the double Langmuir adsorption model could be expanded with a competitive adsorption term that lowers the adsorption of all components[33].

2.4 Model Validation

Even though the used basic model has been validated in a previous study, validating it can be done through recreating a dynamic column breakthrough simulation of an adsorption process described in available literature[34]. The result of a recreated analysis, is shown in Figure 8. This case study was done for a 15/85 CO_2/N_2 mixture that was fed with a velocity of 1 m/s into a column with Zeolite 13X. There are two fronts present, due to the exothermic nature of the adsorption process. The first is the the breakthrough of CO_2, during which the temperature rises. Subsequently the adsorption stagnates, until the adsorbent cools down enough at which the second front breaks through reaching saturation. Besides the validation of the model, this also shows that the mass transfer effects are more dominant than the energy transfer because the effect of the gas moving through the column is more significant than that of the changes in temperature during the process.

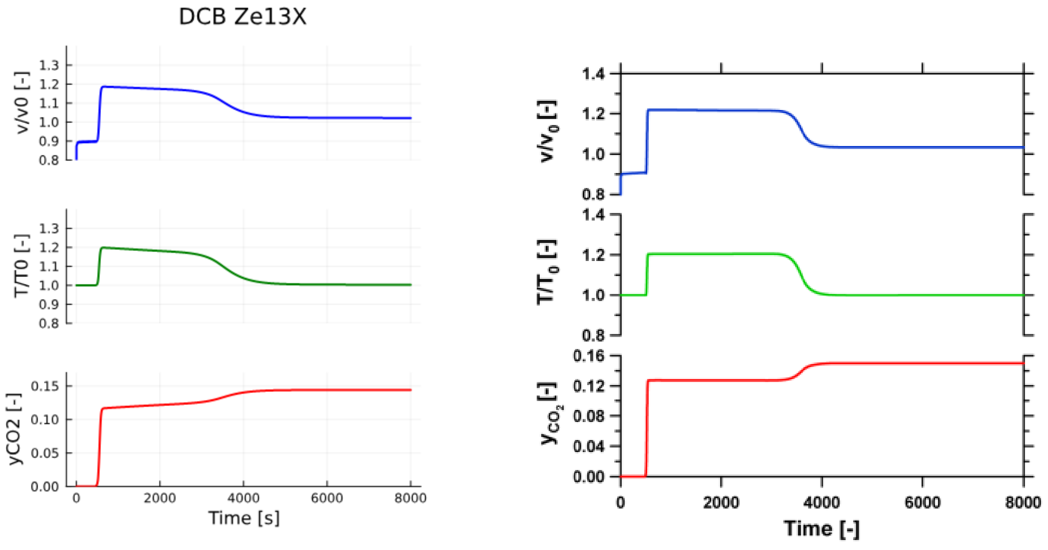

((a)) ((b))

Figure 8: Recreation of a dynamic column breakthrough simulation (a) model result, (b) case study from literature[34]

2.5 Process Description

The basic VSA system is shown in Figure 9, in which the respective changes are also visualized. First the column is pressurized using the feed gas to the desired adsorption pressure, which is either close or equal to atmospheric pressure. During the adsorption phase, the exothermic adsorption takes place. The heat released may require temperature regulation measures. Whilst the adsorption material reaches saturation, the co-current/forward blowdown is initiated during which the pressure is reduced to an intermediate pressure such that the CO_2-lean gas leaves the column at the top whilst the adsorbed CO_2 stays in place. The last step is to reduce the pressure further to the desorption pressure, extracting the CO_2-rich gas at the bottom.

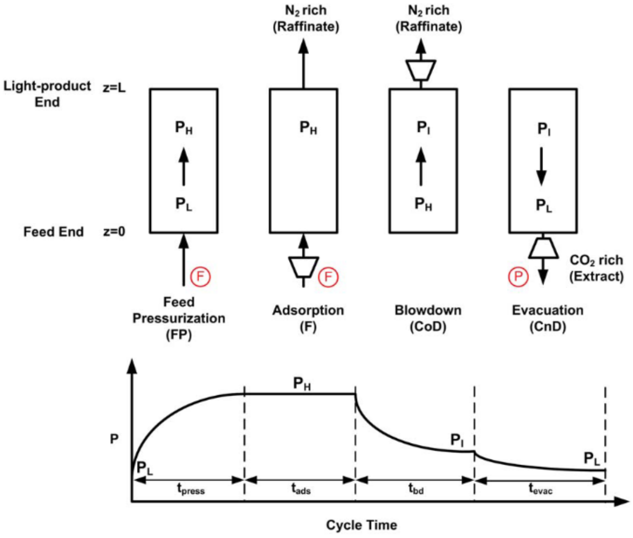

Figure 9: Visualization of basic 4-phase VSA cycle[35]

During adsorption, the concentrations of the adsorbate (CO_2) in fluid and solid phase change with both time and position in the bed. After some time, the beginning of the bed approaches saturation, and the majority of the mass-transfer takes place further from the inlet. The region where the majority of the mass-transfer takes place is called the mass-transfer zone (MTZ)[19]. The change in concentration, and thus the movement of the MTZ, can be analyzed in so-called breakthrough curves. An example of a breakthrough curve is shown in Figure 10, in which c/c_0 the fluid to feed ratio of the adsorbate is plotted against time. These plots also aid in determining the optimal duration of the adsorption phase, after which the flow is stopped and/or directed to a fresh bed.

The width of the MTZ, or steepness of the breakthrough curve, is directly influenced by the shape of the isotherm. Namely, for favorable isotherms (type I) the breakthrough curves become self-sharpening. On the other hand, unfavorable isotherms show widening breakthrough curves when advancing through the bed. Ideal adsorption systems would show a vertical breakthrough curve, indicating that the amount of adsorbed adsorbate is proportional to the adsorption time and the flowrate. Also the costs of the system increase as the MTZ gets wider, because the bed use per cycle decreases for a larger MTZ to bed length ratio (less of the adsorbents surface area is used in the case). As a lower portion of the bed reaches saturation per cycle, more adsorbent material is required for the desired adsorption target. This increases both the length of the required bed and the pressure drop over the bed, resulting in additional costs.

These breakthrough curves also show the effect of optimizing the adsorption time as a system parameter[36]. When the adsorption step stops before a breakthrough of CO_2, then the recovery, for example, is increased as the CO_2 losses are minimized. However, this decreases the purity of the CO_2, after desorption, as the bed is not fully saturated with CO_2 yet. This is one example of the trade-off between purity and recovery. Similarly, a case can be made for prioritizing purity over recovery by only stopping the adsorption step after the adsorbent is fully saturated with CO_2. This maximizes the potential purity that can be captured, with the cost of losing a lot of CO_2, since the entire MTZ is now located at, or beyond, the outlet of the column indicating the amount of CO_2 vented to the environment.

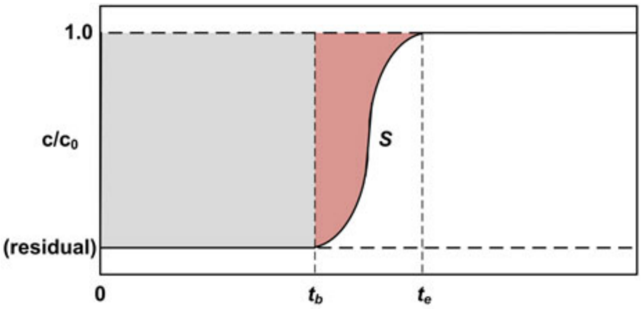

Figure 10: Time trace of an adsorber bed, showing a breakthrough curve, that reaches saturation over time, where breakthrough starts at t_b and saturation/equilibrium is reached at t_e[19]

Similar trade-offs can be seen with regards to the operating pressures of the different phases. Increasing adsorption pressures generally improves CO_2 capture, with the cost of a higher energy penalty, although at too high pressures adsorption may be more favorable for other molecules lowering the purity[37]. The optimization for the blowdown pressure, deals with finding a pressure that is low enough to desorb unwanted gasses from the bed and maximize the CO_2 purity. Choosing a too low pressure may also desorb some CO_2 which lowers the recovery. Moreover, unwanted gaseous species are mostly present at the top of the column at the end of the adsorption step, since bed saturation progresses upwards from the bottom. For the desorption pressure, lowering the pressures increases purity and recovery performances but has the highest energy cost for the work required by the vacuum-pump.

Another version of a VSA cycle makes use of a pressure equalization step, where a column (at the end of its adsorption step) under the highest system pressure, P_{adsorb}, is connected to a column at the lowest system pressure, P_{desorb}. Due to this connection, both vessels are equalized to an intermediate pressure as part of the gas from the top of the high pressure column flows into the low pressure column. This flow is a CO_2-poor gas stream as a result of the adsorption step.

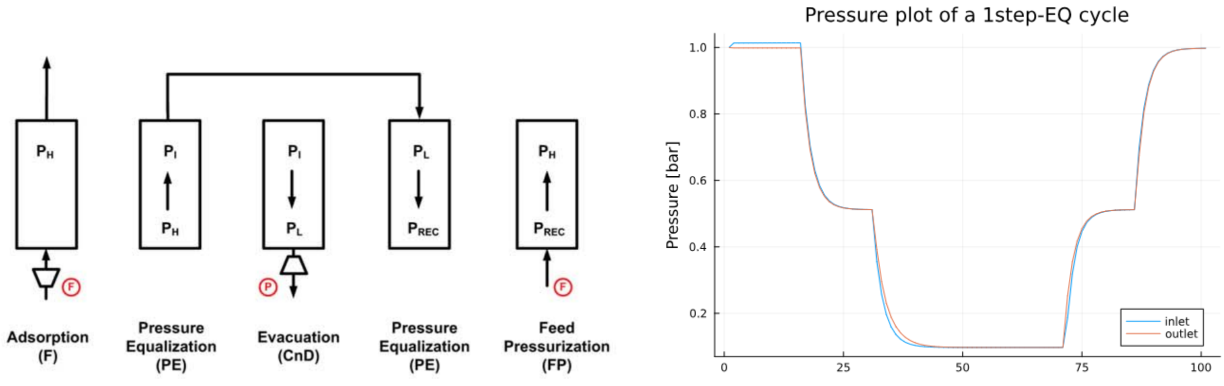

((a)) ((b))

Figure 11: (a): Example of a 5 step adsorption cycle [35] and (b): respective pressure plot

This brings a benefit as unwanted species are removed from the column prior to desorption without an energy penalty. Also, recovery is improved because the gas is passed on through the system instead of released/vented to the environment[35]. An example of such a system is shown in Figure 11. The number of equalization steps increases the benefits that are mentioned above, although the complexity and the costs of the equipment increase with it as well (every additional equalization step requires 2 more columns, which increases the CAPEX and the pressure drop due to the addition of both columns and pipes). In Figure 12 the effect of 3 equalization steps is shown for a CO_2/N_2 mixture[36]. This figure shows how the equalizations do not affect the CO_2 loading in the column, maintaining recovery, and reduce the nitrogen loading improving the purity. Furthermore, along the end/top of the column the nitrogen loading is largest which is due to the adsorption process where CO_2 is adsorbed throughout the bed whereas nitrogen is able to pass through the column to the top.

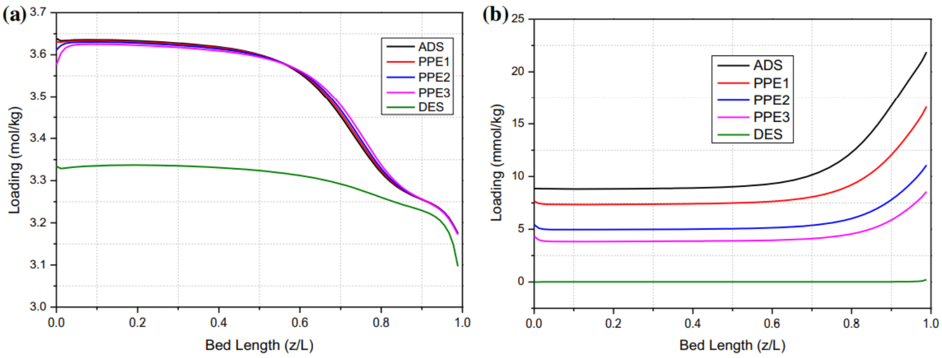

Figure 12: Loading profiles of Ze13X influenced by the 3 equalization steps for a vacuum desorption pressure of 3kPa, where **(a)** shows the CO_2 loading and **(b)** the N_2 loading [36]

Knowing that the flue gas contains water vapor, which is detrimental for the CO_2 adsorption captaincy on Ze13X, another system can be of interest where two columns are placed in series, where the first adsorption column is used to adsorb water, which adsorbs more quickly than CO_2 (making sure minimal CO_2 is adsorbed in the first column). As such, the breakthrough gas of the first column is the dried flue gas that is fed to a successive column to capture the CO_2[38].

In such a scenario, the first column is designed to adsorb all water from the gas using Active Carbon whereas Zeolite 13X, for instance, can be used in the second one (which cannot handle water but does have better carbon adsorption properties than AC). An example of this system is shown in Figure 13, in which second stage is both fed and re-pressurized using the dried gas leaving the first stage during adsorption. The same result could also be achieved by using two adsorbent materials in the adsorber column, a so-called multi-layered column, where a layer of AC is placed at the bottom to prevent water adsorption on the remaining Ze13X. Which option is best highly depends on the composition of the feed. With regards to the costs of the potential system, it is preferred to limit the amount of columns of the final design.

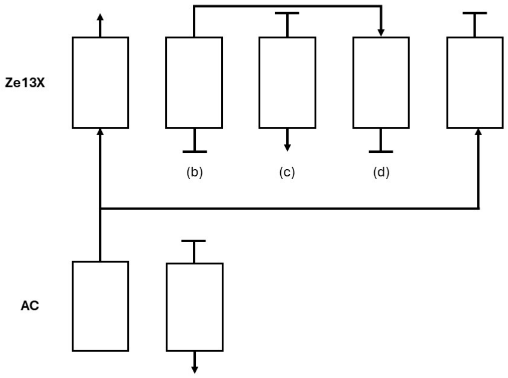

Figure 13: Schematic of two columns placed in series with an Activated Carbon bed and a 13X zeolite for adsorbing CO_2 in wet conditions; adapted from [38]

Additionally, as suggested in available literature, the carbon capture process can be improved by adding a stage to the system, depicted in Figure 14. These stages are designed such that dry flue gas passes through a yield-prioritized stage with Activated Carbon, of which the desorbed product is passed through a purity prioritizing stage with Zeolite 13X where breakthrough gas may be recycled[39],[40]. This last design possibility can be of use, in case a single stage cannot achieve both the recovery and purity demand. In case a drying step is required, it is essential to consider the placement of this step in a two-stage system; either in between or in front of both stages or by using a multi-layered column.

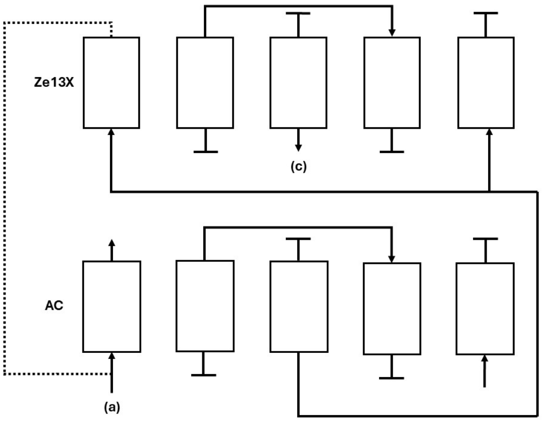

Figure 14: Schematic of a multiple stage adsorption cycle for dry flue gas entering the first stage at (a), The first column prioritizes yield and increases the CO_2 concentration of the desorption product which is fed into the second stage that prioritizes purity where, if necessary, the breakthrough gas stream may be recycled, and the pure CO_2 product is obtained at (c)

Following the discussed design possibilities, this research also looks into the potential of two-stage VSA cycles. In doing so, an additional boundary should be accounted for as the volume of gas obtained during the desorption of the first cycle should equal the volume introduced to the second cycle during both adsorption and re-pressurization. The adsorption cycles discussed in this section form the context for this research, where the four phase cycle with blowdown is the base case and the designed equalization cycles, derived form available literature, are tested as possible improvements[34],[35],[40]. These systems will be analyzed and compared based on their respective yield, purity, energy consumption. As suggested in available literature, a dry feed mixture with a minimum CO_2 concentration of 25% is required to achieve 99% purity using Ze13X[41]. Therefore, it is expected that the optimization process will verify that multi-stage design is required to achieve food-grade purity CO_2 out of HyGear's SMR flue gas.

2.6 HyGear's VSA model

Simulating the full adsorption cycle is done using a dynamic model. A single column is simulated which undergoes each phase of the cycle successively, as shown in Figure 9. Actual reactors may exhibit deviations from ideal plug flow behavior, due to turbulence or flow through bed packing. Hence, an axial dispersion model is used to accurately describe the influence of backmixing due to diffusivity and axial dispersion. These models have a diffusion-related term in the z-direction. The model allows variation of several input variables, for example the isotherm data for different materials and operating pressure can be adjusted. The total list of these parameters can be found in Appendix Table C. Using these input variables, a set of ordinary differential equations is derived from the governing momentum-, mass-, and energy balances. The obtained PDE problem is solved using a Kvaerno5 or RadauIIA5, implicit Runge-Kutta, solver designed for stiff & cyclic computational problems, suited for the sharp concentration fronts observed in adsorption processes[42].

For the conservation of momentum, Darcy's law is used instead of Navier-Stoke's equations because those equations require geometrical data of every instance of the medium which is impractical. Darcy's law, on the other hand, allows one to describe momentum in more practical terms such as porosity and particle sizes. As such, the conservation of momentum is derived from the pressure drop over the column. This is described in terms of superficial velocity, where the change in dimensionless pressure, $\bar{P}$, is taken in the axial direction and viscosity is assumed to be constant (note that this ¯ indicates a dimensionless variable for the other equations as well):

$$v = \frac{D_p^2}{150\mu L}\left(\frac{\epsilon}{1-\epsilon}\right)^2\left(-\frac{\partial \bar{P}}{\partial z}\right) \tag{9}$$

Conservation of mass is describes the changes in concentration over time. This is done using the plug flow assumption with an additional axial dispersion model, that accounts for mixing that normally results from turbulence or flow through the packing of the bed. Furthermore, the mass balance also has additional terms to account for adsorption/desorption effects where mass is exchanged between the two phases. As such the conservation of mass can be written for each species i by applying the ideal gas law with $c_i = \frac{y_i P}{RT}$:

$$\frac{\partial y_i}{\partial t} = \underbrace{\frac{1}{Pe}\frac{\bar{T}}{\bar{P}}\frac{\partial}{\partial z}\left(\frac{\bar{P}}{\bar{T}}\frac{\partial y_i}{\partial z}\right)}_{\text{Diffusion / Axial Dispersion}} - \underbrace{\frac{\bar{T}}{\bar{P}}\frac{\partial}{\partial z}\left(\frac{y_i \bar{P}\bar{v}}{\bar{T}}\right)}_{\text{Convective Mass Transport}} - \underbrace{\frac{R\bar{T}q_{s,0}}{\bar{P}}\frac{1-\epsilon}{\epsilon}\frac{\bar{T}}{\bar{P}}\frac{\partial x_i}{\partial t}}_{\text{Ads-/Desorption effects}} - \underbrace{\frac{y_i}{\bar{P}}\frac{\partial \bar{P}}{\partial t}}_{\text{Pressure Changes}} + \underbrace{\frac{y_i}{\bar{T}}\frac{\partial \bar{T}}{\partial t}}_{\text{Temperature Changes}} \tag{10}$$

In addition, the rate of adsorption is described as a linear driving force, using the loading q_i^* calculated with the competitive Langmuir adsorption model from Equation 5. The rate of adsorption is written using the dimensionless mass transfer coefficient α_i, which is written to show the involved terms:

$$\frac{\partial x_i}{\partial t} = \underbrace{\frac{L}{v_0}\frac{c_i}{q_i^*}\frac{15\epsilon_p\frac{D_{m,i}}{\tau'}}{r_p^2}}_{\text{mass transfer coefficient}}\left(x_i^* - x_i\right) \tag{11}$$

The conservation of mass for the bulk flow is described in terms of the change in pressure over time, which is derived from summing all species i present in the gas stream ($\sum y_i = 1$):

$$\frac{\partial \bar{P}}{\partial t} = -\bar{T}\frac{\partial}{\partial z}\left(\frac{\bar{P}}{\bar{T}}\bar{v}\right) - \frac{R\bar{T}q_{s,0}}{\bar{P}}\frac{1-\epsilon}{\epsilon}\bar{T}\sum_{i=1}^{n_{comp}}\frac{\partial x_i}{\partial t} + \frac{\bar{P}}{\bar{T}}\frac{\partial \bar{T}}{\partial t} \tag{12}$$

As for the conservation of energy, the energy balance is based on the heat balance for the column and a heat balance for the wall. Both equations have a number of dimensionless grouped terms (Ω, σ_i, and Π) that are given in Appendix A. Besides shortening the equation, forming dimensionless groups helps with identifying the terms (conduction, heat of adsorption etc.). It may also be noted that, in general, the non-dimensionalization is performed to improve the stability of the model. The column heat balance is found to be:

$$\begin{aligned}\frac{\partial \bar{T}}{\partial t} = {} & \underbrace{\Omega_1\frac{\partial^2 \bar{T}}{\partial t^2}}_{\text{Heat Diffusion}} - \underbrace{\Omega_2\frac{\partial}{\partial z}(\bar{v}\bar{P})}_{\text{Convective Heat Transport}} - \underbrace{\Omega_3\bar{T}\sum_{i=1}^{n_{comp}}\frac{\partial x_i}{\partial t}}_{\text{Ads-/Desorption Effects}} \\ & + \underbrace{\sum_{i=1}^{n_{comp}}\left(\sigma_i\frac{\partial x_i}{\partial t}\right)}_{\text{Heat of Ads-/Desorption}} - \underbrace{\Omega_4(\bar{T}-\bar{T}_w)}_{\text{Heat Transfer with Column Wall}} - \underbrace{\Omega_2\frac{\partial \bar{P}}{\partial t}}_{\text{Pressure Changes}}\end{aligned} \tag{13}$$

And the wall heat balance is written as:

$$\frac{\partial \bar{T}_w}{\partial t} = \underbrace{\Pi_1\frac{\partial^2 \bar{T}_w}{\partial z^2}}_{\text{Conduction Through Wall}} + \underbrace{\Pi_2(\bar{T}-\bar{T}_w)}_{\text{Heat Transfer Between Bed \& Wall}} - \underbrace{\Pi_3(\bar{T}_w-\bar{T}_{amb})}_{\text{Heat Transfer Between Wall \& Environment}} \tag{14}$$

These six equations describe the conservation laws for the adsorption column, that can be solved using spatial discretization techniques. The finite volume method is used in this case, in combination with a set of boundary conditions, because it can handle sharp fronts which help to describe fluxes in mass, energy, and momentum. As such the column is divided into N cells with width Δz and volume ΔV, as shown in Figure 15.

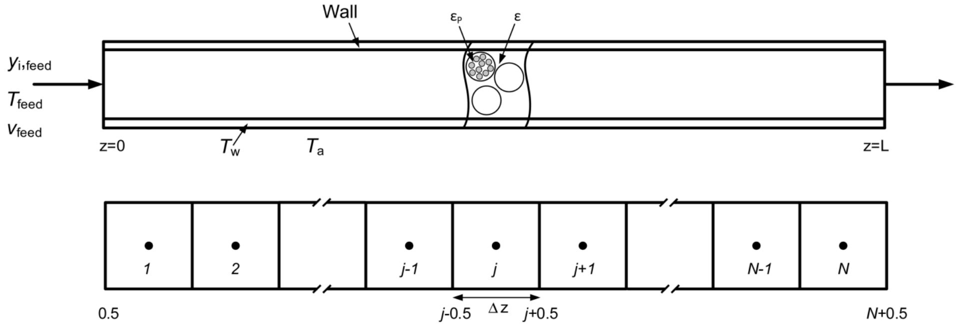

Figure 15: Schematic of the adsorption column with finite volume, divided into N cells with a staggered grid [35]

By using a staggered grid, the in and outlet vector quantities are conveniently stored at the boundaries. Similarly, the scalar cell quantities are stored in the cell's center. Computing integrations over the cells with boundaries j-0.5 and j+0.5, requires interpolation of the centered scalar quantities which is done using the weighted essentially non-oscillatory (WENO) scheme. As the name suggest, this scheme removes non-physical oscillations around the fronts. The WENO scheme is further discussed in the Appendix A.
Regarding the finite volume method as discussed above, it becomes clear that the accuracy of the simulations increases with the number of cells. This comes with the cost of the required computational time and power to do so. Similarly, as the model solves the PDE problem discussed above several cycles are required in order to reach a stable solution of the process. As mentioned in literature, the required number of cycles to reach this cyclic steady state (CSS) may vary from 40 to 400 cycles[34]. Subsequently, the required time to compute just a single solution for a parameter study can take up several hours. Therefore, time is a serious constraint for this type of research. To solve this matter, the results of a large and small accuracy simulation have been studied which is discussed in detail in Appendix Section A.3. These results validated the reduction of cells and cycles per simulation, because the drop in accuracy was insignificant. Hence, the majority of the simulations of this study has been done using 8 cells and extracting a solution after 6 cycles. However, simulations of 32 cells and 50 cycles were utilized for cases during which the Cyclic Steady State (CSS) were to be derived.

2.6.1 Performance Analysis

The results of each simulation are compared based on the achieved purity, recovery, productivity and energy consumption. Of which three are essential parameter performance indicators specified in the research question. The remaining productivity is also an important term, because it is a measure of the adsorption efficiency. The bed productivity of a process provides information on how much of the adsorption capacity is effectively utilized to capture CO_2. These performance indicators are defined as follows:

$$\text{Purity} = \left(\frac{\text{mol}_{\text{out, CO}_2|\text{evac}}}{\text{mol}_{\text{out}|\text{evac}}}\right) \cdot 100\% \tag{15}$$

$$\text{Yield} = \left(\frac{\text{mol}_{\text{out, CO}_2|\text{evac}}}{\text{mol}_{\text{in, CO}_2|\text{ads}} + \text{mol}_{\text{in, CO}_2|\text{press}}}\right) \cdot 100\% \tag{16}$$

$$\text{Productivity} = \frac{\text{mol}_{\text{out, CO}_2|\text{evac}}}{\text{Adsorbent Volume} \cdot \text{Cycle Time}} \tag{17}$$

$$\tag{18}$$

Furthermore, the amount of moles going in, or out, of the system can be derived by integrating over the column's inlet/outlet:

$$\text{mol}_{\text{in, CO}_2} = \frac{P_0 v_0}{RT_0}\epsilon A \int_0^{\text{t}_\text{step}} \left(\bar{v}_{0.5}(t)\frac{y_{0.5}\bar{P}_{0.5}(t)}{\bar{T}_{0.5}(t)}\right) dt \tag{19}$$

$$\text{mol}_{\text{out, CO}_2} = \frac{P_0 v_0}{RT_0}\epsilon A \int_0^{\text{t}_\text{step}} \left(\bar{v}_{N+0.5}(t)\frac{y_{N+0.5}\bar{P}_{N+0.5}(t)}{\bar{T}_{N+0.5}(t)}\right) dt \tag{20}$$

$$\tag{21}$$

Lastly, the cycle's energy consumption is determined through calculating the energy requirement for each phase of the cycle. The pressurization requires compressing energy if the feed pressure is lower than the (highest) adsorption operating pressure. This holds for the adsorption phase as well, although how much energy is required mainly depends on the adsorption duration in this case. However, some energy is also required to overcome frictional pressure losses (maintaining operating pressure). The energy requirement during the blowdown and evacuation phase is calculated based on the pressure difference between the operating pressures, and that of the surroundings (estimated at 1 bar). Following the latter, the energy requirements of the four phases are calculated as follows:

$$E_{\text{ads}} = \frac{1}{\eta}\epsilon A \frac{\gamma}{\gamma - 1} \int_{t=0}^{t=\text{ads}} (vP) \mid_{z=0} \left(\left(\frac{P \mid_{z=0}}{P_{\text{feed}}} \right)^{\frac{\gamma-1}{\gamma}} - 1 \right) dt \tag{22}$$

$$E_{\text{bd}} = \begin{cases} \frac{1}{\eta}\epsilon A \frac{\gamma}{\gamma-1} \int_{t=0}^{t=bd} (vP) \Big|_{z=L} \left(\left(\frac{P_{\text{atm}}}{P|_{z=L}} \right)^{\frac{\gamma-1}{\gamma}} - 1 \right) dt & \text{if} P|_{z=L} < P_{\text{atm}} \\ 0 & \text{if} P|_{z=L} \geq P_{\text{atm}} \end{cases} \tag{23}$$

$$E_{\text{evac}} = \frac{1}{\eta}\epsilon A \frac{\gamma}{\gamma - 1} \int_{t=0}^{t=\text{evac}} (vP) \mid_{z=0} \left(\left(\frac{P_{\text{atm}}}{P \mid_{z=0}} \right)^{\frac{\gamma-1}{\gamma}} - 1 \right) dt \tag{24}$$

$$E_{\text{press}} = \begin{cases} \frac{1}{\eta}\epsilon A \frac{\gamma}{\gamma-1} \int_{t=0}^{t=press} (vP) \Big|_{z=0} \left(\left(\frac{P|_{z=L}}{P_{\text{feed}}} \right)^{\frac{\gamma-1}{\gamma}} - 1 \right) dt & \text{if} P|_{z=0} > P_{\text{feed}} \\ 0 & \text{if} P|_{z=0} \leq P_{\text{feed}} \end{cases} \tag{25}$$

These terms can be summed and divided by the mass of CO_2 obtained from the evacuation phase to derive the power requirement per kilogram of CO_2 as stated in Equation 26. Note that variables η and γ are terms for the compression efficiency and adiabatic constant respectively, which are derived from [35] ($\eta = 0.72$ and $\gamma = 1.4$).

$$E_{\text{Total}} = \frac{E_{\text{Ads}} + E_{\text{bd}} + E_{\text{evac}} + E_{\text{press}}}{\text{Mass}_{\text{out, CO}_2|\text{evac}}} \tag{26}$$

Before moving on to the model development, it must be addressed that the the blowdown energy term in the total energy calculation drops out for VSA cycle designs that use pressure equalization because the equalization occurs spontaneously as soon as the columns are connected (or as soon as the valves of the tubes connecting these columns are opened).

2.6.2 Model Development

Currently the dynamic model simulates an adsorption 4 phase forward blowdown cycle as described in Figure 9. The discussed differential equations and numerical techniques can be used to simulate this cycle through a set of boundary conditions. Each phase requires 4 boundary conditions to describe the physical constraints in terms of the dimensionless pressure, gaseous concentration of each species, dimensionless temperature, and dimensionless wall-temperature of the column. These boundary conditions can be clarified using Figure 16, which shows the flow direction and inlet/outlet-boundaries of the column for each phase.

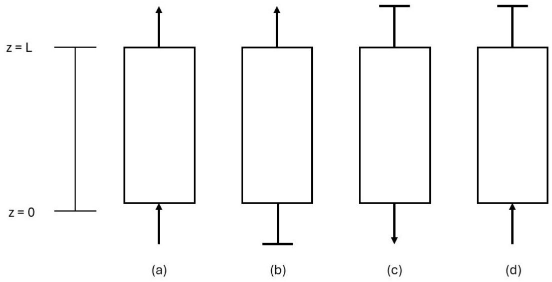

Figure 16: Visualization of the boundary conditions for the 4 phase adsorption cycle; (a) adsorption, (b) forward blowdown, (c) desorption, (d) re-pressurization

The boundary conditions for the 4 phase adsorption cycle are presented in Table 16, and to explain how the conditions are derived the conditions during adsorption are explained in more detail below.

Table 4: Boundary conditions for the 4 phase adsorption cycle

Phase	**z = 0**	**z = L**
Adsorption (open-open)	$\bar{P}\mid_{z=0}=\bar{P}_1+\frac{\bar{v}_{0.5}\frac{\Delta z}{2}}{\left[\frac{4}{150}\left(\frac{\epsilon}{1-\epsilon}\right)^2\right]r_p^2\frac{P_0}{\mu v_0 L}}$ $y_i\mid_{z=0}=y_{i,feed}$ $\bar{T}\mid_{z=0}=\bar{T}_{feed}$ $\bar{T}_w\mid_{z=0}=\bar{T}_{amb}$	$\bar{P}\mid_{z=L}=1.0$ $\frac{\partial y_i}{\partial z}\mid_{z=L}=0$ $\frac{\partial \bar{T}}{\partial z}\mid_{z=L}=0$ $\bar{T}_w\mid_{z=L}=\bar{T}_{amb}$
Blowdown (closed-open)	$\frac{\partial \bar{P}}{\partial z}\mid_{z=0}=0$ $\frac{\partial y_i}{\partial z}\mid_{z=0}=0$ $\frac{\partial \bar{T}}{\partial z}\mid_{z=0}=0$ $\bar{T}_w\mid_{z=0}=\bar{T}_{amb}$	$\bar{P}\mid_{z=L}=\frac{\left(P_I+(P_H-P_I)e^{-\lambda\tau\frac{L}{v_0}}\right)}{P_0}$ $\frac{\partial y_i}{\partial z}\mid_{z=L}=0$ $\frac{\partial \bar{T}}{\partial z}\mid_{z=L}=0$ $\bar{T}_w\mid_{z=L}=\bar{T}_{amb}$
Desorption (open-closed)	$\bar{P}\mid_{z=0}=\frac{\left(P_L+(P_I-P_L)e^{-\lambda\tau\frac{L}{v_0}}\right)}{P_0}$ $\frac{\partial y_i}{\partial z}\mid_{z=0}=0$ $\frac{\partial \bar{T}}{\partial z}\mid_{z=0}=0$ $\bar{T}_w\mid_{z=0}=\bar{T}_{amb}$	$\frac{\partial \bar{P}}{\partial z}\mid_{z=L}=0$ $\frac{\partial y_i}{\partial z}\mid_{z=L}=0$ $\frac{\partial \bar{T}}{\partial z}\mid_{z=L}=0$ $\bar{T}_w\mid_{z=L}=\bar{T}_{amb}$
Pressurization (open-closed)	$\bar{P}\mid_{z=0}=\frac{\left(P_H+(P_H-P_L)e^{-\lambda\tau\frac{L}{v_0}}\right)}{P_0}$ $\frac{\partial y_i}{\partial z}\mid_{z=0}=y_{i,feed}$ $\frac{\partial \bar{T}}{\partial z}\mid_{z=0}=\bar{T}_{feed}$ $\bar{T}_w\mid_{z=0}=\bar{T}_{amb}$	$\frac{\partial \bar{P}}{\partial z}\mid_{z=L}=0$ $\frac{\partial y_i}{\partial z}\mid_{z=L}=0$ $\frac{\partial \bar{T}}{\partial z}\mid_{z=L}=0$ $\bar{T}_w\mid_{z=L}=\bar{T}_{amb}$

Firstly for the adsorption case, both ends of the column are open. For the dimensionless pressure at the inlet, this means that it is equal to the dimensionless pressure at the center of the first cell plus the pressure drop over the first half of that cell (given that the inlet velocity is known). The dimensionless pressure at the top of the column is equal to the adsorption pressure to ensure stable operation. For the gaseous concentration of each species, this is equal to the feed concentration at the inlet as there is a constant feed of new gas during this phase. On the other hand, the concentration gradient at the outlet is set to zero, assuming steady state behavior, as there are no concentration changes beyond the column's outlet. Lastly, the wall temperature is assumed to be equal to the ambient temperature.

2.6.3 Developing an Equalization Cycle

For this study HyGear's dynamic model of a 4 phase blowdown system is expanded to a 5 phase equalization system as shown in Figure 11. This entails that the pressure equalization step needs to be modeled and implemented replacing the blowdown step. When connecting the high pressure and low pressure column, their dynamics, gas composition and temperature influence the equalization pressure, besides P_{adsorb} and P_{desorb}, that is reached when approaching equilibrium. Consequently, the intermediate pressure is no longer a design parameter as with the blowdown system but a fixed parameter that must be calculated. Determining the equalization pressure for each cycle is a laborious process as the high pressure column needs to be equalized with a low pressure column which exists in a future time stamp of the simulation, so in order to derive this pressure efficiently a pressure between P_{adsorb} and P_{desorb} can be guessed and adjusted through iteration. The initial guess for this equalization/intermediate pressure is often taken as the average pressure and corrected by a factor x [43],[35].

$$P_I=(1-x)\cdot\frac{P_{\text{adsorb}}-P_{\text{desorb}}}{2} \tag{27}$$

Note that finding the equalization pressures for multiple equalization steps, becomes an algebraic problem but can be solved using the same principle. This is explained in further detail for a 2-step, and, 3-step equalization in Appendix Section A.2.

After the first equalization attempt, mass balance checks can be done to converge to the right equalization pressure[37]. This is described in Equation 28, in which δ^{eq} is the maximum allowed absolute mass balance error, for example 10^{-3}. This tolerance can be changed respective to prioritizing the simulation speed or or the simulation accuracy. In fact, the exchanged mass is small compared to the total of the system, therefore simulation speed is prioritized.

$$\mid \epsilon^{eq} \mid = \mid \frac{m_{in}^{eq} - m_{out}^{eq}}{m_{out}^{eq}} \mid < \delta^{eq} \tag{28}$$

Following this relation, the model can be adjusted accordingly as described in the logical flowchart from Figure 17. This flowchart shows that the implementation of the equalizations requires a logical loop around multiple phases of the model. Through each iteration the equalization pressure is adjusted with the relative mass balance error, that is also multiplied with a sensitivity factor f set between 0 and 1. Moreover, it is worth mentioning that ϵ^{eq} is negative whenever the equalization pressure is too low and vise versa. As a result, the mass balance error, when ϵ^{eq} is negative, is used to increase the equalization pressure.

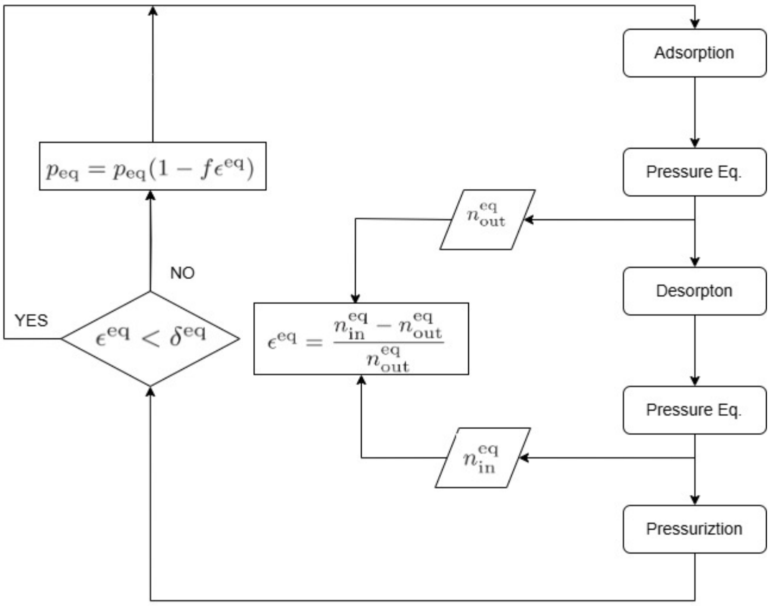

Figure 17: Flowchart of the logical algorithm for the adjustment of the equalization pressure during an adsorption cycle, the pressure is adjusted using the mass balance error and a factor f which can be set between 0 and 1 (adapted from [37])

Lastly, the mass going in and out of the column during the equalization phase can be obtained by integrating over the top-end of the column:

$$\mathrm{m}_{\text{out}}^{eq} = \int_{\text{t = ads}}^{\text{t = eq down}} \rho_{|_{z=L}} v_{|_{z=L}} \epsilon A \quad dt \tag{29}$$

$$\mathrm{m}_{\text{in}}^{eq} = \int_{\text{t = evac}}^{\text{t = eq up}} \rho_{|_{z=L}} v_{|_{z=L}} \epsilon A \quad dt \tag{30}$$

Researching VSA cycles with pressure equalization steps can be facilitated by writing the converged equalization pressure as a function of the desorption pressure (and the adsorption pressure, which is kept constant in this case). In doing so, the iterative equalization pressure convergence procedure has to be done only once over a number of desorption pressures such that the derived function is valid for the desorption range of interest. Over a desorption pressure range of 0.005 to 0.4 bars it was found that the equalization pressure is best described as an adjusted geometric mean of the high and low pressure of the equalizing columns; which is also suggested in another study[44].

$$P_{\text{eq}} = \sqrt[1+C]{\mathrm{P}_H \cdot \mathrm{P}_L} = (\mathrm{P}_H \cdot \mathrm{P}_L)^{\frac{1}{1+C}} \tag{31}$$

As a consequence, the equalization pressure decreases much further than the average value. This is due to the fact that, for lower desorption pressures the column is emptier in both loading and gas concentration such that the gas which is initially transported to the low pressure column is adsorbed, therefore, additional mass transfer is required to effectively increase the pressure. Moreover, this behavior is different for both adsorbent materials due to their difference in isotherms, ease of regeneration, and other adsorption properties. Hence the parameter C differs as well, namely 1.4 for AC and 0.42 for Ze13X. Consequently, the equalization pressures for Ze13X are slightly lower compared to those for AC which can be verified given that the isotherms for N_2 (although also CO_2) are higher for Ze13X.

For the equalization cycle, also a new set of boundary conditions is required. Although they are similar to the other boundary conditions, the most important aspect is to ensure that the gas leaving the top of the high pressure column enters the low pressure column at the top. Thus, the set of boundary conditions should describe a closed-connected situation in which the equalization column giving flow and the equalization column receiving flow both have their own conditions to describe the process. These new boundary conditions are visualized in Figure 18.

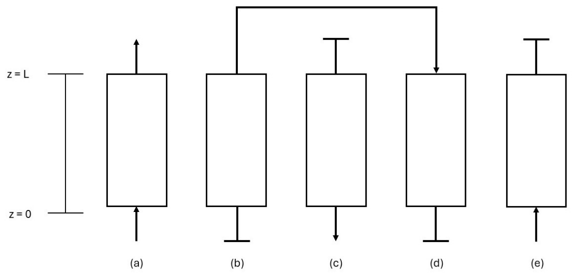

Figure 18: Visualization of the boundary conditions for the 1 Equalization step adsorption cycle; (a) adsorption, (b) decreasing equalization, (c) desorption, (d) increasing equalization, (e) repressurization

The conditions for the closed end at z=0 can be used from the blowdown phase in Table 4, whereas the connected conditions are derived from available literature [43]. This study analyzed the performance of three possible sets, out of which the equalization of variables was found to be the most effective. These boundary conditions, describe the total molar flux, pressure, molar fraction, and temperature at the connections and are given in Table 5.

Table 5: Boundary conditions for equalization cycle

Phase	**z = 0**	**z = L**
Equalization giving flow (closed-connected)	$\frac{\partial \bar{P}}{\partial z} \mid_{z=0} = 0$ $\frac{\partial y_i}{\partial z} \mid_{z=0} = 0$ $\frac{\partial \bar{T}}{\partial z} \mid_{z=0} = 0$ $\bar{T}_w \mid_{z=0} = \bar{T}_{amb}$	$\bar{P} \mid_{z=L} = \frac{\left(P_I + (P_H - P_I) e^{-\lambda \tau \frac{L}{v_0}}\right)}{P_0}$ $\frac{\partial y_i, bedI}{\partial z} \mid_{z=L} = 0$ $\frac{\partial T, bedI}{\partial z} \mid_{z=L} = 0$ $\bar{T}_w \mid_{z=L} = \bar{T}_{amb}$
Equalization receiving flow (closed-connected)	$\frac{\partial \bar{P}}{\partial z} \mid_{z=0} = 0$ $\frac{\partial y_i}{\partial z} \mid_{z=0} = 0$ $\frac{\partial \bar{T}}{\partial z} \mid_{z=0} = 0$ $\bar{T}_w \mid_{z=0} = \bar{T}_{amb}$	$P_{bedII} - P_{bedI} = 0$ $y_{i,bedII} - y_{i,bedI} = 0$ $T_{bedII} - T_{bedI} = 0$ $\bar{T}_w \mid_{z=L} = \bar{T}_{amb}$

2.6.4 Validation

The results of the parameter study that has been done using the developed model, are discussed in Section 3, of which the similarity with available literature is a validation on its own. However, validating the model should also be done beforehand through studying the process of the induced mass-, and energy transfer due to equalization. The latter has been researched in another study as well, although applying the equalization at the bottom of the columns[45].

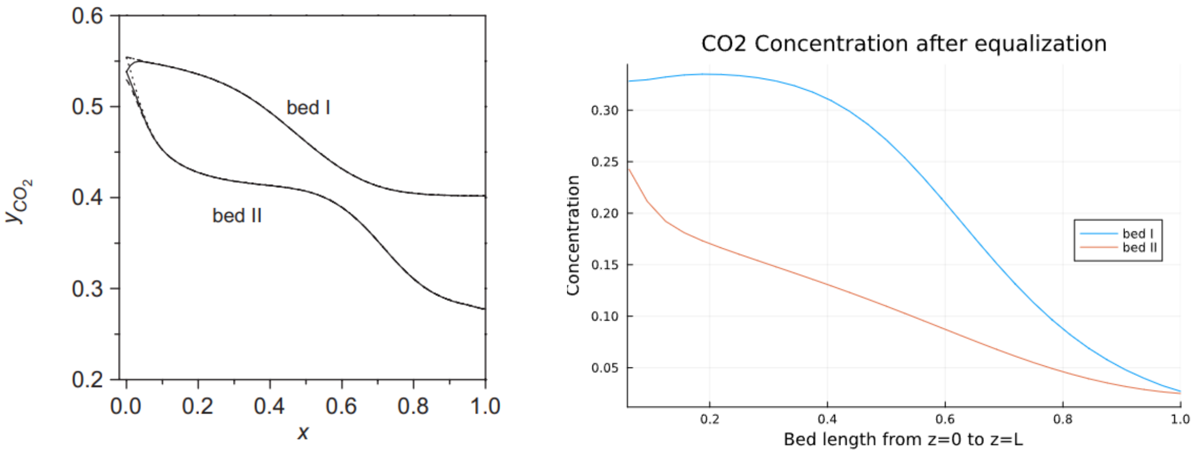

((a)) ((b))

Figure 19: Simulations results of available literature showing (a) the CO_2 gas concentration over the columns at the end of the equalization phase, (b) the concentration proflie obtained using the developed model (where bed I is depressurizing and bed II is pressurizing with the flow provided by bed I)[45]

What the equalization process should showcase is that the concentration profiles, pressure, and temperature at the equalization entries are equal at the end of the phase. Moreover, the partial pressure profile must also show that the gradient does not reside against the flow of the equalization process. A comparison with the findings of the used literature is shown in Figure 19. In addition, the partial pressure of the light, mostly transported, product N_2 has been plotted as well as the temperature change over time in Figure 20. This case study, and comparison to available literature serve as a verification that the construed model describes the equalization process correctly.

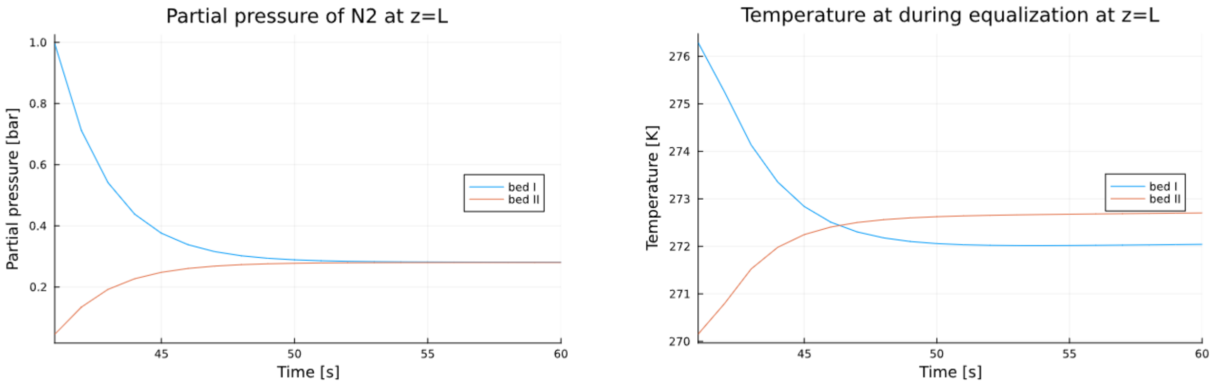

((a)) ((b))

Figure 20: Simulations results the developed model showing (a) the partial pressure of N_2, (b) the temperature both at z=L during the equalization phase (where bed I is depressurizing and bed II is pressurizing with the flow provided by bed I)

2.6.5 Developing a multi-stage model

In order to model an adsorption process with multiple stages as shown in Figures 13 and 14, the gas obtained during desorption/evacuation needs to be saved and inserted during the adsorption and re-pressurization of the next/successive stage. Additionally, the same can be said for cases where a recycle stream is used as suggested in Figure 14. Ensuring continuous flow and having a sound mass balance brings another challenge that will further increase the computation time and complexity of the model. In literature and in practice, this issue is solved by using a reservoir/buffer of the first stage desorber product[39]. Since parametric optimization is the main scope of this study, significant computational power can be saved by optimizing two models separately and change the input conditions of the second stage with the results of the first.

3 Methodology for VSA Parameter study

In order to get a better understanding of the functionality and key-parameters involved in carbon capture via adsorption, it is important to systematically test the different phases of the VSA cycle. As discussed in previous sections, there is a vast number of parameters that influences the performance of this separation process. However, to limit the number of reached variables, and also the number of simulations that is required to do so, this study focuses on the most influential variables; feed composition, duration of given steps, and operating pressures. It may be noted that the model does allow dimensional changes of the column as well, but that these are kept constant throughout this study (namely due to the fact that time or flow speed changes have a similar effect compared to changes in column length[46]). The inner radius, length, and volume of the column for these simulations are 0.1445 m, 1 m, and 0.066 m^3 respectively. These and other parameters are noted in Appendix Table 9.

As the required computational power increases with the number of components in the gas stream, the flue gas mixture is simplified to a dry CO_2/N_2 mixture derived from an available optimization study [35]. N_2 being largely present in the mixture in most occasions, the study of this base case is expected to form a reasonable baseline for real-life scenarios. Knowing that the real flue gas contains water vapors, also humid-operation conditions and drying steps will be analyzed in Section 3.4. Following the derived base case, the separation process will be analyzed for 8 key parameters: The duration of the phases (pressurization, adsorption & evacuation, equalization), the desorption pressure, equalization depth, the inlet feed velocity, and the gas compositions of the feed.

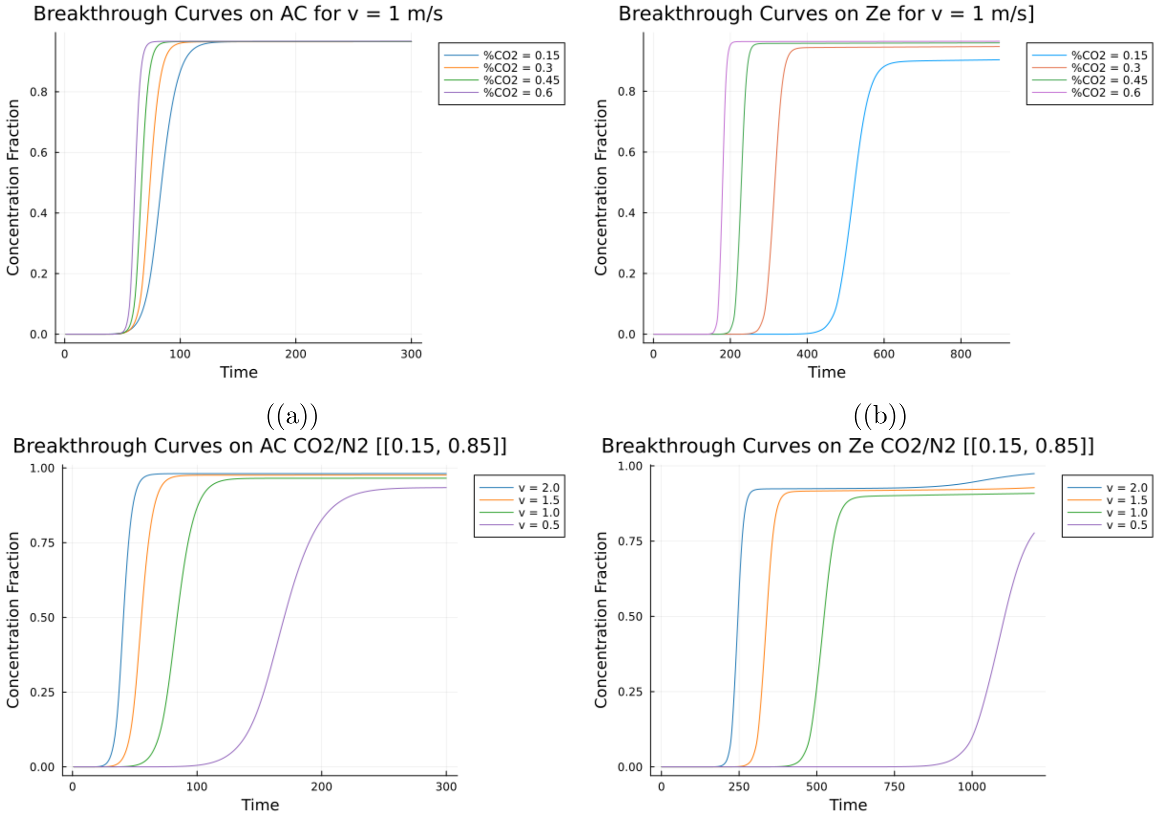

((a)) ((b))

((c)) ((d))

Figure 21: Visualization of the effects of CO_2 concentration and feed velocity on the resulting breakthrough curves on Active Carbon (left side) and Zeolite 13X (right) side, where figures (a) and (b) show the effect of concentration changes, and (c) and (d) the effect of feed velocity

3.1 Adsorption conditions

Starting of, the adsorption process is simulated individually to find find the appropriate operating time which is determined for a set break-through scenario. This scenario describes the point at which adsorption takes place with the least amount of CO_2 lost to the environment. Therefore, the break through curve at the column's end, at z=L, is analyzed for base case conditions of the CO_2/N_2 mixture. These breakthrough curves are shown in Figure 52, from which can be seen that setting the feed velocity (m/s) has an effect on the steepness of the breakthrough curve (width of the mass transfer area).

These simulations also show that the concentration of CO_2 affects how quickly the first concentration front breaks through on Ze13X, whereas on AC this effect is significantly smaller[47]. The feed velocity influences the steepens of both breakthrough fronts. The individual results for each composition and the tested feed velocities can be found in Appendix B Figure 52. All in all, both parameters are important to take into a count for picking a suitable adsorption time. For example, for feed with 15% CO_2 and a feed velocity of 1 m/s the breakthrough times for 4% breakthrough is 62 seconds using Active Carbon and 457 seconds for Zeolite 13X.

Simulating the adsorption process also provides information about the saturation conditions of the adsorbent bed. At this adsorption time the entire surface of the adsorbent, in the column, is saturated. Such a saturation case study, as oppose to the breakthrough scenario, prioritizes purity over yield. Since this state is reached after the breakthrough point the MTZ has fully broken through, and now resembles the amount of gas/CO_2 that is lost to the environment during the process (decreasing the yield). The results of the saturation simulations are shown in in Figure 22. In addition, a more detailed loading comparison is found in Appendix B Figure 25.

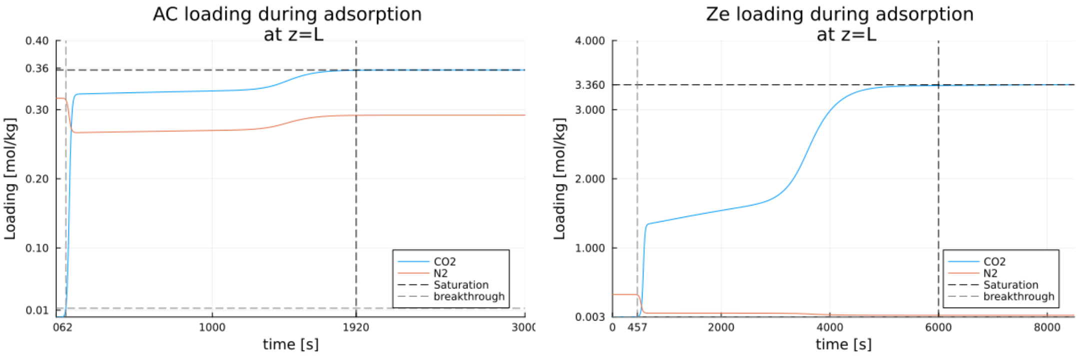

((a)) ((b))

Figure 22: Adsorbent saturation points for (a) Active Carbon, and (b) Zeolite 13X, for a feed velocity of 1 m/s and 15% CO_2, showing the difference in CO_2 loading at z=L at 4% breakthrough and saturation

The saturation point for both adsorbent materials for a feed concentration of 15% CO_2, 85% N_2 and a feed velocity of 1 m/s, is 32 minutes on AC and 100 minutes on Ze13X. These saturation results can be used to analyze the effect of varying pressure during the desorption process.

With the adsorbent volume in the column known to be 0.04 m^3, and the densities of AC and Ze13X, it is possible to compare the adsorption capacities:

$$V_{\text{adsorbent}} = (1 - \epsilon) \cdot A \cdot L \tag{32}$$

As the densities of AC and Ze13X are respectively 842, and 1130 kg/m^3, this comparable density shows that Ze13X can adsorb significantly more CO_2 in this case: 13 mol and 157 mol respectively.

In addition, it is of interest to determine the maximum allowed breakthrough or adsorbent saturation, given that the yield/recovery of the final design should be at least 80%. Knowing that the blowdown is substituted for the equalization steps, it is clear that the CO_2 that exits the adsorber, due to breakthrough, is the major term dictating the recovery. Therefore, the adsorption time for which the loss, due to breakthrough, reaches 20% can be derived using the following ratio (and the discussed mole integrals of equation 15):

$$\text{Loss due to breakthrough} = \frac{\text{mol}_{CO_2,\text{out,ads}}}{\text{mol}_{CO_2,\text{in,ads}} + \text{mol}_{CO_2,\text{in,press}}} \tag{33}$$

Note that the pressurization time is set to 15 seconds, because in practice the duration of this step is dependent on the equipment's physical restraints and managing the operation of the whole installation (all the columns) with as little idle time as possible.

((a)) ((b))

Figure 23: Moles of CO_2 lost due to adsorbing beyond breakthrough, expressed in a loss ratio for (a) Active Carbon, and (b) Zeolite 13X

From this analysis becomes clear that the adsorption time cannot be extend longer than 107 seconds when using AC, and 771 seconds for Ze13X. Through finding these limits, the possible adsorption ranges have been identified up to which one can increase the potential purity. The resulting loading profiles are shown in Appendix Figure 53. It must be noted that thus far the obtained variables are applicable to single cycle simulations as oppose to an installation operating continuously in a Cyclic Steady State (CSS). Hence, the final values used in the cycle analysis will be shorter, due to the fact that breakthrough will occur earlier compared to a single operation with the initial conditions of a 'clean' sorbent. It was found that the initial loading conditions during CSS are two thirds of the saturation loading for AC and roughly 75% for Ze13X, which will be discussed later on.

3.2 Desorption Analysis

Researching the evacuation/desorption phase of the cycle, by solely simulating this phase with a bed saturated with CO_2, gives insight in two relevant aspects of the final design. One can determine around at which pressure CO_2 starts to desorb. This is the pressure reduction that the equalization step(s) should achieve to remove as much gas as possible without losing adsorbed CO_2. It is also of interest to derive a desorption pressure for which the marginal gain in recovered CO_2 is lower than the specific energy penalty. In other words, at this pressure it is ineffective and energetically inefficient to decrease the pressure any further. On the other hand, a practical desorption pressure limit should also be taken into consideration which varies from 10 to 0.5 kPa[35], [36]. Although the energy consumption will be looked into during the analysis of the complete system, one can already research the marginal gain in desorbed CO_2 with this desorption analysis.

With these goals in mind, the desorption analysis is conducted by plotting the adsorbent loading at the end of the desorption/evacuation phase, for various pressures, using the adsorbent loading data form the previous section. Resulting plots of desorption simulations are shown in Figure 24 which showcase, as expected, almost no difference in the loading at the in- and outlet because the loading profile is a straight line for the case of saturation.

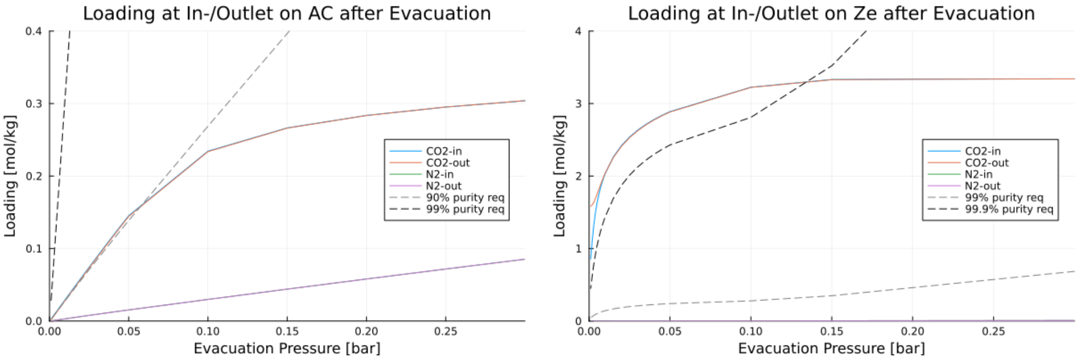

((a)) ((b))

Figure 24: Change in loading on a saturated adsorbent using different desorption pressures on (a) Active Carbon, (b) Zeolite 13X

The effect of desorption pressure on the adsorbent loading is clearly visible, starting around 0.2 bar for AC and 0.1 bar for Ze13X. What these results also show is that the linear decrease in N_2 loading on AC, and that of Ze13X, cannot be compared with these figures alone. After having zoomed in on the N_2 loading on Ze13X, shown in Appendix Figure 54, it was found that the change in loading is semi linear, and slightly higher in magnitude compared to that on AC due to the higher isotherm. In combination with the much higher CO_2 adsorption capacity, this shows that Ze13X has a significantly higher potential of meeting the purity performance indicator of this study. This can be further explained by calculating the potential purity that is possible by only considering the adsorbent loading:

$$\text{Purity} = \frac{q_{CO_2}}{q_{CO_2} + q_{N_2}} \tag{34}$$

Taking Active Carbon as example at a desorption pressure of 0.2 bar, one can estimate that the maximum potential purity is: 0.29/(0.29+0.065) = 82%. Note that this is a theoretical limit, and a measure of selectivity, which can only be achieved when the bed is fully regenerated, which in practice does not happen. Still this approach is useful to analyze at which pressure a given purity goal, p, can be achieved; by creating tangent lines for the required CO_2 loading, given the impurity loading.

$$q_{CO_2} = q_{N_2} \cdot \frac{p}{1-p} \tag{35}$$

This tangent line expression has been used to test the potential maximum purity, which is shown in Figure 24. From these results can already be seen that without equalization steps a maximum purity of 90% is possible for AC when using desorption pressure of 0.06 bar or lower, whereas 99.9% is possible for Ze13X at 0.14 bar or lower. Note that the tangent lines for Ze13X are not straight lines, because of the nonlinear relation of N_2 adsorbent loading with desorption pressure.

Continuing the desorption analysis, similar tests can be done for the case of breakthrough. Doing so, allows one to verify if the found pressure ranges are indeed suitable for the final design. It must be noted that these calculations require the use of the average adsorbent loading over the column, knowing that the loading (and gas concentration in the column) is not saturated for these scenarios. The loading profiles for the breakthrough scenario are shown in Figure 25. Furthermore, the respective loading profiles can be compared, after integrating over the column length to the saturation loading to quantify how much of the bed is used. For AC at breakthrough the bed is 66.4% saturated whereas for Ze13X only 40.3% is saturated.

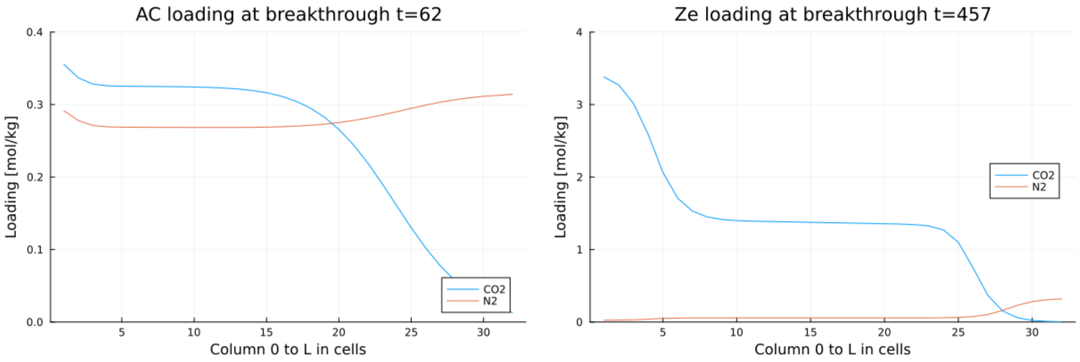

((a)) ((b))

Figure 25: Comparison of the adsorbent loading at 4% breakthrough on (a) Active Carbon, (b) Zeolite 13X

The results of the breakthrough scenario are shown in Figure 26, where a similar approach has been used to check the required loading for a given purity goal. From these figures can be seen that the same purity goals can be met with Ze13X, albeit at impractically low desorption pressures. In other words, the regeneration becomes too difficult due to the lower initial adsorbent loading. For AC the regenerative effects of varying desorption pressures is not significantly altered, compared to the saturated case, although, the maximum potential purity has decreased. That Ze13X has more drastic changes in the loading-pressure relation can be explained due to the larger contribution of the second adsorption front, shown in Figures 22 and 25.

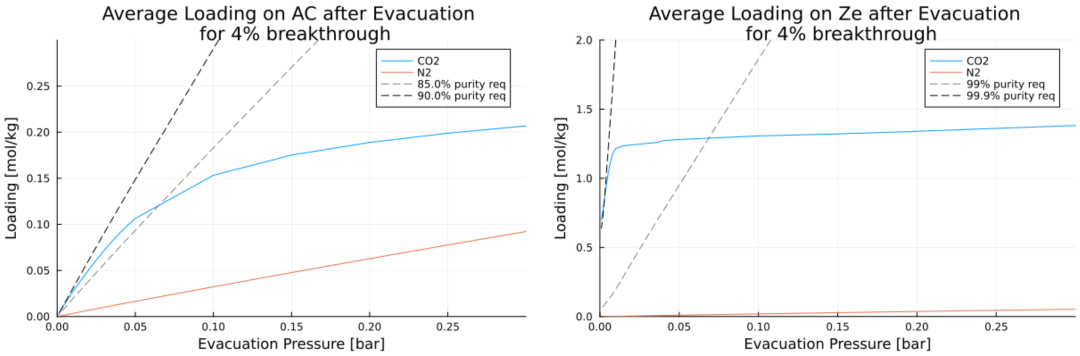

((a)) ((b))

Figure 26: Change in adsorbent loading for the case of 4% breakthrough using different desorption pressures on (a) Active Carbon, (b) Zeolite 13X

In addition, both Ze13X cases show that the majority of the total loading (at near vacuum pressures) is difficult to desorb which coheres with the stronger molecular interections between CO_2 and Ze13X and the shape of the isotherms shown in Figure 6. Consequently, these results showcase that the desired equalization depth and evacuation pressures remain the same for AC but are dependent on the adsorption conditions when using Ze13X. Hence, for AC wether or not to adsorb beyond breakthrough depends on the magnitude of the benefits of the equalization phase, whilst, for Ze13X doing so also offers the benefit of having more practical desorption conditions.
Another case can be looked into to test the maximum allowed saturation level for the given minimum yield/recovery goal as discussed in Section 3.1. Extending the adsorption until the yield requirement limit shows that the purity loadings can be met at higher desorption pressures, which is makes the operating conditions more feasible. In contrast, the adsorbent bed is now 90.4% saturated for AC and 54.2% for Ze13X. Through the results of these desorption case studies, it is expected that the desorption is most productive, for both adsorbents, at pressures of around 0.05 bar, and this expectation will be evaluated during the cycle analysis.

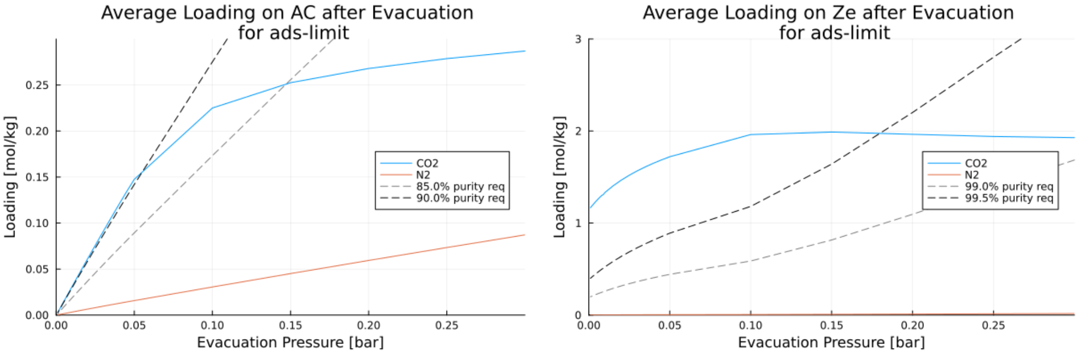

((a)) ((b))

Figure 27: Change in adsorbent loading for the case of minimum yield using different desorption pressures on (a) Active Carbon, (b) Zeolite 13X

Before researching the effects of the equalization phase, it is of interest to study desorption by varying the total desorption time to test which duration results in the minimum requirement to achieve full desorption results. As explained previously, adsorption and desorption are not kinetically limited and only flow velocity influences the pressure loss. The adsorbent loading reaches a homogeneous distribution as the desorption time is extended, although this may bring differences in loading profiles for shorter desorption times this does not influence the net amount of gas extracted from the column/adsorbent. A rule of thumb can be used to set the desorption time to 1.5, or 2, times the adsorption duration, depending on the adsorbents affinity to the components[19]. Since AC and Ze13X have a high affinity towards CO_2, the desorption duration is set to 2 times the adsorption duration.

3.3 Cycle Analysis

Following the Adsorption and Desorption analysis, the remaining phase of interest is the equalization which is analyzed through simulating the whole system in cycles. The individual pressurization phase is of less interest, since the pressurization is solely dependent on what is physically possible with the installation's equipment (compressor dependent pressurization time and flow velocity that needs to be low enough not to harm/loosen the adsorbent material packing inside the column). Moreover, the same holds for the duration of the equalization phase that has been set to 15 seconds. Therefore, the equalization phase is solely analyzed on its effect on adsorbent loading.
Furthermore, the equalization pressure relation, from Equation 31, that was found through mass balance iterations, shows that the desired equalization depth is already achieved at the desorption pressures of interest. Hence, only 1 equalization step will be used in this analysis. Note that using more equalizations steps is definitely possible, although, each added step increases the amount of required columns as well as the systems complexity and costs. This trade-off led to the decision to research only 1 equalization step. Additional information on the contribution to the equalization depth with each added step is discussed in detail in Appendix A.2.
As the benefits of using an equalization step have been discussed in Section 2.5, the goal of this part of the study is to validate these benefits in the context of the desorption pressure range derived from the desorption analysis. With the latter in mind, an example cycle case on Ze13X with a desorption pressure of 0.03 bar (an thus an equalization depth/pressure of $\sqrt[1.42]{1 \cdot 0.03} = 0.1\text{bar}$) and the minimum yield adsorption duration has been analyzed. Similar to the results of a different study, shown in Figure 12, the loading profiles after adsorption, equalization, and evacuation are plotted in Figure 28.

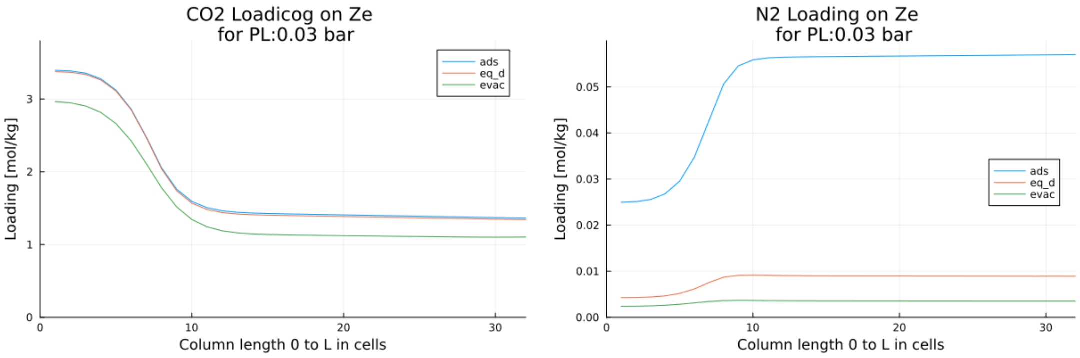

((a)) ((b))

Figure 28: Loading profiles of (a) CO_2 and (b) N_2 after adsorption, equalization, and evacuation on Ze13X using a desorption pressure of 0.03 bar

Since the conditions are similar, it can be seen that the loading profiles after adsorption are identical to the adsorption case study in Figure 53, but differ from Figure 12 as this case was simulated for cyclic steady state operation. Despite this, the reduction in N_2 loading is clearly visible whilst that of CO_2 is maintained. As such, the yield & purity benefits of using an equalization step are demonstrated. This single cycle case can be compared to its CSS operation, which will result in close to saturated operation due to the over-extended adsorption duration. Yet doing so, allows quantification of the correct initial loading conditions by recording the loading & gaseous concentrations after re-pressurization.

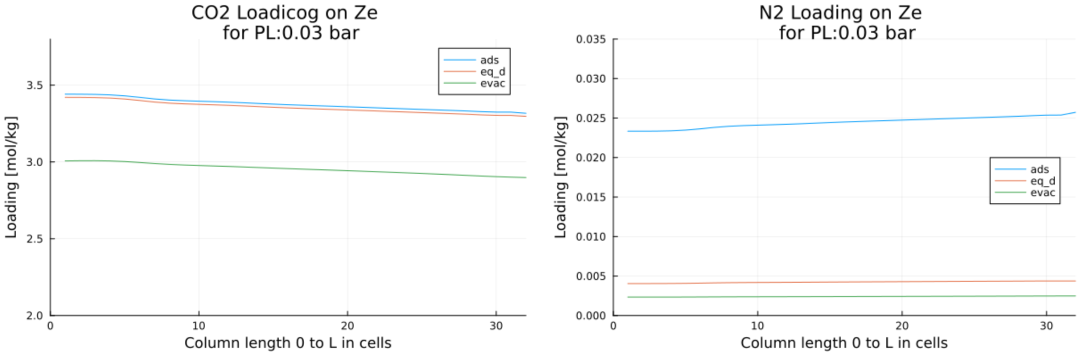

((a)) ((b))

Figure 29: Loading profiles of (a) CO_2 and (b) N_2 after adsorption, equalization, and evacuation on Ze13X using a desorption pressure of 0.03 bar during Cyclic Steady State (CSS) operation

The loading results for CSS operation are shown in Figure 29. This close to saturation case, verifies that a large portion of the on Ze13X adsorbed CO_2 is not regenerated. Moreover, knowing that this CSS operation achieves a purity of 99.3% purity with an over-extended adsorption time showcases that 1 stage is not enough to reach the foodgrade-purity goal. It may also be noted that the purity can be roughly estimated by subtracting the loading differences from the equalization down phase and that of the evacuation phase: $\frac{0.4}{0.4+0.002} = 99.5\%$. Regarding the initial loading conditions, it was found from several cases such as seen in Figure 29 that the initial loading is 2.9 mol/kg for CO_2 and 0.005 mol/kg for N_2. These initial conditions, as well as for those for AC, are used as an interpretable measure since, in practice, the concentration- and loading profiles at the end of the pressurization phase are used as more accurate initial conditions in the model (an example of these profiles is shown in Appendix Figure 55). A similar case can be studied for AC which verified that CO_2 is easier desorbed, given the flatter isotherm (weaker molecular interactions). These results are shown in Figure 30. A higher desorption pressure was used, namely 0.05 bar, ensuring that the equalization pressure is not too low although some CO_2 is still desorbed (the equalization in this case is 0.29 bar in this case).

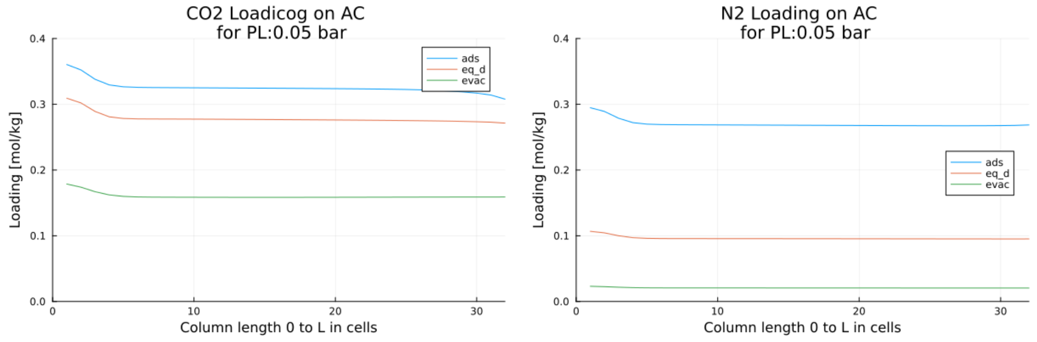

((a)) ((b))

Figure 30: Loading profiles of (a) CO_2 and (b) N_2 after adsorption, equalization, and evacuation on AC using a desorption pressure of 0.1 bar

Lastly, this case for AC with an over-extended adsorption time achieves a 56% purity and the initial loading conditions resembling CSS operation are 0.25 mol/kg for CO_2 and 0.21 mol/kg for N_2. Both loadings are close due to the similar adsorption isotherm data at the feed concentration (with which the column is pressurized). These results can be used to correct the maximum adsorption time for steady operations, and form a basis for the design of a 2 stage vacuum pressure swing adsorption cycle. Considering the CSS loading conditions, the adsorption limits are changed according to the adsorption analysis shown in Figure 31. Note that this Figure can also be regarded as the loss percentage plotted against the dimensionless time, which is the time divided by the residence time $\bar{t} = \frac{t}{t_{res}}$, because the residence time is 1 second for a feed velocity of 1 m/s.

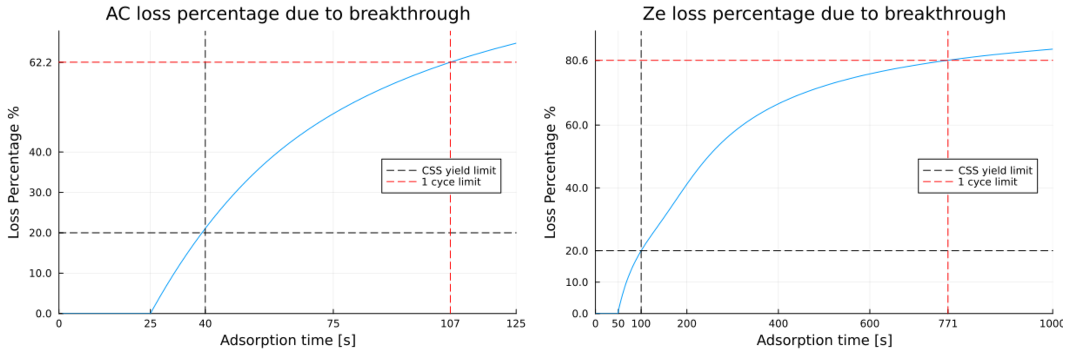

((a)) ((b))

Figure 31: Moles of CO_2 lost due to adsorbing beyond breakthrough, expressed in a loss ratio for (a) Active Carbon, and (b) Zeolite 13X, showcasing that only a part of the adsorbent bed is regenerated which as a consequence requires the adsorption time to be reduced during CSS operation

In these Figures, both the corrected adsorption durations and the former ones are shown indicating that a CSS operation using former settings would allow too much breakthrough. As be seen, the larger initial loading conditions result in considerably shorter adsorption duration approaching saturation more quickly. Also, it is worth mentioning that lowering the feed velocity will also help in reducing the loss due to breakthrough. For example, lowering the feed velocity to 0.5 m/s resulted in a maximum adsorption duration of 21 seconds. The corrected CSS case simulations are shown in Appendix Figure 55, for which the case of Ze13X produced a yield increase to 91.8% with the purity dropping to 98.7% (and a promising energy consumption of 116 kWh/ton$_{CO_2}$).

In conclusion, all parameters have been analyzed individually which provides the required information to formulate a final design for the dry flue gas. Since the parameter study has proven that a single stage will not be able to meet both requirements, the Section 4 discusses the results of a multiple stage design.

3.4 Wet Operation Conditions

Thus far, all considered cases have been made for dry flue gas conditions, although, the real SMR flue gas does contain water vapor. These can either be condensed out of the gas stream, or could be separated by making use of its high affinity with AC in a VSA cycle. There are two possibilities regarding the placement of this drying process; the first is to consider operating the first recovery stage with AC in wet conditions and condensate the water before going to the purity stage. Second, is to have a designated drying stage before the whole process itself as was shown in Figure 13. Again, with the latter option it is still open to choose a VSA cycle or, for example, a gas liquid separator. As a means to limit the energy consumption and the amount of complex components in the design, it is preferred to operate the first recovery stage in wet conditions and use a gas-liquid separator (and a cooler if needed) to remove enough water vapor such that it does not dissolve the Zeolite adsorbent used in the second stage. This design choice brings two additional advantages, assuming that a cooler is required. First, the required cooling duty is lower in this configuration as oppose to a gas-liquid separation prior to the first stage since the amount of gas that needs to be cooled is less. Second, decreasing the temperature benefits the adsorption process which is exploited better for increasing the purity at the second stage compared to the first stage.

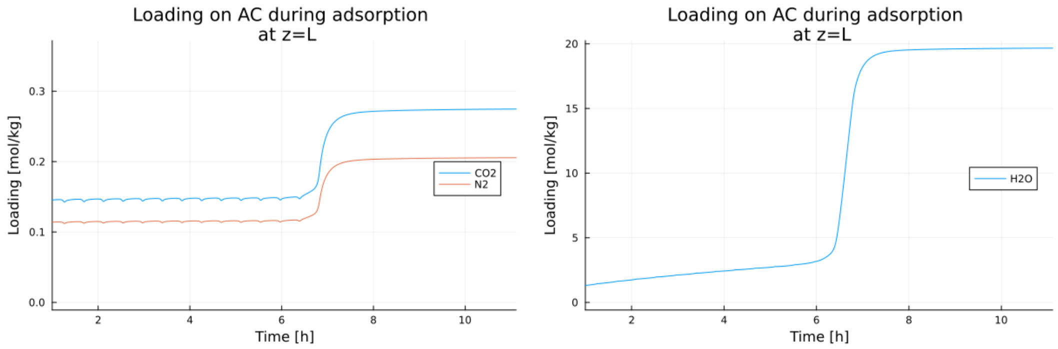

((a)) ((b))

Figure 32: Adsorption analysis in humid conditions on Active Carbon, showing (a) CO_2 and N_2 loading, (b) H_2O loading over adsorption time in hours

Regarding the considered dry gas scenarios with a gas stream of 15/85% (CO_2/N_2), a flue gas with a relative humidity of 100% is assumed to have a composition of[32]: 12/84/4% (CO_2/N_2/H_2O). It may be noted that any higher content is not considered, as in that case (partially) liquid water would be pumped through the system. Performing the discussed steps in the parameter study can be done for this mixture, even though it should kept in mind that, due to capillary condensation, the water adsorption capacity is 55 times larger than that of CO_2 ($\frac{19.9}{0.36} = 55$). Therefore, the amount of cycles it takes for water to break through, and to obtain CSS operation, is significantly longer.

This effect is observed when adsorbing a column, initially filled with N_2, until saturation, which can be seen in Figure 32. From the saturation profiles can be seen that the adsorption capacity of CO_2 and N_2 is slightly lowered due to the presence of water, as confirmed in available literature[32]. Similar to previous cases, the gas concentration and loading profiles in the column can be initialized to that of the post-pressurization phase when CSS is reached. The desorption analysis showed similar desorption behavior on AC for CO_2 and N_2, whereas the desorption of water showed far steeper desorption patterns as a result of its stronger interaction/adsorption. These patterns are shown in Appendix Figure 57.

In addition, the equalization pressure relation for AC has been revised since the presence of water vapor changes this behavior. Operating for the same pressure range, resulted in a pressure function of: $P_I = \sqrt{P_H \cdot P_L}$. Further optimization of the cycle design is discussed in Section 4, for which some aspects need to be kept in mind. Firstly, the purity goal for the product gas is lowered due to the presence of water. For example, a desorption product of 30/20/50% (CO_2/N_2/H_2O) for the first stage can be dried, using an ambient gas-liquid separation, allowing the liquid fraction of the water in the

mixture to condensate out of the stream, to a composition of 58/40/2% ($CO_2/N_2/H_2O$). The second aspects concerns the water content of the product stream as well, because this must be low enough to prevent breakthrough of the water front in the second column. In case this can not be assured, water-zeolite degradation will take place. These dynamics have been studied in available literature, which report a reduction in CO_2 adsorption capacity due to the competitive adsorption (and capillary condensation) of water vapor up to 98% depending on the water's partial pressure or relative humidity[48],[49],[50].
If the water content appears to be to high for the second stage, then the product gas of the first stage could be cooled to remove more water. The flowsheet analysis that is used to calculate the required cooling duty, and resulting water content, is shown in Appendix Figure 58. Since this method brings an additional power requirement, another option is to add a layer of activated carbon can be used at the inlet to protect the zeolite. The latter can be simulated using two adsorber columns place in series as was shown in Figure 13. Testing whether these measures are required is done through simulating the adsorption process individually on Ze13X for different water contents, until a concentration at which the water front does not break through. Next, this concentration can be used to derive the required cooling duty (with the flowsheet of Appendix Figure 58).

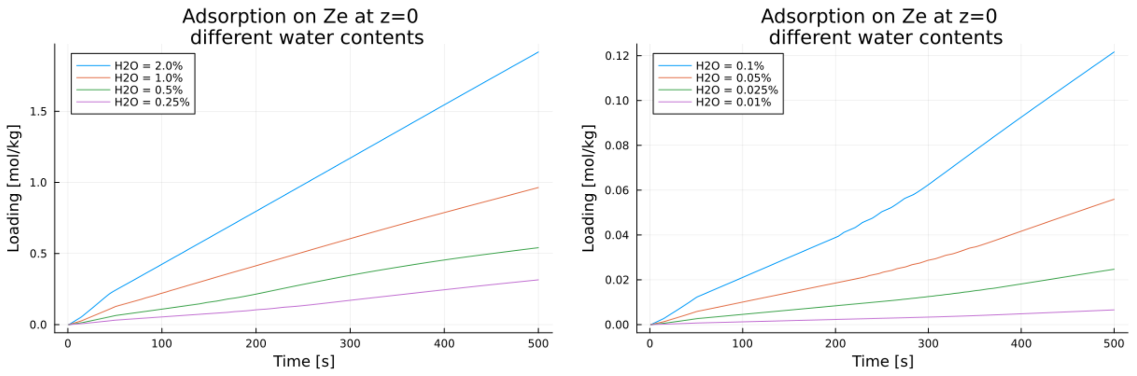

((a)) ((b))

Figure 33: Adsorption of water on Zeolite 13X during the first 500 seconds, starting from a clean bed, for different water concentrations in the feed

The results of this test are shown Figure 33, that depicts the loading at the column inlet during the first 500 seconds. From which can be seen that cooling is indeed required to lower the water content to at least 0.01% (mole fraction y_{H_2O}=0.0001, and a relative humidity of 0.46% at 298K). Using the DWSIM flowsheet, shown in Appendix Figure 59, it was found that this can be achieved by cooling the example product stream of 30/20/50% ($CO_2/N_2/H_2O$) from 298K to 233K which requires 22kW. Knowing that lower temperatures benefit adsorption, it was tested what the adsorption process would be like at this range. Simulations showed that after 3000 seconds still only 0.04 mol/kg was adsorbed at the column inlet, whilst the adoption of CO_2 increased to 4.4 mol/kg. On the other hand, achieving such a temperature change of 60K, well below freezing temperatures, was deemed impractical. Hence, the final design will have a column with AC placed in series before the purity column with Ze13X. This configuration was shown in Figure 13, and makes sure that the dry breakthrough gas of the protective layer enters the column with the zeolite. The same could potentially be achieved by having a layer of AC at the inlet of the zeolite column itself, although, further studies would be required to design a cycle in which the water that is regenerated does not re-adsorb on the zeolite.
Lastly, it should be noted that some CO_2 will be adsorbed in this drying stage/layer. Regarding this process in separate columns, it should be checked if this gas stream should be recycled as well to maintain the recovery target.

4 Multi-Stage VSA Design

The next step is to combine the obtained information, from the case studies, to formulate the an optimized carbon capture design. The discussed methods from Section 3 are used to analyze several designs that consists of a recovery prioritizing stage and a purity stage. In order to achieve high CO_2 purity, the cycle design must operate close to saturation conditions. Therefore, it is required to recycle the breakthrough gas back to the recovery stage. This design parameter, together with for example the energy consumption per stage need to be checked in the optimization process. For the recovery stage, the wet flue gas is fed to a column packed with AC to enrich the CO_2 product stream without compromising yield and minimizing the energy consumption[51]. There is no initial gas-liquid separator because the 100% relative humidity conditions also offer competitive adsorption with N_2 which is beneficial for the CO_2 enrichment. The product stream is directed to a gas-liquid separator to remove the majority of the water. At 298K the water content will be reduced to a mole fraction of 2%. Although this could be reduced through cooling the gas stream, it was found that cooling on its own is not enough. Several design configurations have been tested, out of which two designs have shown potential. After the gas liquid separator either a multi-layered adsorber stage can be used, or two columns have to be place in series such that the first column practically servers a dryer column. These two design options and the initial stage are discussed below. It may be noted that the column parameters of Appendix Table 9 are used, such that the column has an inner radius of 0.1445 m, a length of 1 m, and a volume of 0.066 m^3.

4.1 Recovery Stage

As for the recovery stage, it was found best to use a column fully packed with AC. The studied parameters have been optimized for the obtainable purity and energy allocation. Depending on the operating conditions of the second part, the optimal adsorption duration of the recovery stage can be selected. The same can be said for the used desorption pressure for this cycle, because the combination of these two parameters dictate the CO_2 concentration of the gas fed to the next stage as well as the recovery of the whole system (assuming that the CO_2 lost in the second stage is recycled). In addition, the energy consumption per cycle is recorded for the final energy consumption in kWh per ton of captured CO_2. Together these aspects form an optimization problem since allocating more energy to the first stage enables lower operation pressures for a better purity which may improve the functionality of the second stage. To make sure that the desorption pressure, and the resulting equalization pressure, does not drop to a level at which CO_2 is regenerated, it has been decided to use desorption pressure no lower than 0.05 bar[52]. In the context of the multi-layered stage design, it was found that an adsorption duration of 80 seconds, and a desorption pressure of 0.07 bar, gives a product stream of 29.1/8.6/62.1 (CO_2/N_2/H_2O) with a yield of 88.0% (as 12.0% was lost during breakthrough).

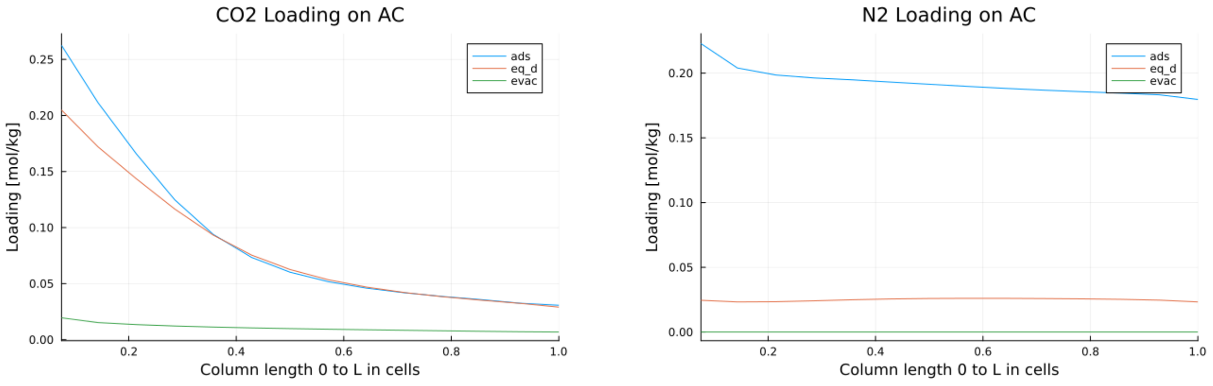

((a)) ((b))

Figure 34: Recovery stage loading profiles of (a) CO_2 and (b) N_2 after adsorption, equalization, and evacuation

The amount of CO_2 lost due to breakthrough has been reduced through both the adsorption time as well as the feed velocity which was set to 0.25 m/s, which means the gas has a residence time of 4 seconds. The majority of the water content in the product stream is removed by using a gas-liquid separator. The remaining amount of water is 2.2%, due to which the purity increases to 72.9%. Thus, a product stream of product stream of 72.9/24.9/2.2 ($CO_2/N_2/H_2O$). Regarding the recycle stream of the purity stage, and assuming that volumes are matched with reservoirs/tanks in the real-life process, it can be derived that the feed concentration of the first stage would increase roughly up to 30% CO_2. For this setup the energy consumption is 0.0386 kWh per cycle. This energy penalty is combined with second part of the process where purity is prioritized.

4.2 Purity Stage Options

The first option required one additional stage, and is therefore less complex and cheaper. As shown in Figure 35 after the gas-liquid separator, a multi-layered column packed with a 20% AC and 80% Ze13X is used. The layer of AC serves as a protective layer to maintain the adsorption capacity of CO_2 on Ze13X. The desorption pressure at this stage is 0.18 bar, since lower pressures desorb too much water, from the protective layer, decreasing the purity. In terms of energy, most is allocated to the first stage to enhance the purity in wet conditions as much as possible. This and other design parameters are presented in Table 6.

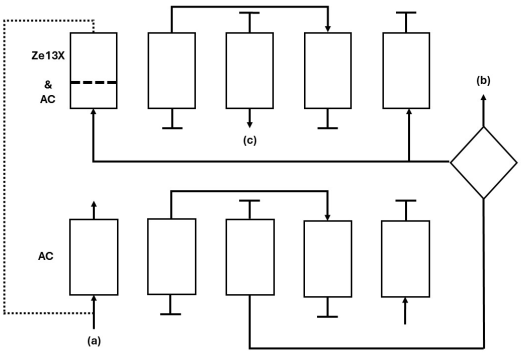

Figure 35: Flow diagram of the multi-layered stage design option, where the wet flue gas (a) is mixed with the recycle stream and fed into the first stage, the product stream is passed through a gas-liquid separator where water is removed (b), the final product stream of the second stage is obtained at (c)

The loading profile after adsorption is shown in Appendix Figure 60, that shows how the water in CSS does not reach the zeolite. Although this design is relatively simple, the best obtainable purity is a product stream of 95.3/0.0/4.7% ($CO_2/N_2/H_2O$) with a total energy consumption of 122.8 kWh/ton_{co_2}. Cooling the gas to improve the gas-liquid separation, and enhance the adsorption process, has been tested as well but that significant effects require too much energy. Similarly, the adsorption has been simulated with elevated pressures up to 1.5 bar but did not show significant improvements. Moreover, the purity limit of this design can be explained through the fact that there is always some water regenerated from the protective layer.

Table 6: Optimized parameters for the multi-layered design, with the energy consumption for a blowdown cycle reported in (brackets)

Stage	**Feed [$CO_2/N_2/H_2O$]**	**Desorption Pressure [bar]**	t_{ads}	**Product [$CO_2/N_2/H_2O$]**	**Yield [%]**	**Energy Consumption [kWh/Cycle]**
Recovery	12.0/84.0/4.0	0.07	85	29.1/8.6/62.1	88.0	0.0386 (0.0652)
Purity	72.9/24.9/2.2	0.18	90	95.3/0.0/4.7	56.3	0.0245 (0.0485)

Even though the best obtainable product stream does not directly adhere to the food-grade CO_2 purity requirement, this design is still useful as the product stream only needs to be dried in order to reach food-grade CO_2 purity. The combination with CO_2 liquefaction is promising to offer a full carbon capture and storage (CCS) process. This step is also required to achieve HyGear's goal of producing sustainable hydrogen. Hence, the captured carbon may be cooled to lower the water content below 50 ppmv, which is required for CO_2 liquefaction. Therefore, the combination with the proposed VSA design might be a cost effective system to obtain food-grade purity liquefied CO_2, since cooling the gas to sub-zero temperatures is already part of the CO_2 liquefaction process.
The second option consists of three stages, with two recycle streams as shown in Figure 36. The gas exiting the gas-liquid separator is directed to the second part of the system, where two columns are placed in series to ensure that no water is adsorbed onto the zeolite adsorbent. Although more complex, and costly, this configuration solves the issue of the multi-layered design since the water is dealt with in a separate stage.

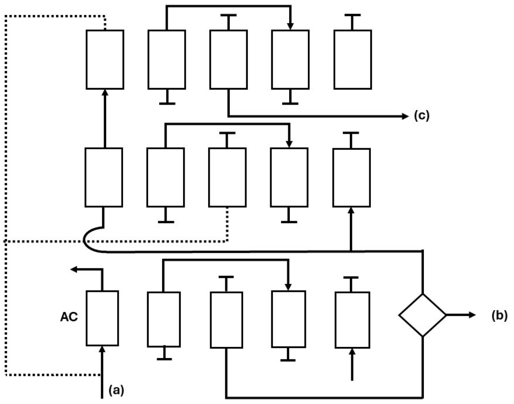

Figure 36: Flow diagram of the dryer column design option, where the wet flue gas (a) is mixed with the recycle streams and fed into the first stage, the product stream is passed through a gas-liquid separator where water is removed (b), the final product stream of the second stage is obtained at (c)

Any CO_2 lost in breakthrough, or in the product stream of the dryer column, should be recycled. In doing so, each stage is optimized for which mainly the energy requirement is challenging to meet. When comparing designs, it is clear that the multi-layered system has a significant advantage in terms of simplicity and costs. Limiting the system's size is of key importance in terms of CAPEX and, knowing that HyGear sells their systems in container sized modules. With the CO_2 liquefaction as the next step in the carbon capture (and storage) process, it is therefore determined that the multi-layered design is the most suitable carbon capture process design. This design and the respective flow compositions, is shown in more detail in Figure 37.

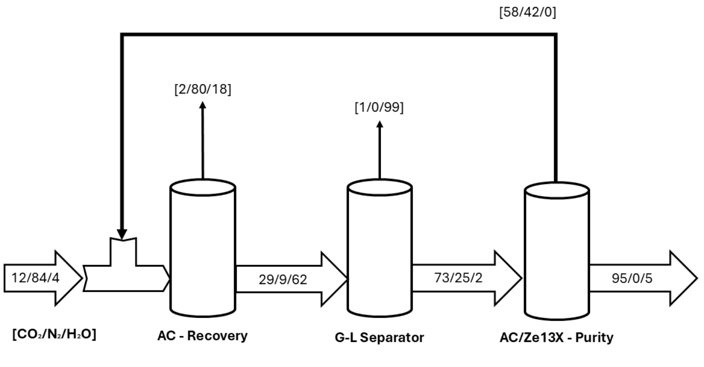

Figure 37: Overview of the final design, showing the concentration of the feed, breakthrough, and product streams of the individual components

4.3 Energy Savings

Blowdown system equivalent for the proposed designs can be simulated to compare the energy requirements. For this comparison the yield decrease due to blowdown is neglected. The first stage was found to require 0.0652 kWh per cycle to increase the concentration of the product stream to 73% CO_2. Doing the same for the multi-layered purity stage, it was found that 0.0485 kWh per cycle was required. It may be noted that the energy per mass unit is a biased comparison since a larger part of the CO_2 is lost in the blowdown system. Looking only at the energy per cycle requirement it can be seen that the equalization design brings a 43.3% energy reduction (in terms of kWh/cycle). Furthermore, the energy comparison is shown in more detail in Figure 38 which also show that the energy requirement of the adsorption and pressurization phases are negligible compared to the blowdown and evacuation steps. Note that for this figure, the mass output of the equalization design is used in order to show the energy requirement of the equivalent blowdown cycle.

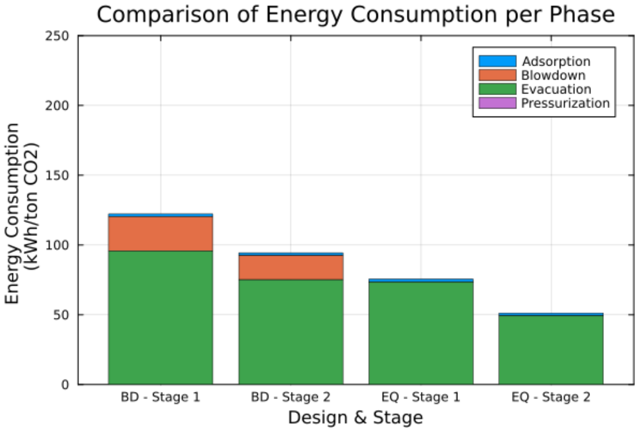

Figure 38: Histogram showing the difference in energy comparison, where the blowdown energy requirement is calculated with the mass output of the equalization cycle

4.4 Possible spread of CO_2 concentration

The possible spread of CO_2 can be derived by determining the minimum and maximum CO_2 inlet concentrations for which the optimized design achieves food-grade purity. For larger CO_2 concentrations the adsorption time has to be watched to prevent potentially earlier breakthroughs, although this effect mainly plays a role on Ze13X as shown in the adsorption analysis of Figure 52. On the other hand, for lower CO_2 concentrations the adsorption time could be changed as well as the desorption pressure. In doing so, the power consumption increases which still has to meet the maximum requirement. Since lower feed concentrations result in lower adsorption loadings, it could also be useful to consider increasing the adsorption pressure. The minimum CO_2 concentration in the first stage is determined by the minimum concentration that the second stage requires to reach the purity goal. This was found to be 70%. With this information, the possible spread of CO_2 in the feed was found to be 8% because the energy requirement cannot be met for lower concentrations.

4.5 Fluidization Velocity

Developed process designs have to be checked on safety measures, to ensure technical and economical feasibility. For these designs the most important measure is the minimum fluidization velocity. For this velocity, the velocity of the gas/fluid is strong enough to lift the adsorbent particles and release them from the bed. Hence the feed velocity must always be, with a safe margin, lower than the minimum fluidization velocity V_{mf}. This minimum fluidization can be derived from the Ergun equation:

$$(\rho_s - \rho_g)\, g = \frac{150\,\mu\, V_{mf}\,(1-\epsilon)}{\phi_s^2\, D_p^2\, \epsilon^3} + \frac{1.75\,\rho_g\, V_{mf}^2}{\phi_s\, D_p\, \epsilon^3} \tag{36}$$

Throughout the entire process the gas density varies between 0.9 and 1.6 kg/m^3, and the particle sphericity, ϕ_s,is assumed to be equal to 1. The remaining parameters are given in Appendix Table 9, which can be used to solve Ergun's equation for the fluidization velocity. From the two adsorbents AC has the lowest density, in combination with the densest gas density, the minimal fluidization velocity is conservatively estimated to be 0.43 m/s. With a margin of almost 50%, it is confirmed that the VSA cycle design functions in feasible operation ranges when using a feed velocity of 0.25 m/s.

4.6 Column Dimensioning

The final design is specified for HyGear's flue gas conditions, although the column dimensioning is still based on a case obtained from available literature[34]. Therefore, the column dimensions can be altered considering a system designed to handle 1000 m^3/h (0.28 m^3/s) of this flue gas. Maintaining operation conditions and a feed velocity of 0.25 m/s, it can be found that the required diameter of the columns is 1.2 m. The radius to column length ratio of the simulated columns is 0.1445, subsequently the column length becomes 4.2 m. From this can be concluded that these columns will not fit into standardized containers for which HyGear designs their systems.

Smaller column dimensions with the same performance are obtained when assuming that larger feed velocities can be used if the residence time is maintained (which is 4 seconds). By a feed velocity of 0.4 m/s, it can be derived that the inner diameter decreases to 0.9 m and the required length to 1.6 m (thus a volume of 1.1 m^3). This feed velocity is possible under the assumption that the fluidization velocity was calculated to conservatively, or that a down-flow system is used (for which much higher feed velocities are possible). These column dimensions are more realistic and used in the next section to perform an economic analysis of the system.

5 Economical Analysis

With the proposed design, it is possible to perform an economical analysis to estimate the CAPEX and OPEX of the system. Doing so is done by through calculating the costs of the columns, the required (vacuum) compressors, and the adsorbent costs. For these calculations it is estimated that the installation has a service time of 15 years. In terms of OPEX, the energy consumption of the system can be used to determine the electrical costs of the system together with a maintenance estimate. The energy requirement of the compressors and vacuum pumps form the most important component of the operational costs because there are no other significant appliances that require heat and/or power. It may be noted that the overall costs of manpower are taken out of this analysis, and that the prices are derived excluding taxes. The CAPEX and OPEX cost calculations are combined to derive a cost per kilogram of captured CO_2 which can be compared to cost estimations found in available literature.

5.1 CAPEX

The total capital investments are derived through the deriving the costs of the columns, (vacuum) compressors and gas-liquid separator individually. Estimating these costs is done using a cost estimation report with data from 1998[53]. Hence, the prices need to be indexed using the Chemical Engineering Plant Cost Index (CEPCI):

$$\text{Price}_{2025} = \text{Price}_{1998} \cdot \frac{\text{CEPCI}_{2025}}{\text{CEPCI}_{2002}} = \text{Price}_{1998} \cdot \frac{800}{389.5} \tag{37}$$

There are four adsorber columns required for the design. As discussed in Section 4.6, the columns have an inner diameter of 0.9 m and a length of 1.6 m. The total length of the column is estimated to be 2.0 m, by assuming that there is additional room needed for a layer of inert material to ensure a uniform flow profile as shown in Figure 39. Furthermore, a wall thickness is assumed to be enough as the columns are not subjected to large pressures.

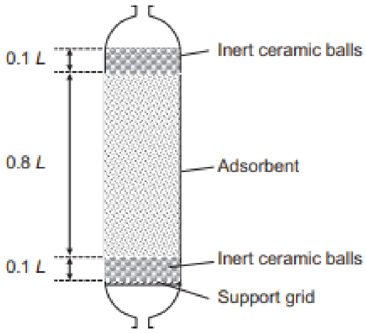

Figure 39: Adsorption vessel internals[54]

To account for the cost that are included for the whole column design (heads, supports, piping etc.) the cost relation in Appendix Figure 61 can be used to derive that the costs of one column (of 1.1 m^3 or 294 gallons) are \$8,400 which equate to €15,800 after indexing. The indexed packing prices for AC, Ze13X and ceramics are not taken into a count as they are negligible compared to other cost factors; namely 0.74, 1.32, 3.21 €/m^3 respectively[53]. In order to cope with the humid conditions, stainless steel 304 is used which has a material factor of 1.3. Assuming that the columns do not need replacement, an installation factor of 4 gives that the total costs for the four columns are €330,000. As for the gas liquid separator, a cost assumption is made based on a small tank of 0.05 m^3. The cost relation for a carbon steel vertical vessel, shown in Appendix Figure 61, is used. Again a material factor of 1.3 is applied for Stainless Steel 304, in combination with the six-tenths rule estimate the costs for the right volume. After indexing, and using an installation factor of 4, the price of the gas liquid separator is estimated to be €17,500.

Two compressors for the adsorption and pressurization steps, and two vacuum pumps for the desorption are required, because the design consists out of two stages. Design conditions for the compressor are based on the flue gas flow of 1000 $\mathrm{Nm^3/h}$, at atmospheric pressure, so given the relatively low pressure ratios a rotary blower is most suitable. The cost estimate, is derived using lang factors and current pricing used by HyGear[55]. The cost estimate is made using the $6/10^{\mathrm{th}}$ rule, knowing that a blower with a capacity of 4000 $\mathrm{Nm^3/h}$ currently costs €60,000:

$$\mathrm{CAPEX_{Blowers}} = 60,000 \cdot \left(\frac{1000}{4000}\right)^{0.6} = 26,116.52 \tag{38}$$

Using a lang factor of 2.5, the total capital costs for the blowers are €131,000.
The vacuum required vacuum pumps are based on the required capacities, that are derived form the velocity profiles of the final cycles. The recovery stage has a higher actual capacity than the purity stage, because of the lower desorption pressure higher relative humidity and the fact that it is the first stage of the separation process: 4225 and 1825 $\mathrm{m^3/h}$ for the recovery and purity stage. Another price relation given by HyGear, can be used in the six-tenths rule. For this case it was found that a vacuum pump of 1140 $\mathrm{m^3/h}$ currently costs €20,000. Using this information for both vacuum pumps, the estimated prices were found to be €43,900 and €26,500 respectively. Using an installation factor of 2.5, the capital costs for the two vacuum pumps are €176,000.

5.2 OPEX

The operational costs of the carbon capture system are assumed to be mostly influenced by the energy costs of the process and the replacement costs of major components. Hence, the energy costs per cycle can be used to derive the total energy costs during the systems lifespan. With a two column planning for each stage, the flow matching can be estimated by taking some idle time into a count. The flow planning of the purity stage is shown in Figure 40, and it is assumed that the slightly shorter cycle of the recovery stage can operate simultaneously. As such it is derived that two cycles can be completed, for the whole system, within 420 seconds (bed 1 has an idle time of 70 seconds and bed 2 of 60 seconds).

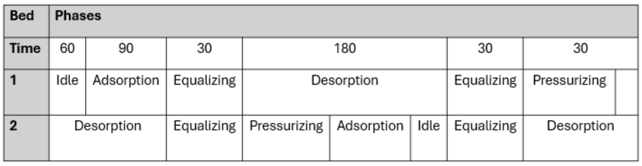

<table>
<tr><th>Bed</th><th colspan="8">Phases</th></tr>
<tr><td>Time</td><td>60</td><td>90</td><td>30</td><td colspan="3">180</td><td>30</td><td>30</td></tr>
<tr><td>1</td><td>Idle</td><td>Adsorption</td><td>Equalizing</td><td colspan="3">Desorption</td><td>Equalizing</td><td>Pressurizing</td></tr>
<tr><td>2</td><td colspan="2">Desorption</td><td>Equalizing</td><td>Pressurizing</td><td>Adsorption</td><td>Idle</td><td>Equalizing</td><td>Desorption</td></tr>
</table>

Figure 40: Column planning of the purity stage when using two columns per stage

In terms of operating time, it is estimated that the yearly downtime due to maintenance is 3 days. Which means that 2.2 million cycles are completed within the system's lifespan, requiring 144,000 kWh. The price for electricity for industrial consumption is taken as €0.1775[56]. Therefore, the operational costs are €25,600.
In terms of replacement costs, it is assumed that the major components described in the CAPEX calculation last the total lifespan of the system. Overall replacement or maintenance cost are approximated to 3% of the total CAPEX[55]. This is expected to mainly include blower & vacuum pump maintenance and replacement of valves. The valves are used intensively throughout the operation, therefore these require relatively frequent replacement to cope with degradation effects and prevent leakages. Hence, the maintenance cost is estimated to be €19,600 but can be checked for its influence.

5.3 Cost Comparison

The total costs of the carbon capture system are summarized in Table 7, and can be compared to literature by calculating the total CO_2 output of the system. Since these cost were based on rough estimations, the total costs are expected to vary with ±25%.

Table 7: Total CAPEX and OPEX of the carbon capture process, expressed in thousand euros

	Columns	**G-L-Separator**	**Blowers**	**Vacuum Pumps**	**Energy**	**Maintenance**	**Total**
CAPEX	330	17.5	131	176	-	-	€654,000
OPEX	-	-	-	-	25.6	19.6	€45,000

In the optimized design, 11.9 mol of CO_2 per cycle is extracted from a feed of 59 m^3/h. Compared to the industrial flue gas case of 1000 m^3/h, the feed is increased with a factor 16.9. This can be used to estimate that the up-scaled system can extract 202 mol CO_2 per cycle. As such the total costs can be divided by the total mass of CO_2 that is captured, which results in a price of €35.2±8.8/ton CO_2 (or €0.035±0.05/kg CO_2). This may be compared to a study of a similar scale, since larger scaled processes are more difficult to compare in costs. The best comparable study that was found is a reported a carbon capture costs, from wet flue gas, using a two-stage vacuum pressure swing adsorption process of $34.1/ton CO_2[33]. As this was published in 2015, this leads to €45.1/ton CO_2 after indexing. This study also included the costs of the CO_2 compression process (to 110 bar and 30○C). Therefore, future research on this part of the carbon capture process could give insights into the total cost comparison. Another study, also from 2015, published capture cost estimations for a 500 MW power plant of $30-37/ton CO_2[57]. This provides a range of 39.7 to 48.9 €/ton CO_2. Due to the 25% uncertainty in the cost estimate, it cannot be said whether the capture cost of the proposed design is competitive. However, these cost estimations do show a similar order of magnitude when compared to available literature.

5.4 Sensitivity

Besides having estimated the costs of the system with a uncertainty margin, it is also interesting to see how some factors influence the overall €/ton CO_2. Therefore, this section looks into four factors and how these affect the total costs. Although the cycle time is also an interesting factor, this one is not taken into a count because it not precisely known how this will affect the CO_2 output per cycle. First is the number of blowers, because operating time schedules can be arranged in such a way that the vacuum pump of the first/recovery stage is also used to feed (and pressurize) the second/purity stage. In doing so the CAPEX is reduced with 10%, resulting in a capture costs of €31.8±7.9/ton CO_2.

Figure 41: Analyzed cost sensitivity for electricity costs costs

The next to parameters of interest are the maintenance and electricity costs, since these are assumed but may changed due to overhead circumstances. Hence the total capture costs are evaluated based on increases and decreases in maintenance and electricity prices. The results of these case studies are shown in Figures 42 and 41. From this can be seen that a changing energy price can influence the capture cost with at most ±0.87€/ton CO_2.

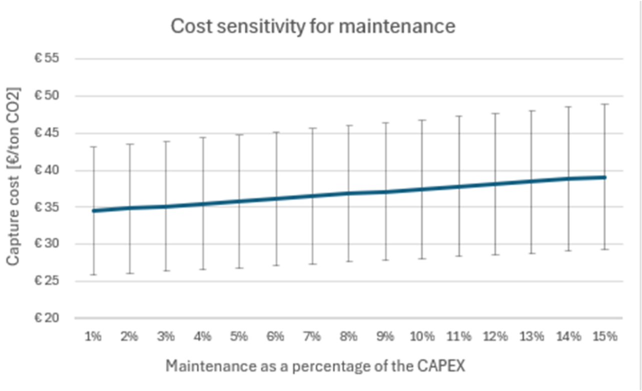

Figure 42: Analyzed cost sensitivity for maintenance costs

The maintenance cost show a more significant affect on the cost. Over the range of 1 to 15% of the CAPEX, the capture costs vary with ±2.3€/ton CO_2.
Another factor that can be tested is the effect of downtime on the capture costs, because this influences both the energy costs and the amount of CO_2 captured over the course of the systems lifespan. This sensitivity study is shown in Figure 43 where the capture costs is calculated for a range of 1 to 20 days of downtime per year. A similar effect is seen as with the electricity price analysis, since the range of annual downtime changes the capture costs, at most, with ±0.95€/ton CO_2.

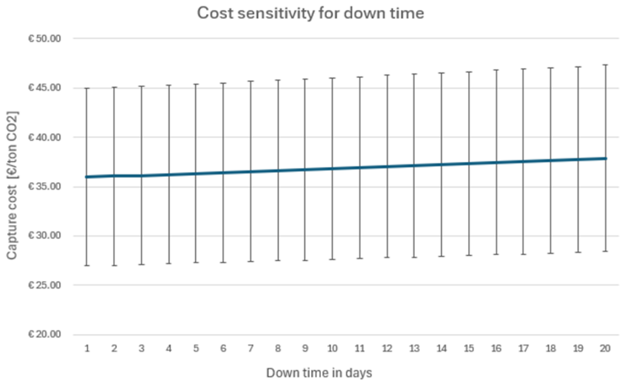

Figure 43: Analyzed cost sensitivity for annual down time

What can be concluded from this economical analysis is that the capital investments costs outweigh the operational costs. This is also seen in the sensitivity analysis, where the operational costs have a lower influence on the capture costs as oppose to system optimization measures that, for example, reduce the number of required blowers. In addition, the maintenance factor was found to be the most influential out of the 3 analyzed operational factors. Overall, the estimated capture costs are of the same order of magnitude as those reported in available literature, although, more research in this regard is required to asses the market potential/competitiveness of this system.

6 Conclusion

A dynamic vacuum swing adsorption (VSA) model has been thoroughly researched in this thesis, during which potential improvements have been identified and successfully implemented. As a result the common, four phase, blowdown cycle design has been expanded to a 5 phase equalization cycle, achieving improvements in purity, recovery, and energy consumption. Although it is made possible to include several equalization steps in the cycle design, this study showed that using one equalization step reaches the desired equalization depth for the carbon capture process. The research question is answered through proposing a VSA cycle design capable of capturing CO_2 from HyGear's steam methane reforming (SMR) flue gas that is suited for CO_2 liquefaction to obtain food-grade purity. In combination with proper carbon storage methods, the findings of this study form a road-map for HyGear to develop their blue hydrogen production technology. A two-stage design has been optimized through a detailed parameter study, identifying influential parameters and their effects on the separation process. Energy consumption has been allocated between the stages, by setting the desorption pressure, making sure the system meets the energy consumption requirement of $\leq$150 kWh/ton CO_2. The reduction in energy consumption, in comparison with the blowdown cycle, is achieved as the equalization step makes use a spontaneous equilibrium-based process. At the same time, recovery is maintained because the gas is no longer vented to the environment. Furthermore, an economic analysis of the final design has been done using the column dimensioning estimations for an industrial flow rate. The estimated capture cost in €/ton CO_2 is comparable to values reported in available literature. However, more research is required to assess to economic feasibility of a detailed carbon capture module (including the CO_2 liquefaction step).

The parameter study highlights the importance of balancing phase durations of a cycle with respect to their cyclic steady state (CSS) operation. Analyzing influential parameters in CSS simulations provided information about the optimization possibilities for the design. The latter also helped with determining the possible spread for the CO_2 content in the feed. As such, this spread can be used to determine possible alternative flue gas streams to which this carbon capture technology can be applied. This commercial perspective forms an outlook for future studies, for which also some flue gas treatment technologies have been proposed.

In conclusion, this thesis researched, implemented, and validated an improvement on a dynamic VSA model. This model has been used as a tool to study the relevance and effects of different system parameters which, provided the means to design a VSA system to meet the initial performance criteria. Overall, this study contributes to HyGear's broader goal of providing sustainable blue hydrogen.

7 Discussion and Recommendations

A dynamic VSA model has been used and tested extensively throughout this thesis, although, there are still points of discussion and possible improvements to be made in future research. The desorption pressures of interest have been identified through, the parameter study and the implementation of the equalization phase was successful. However, at these low near-vacuum pressures the solver's stability is challenged because the pressure, loading, and concentration ratios of impurities start to approach zero. Despite the fact that increasing the number of cells and optimizing the relative and absolute tolerances improves solver stability, it is interesting to look into other methods as well. Suggested methods for numerical stability are the use of different solvers. For example, it was found that for steep isotherms (in the case of zeoite or high water contents) the former Kvaerno4 solver could be best replaced with the RadauIIA5 solver with an optimized maximum time stamp (dtmax=0.15 up to 1.2 depending on the stiffness), which copes better with stiff problems at the cost of computation time. On the other hand, for less stiff problems it was found that Kvaerno5 had the least stability issues and fastest computation time.

Besides model development, further integration with process simulation tools such as DWSIM could proof useful in the process equipment design process. Integrating the model in a full flowsheet analysis gives a better picture of the process and recycle streams which need to analyzed. These are important aspects to look into before heading into the a realization of a design. In ding so, also the economic analysis may be refined. Currently this analysis is based on a number of assumptions and cost relations obtained in available literature. Consequently an uncertainty margin of 25% is used for the final capturing cost and sensitivity studies. These values could be confirmed through contact with suppliers, and new economic parameters can be included in future economic analyses. For example the cost comparison could be expanded with the increased income from the carbon credits as well as the worth gained in producing blue hydrogen as oppose to grey hydrogen. Furthermore, future studies could focus on quantifying adsorbent degradation and more detailed process equipment designs to improve the economic analysis. Although it was found that the adsorbent material is not a significant cost factor, it is important to know when to replace the adsorbent to maintain the system's performance.

Furthermore, during the optimization process the adsorption duration was limited, minimizing breakthrough, to maintain CO_2 recovery. The feed velocities of both stages are kept similar to allow for scalability. In practice feed velocity and cycle times are also optimized in terms of process planning, to allow smooth operation and minimize idle/down time. As such this is another topic that could be looked into. A more detailed process planning will also give better estimations on the number of cycles that can be made in the system's lifespan, which greatly influences the total capturing costs.

Verification of the obtained results is also another matter of interest, that could be done through experimental studies. It is essential to validate the predicted equalization pressure relation, since this determines whether or not the final design requires more than 1 equalization step. In addition, it is also of interest to analyze the adsorption of water on Ze13X in more detail because this diminishes the CO_2 adsorption capacity. This research showed that any significant adsorption onto the adsorbent material should be avoided, although, experiments might also showcase that Ze13X can handle H_2O-loading up to a certain extent. Lastly, research can be dedicated to gas treatment processes to remove NO_x and SO_x via the simultaneous or stage-wise adsorption process that shortly have been discussed in Appendix A.4.

All in all, this research continues the development of a vacuum swing adsorption system to capture CO_2 from HyGear's SMR flue gas stream. Future designs can be optimized for a more realistic representation of the system, which will provide the next step towards successful implementation of a carbon capture installation in HyGear's SMR technology.

Nomenclature

Symbol	**Description**	**Unit**
Greek		
α	Dimensionless mass transfer coefficient	-
β	Fitting parameter in capillary condensation	-
χ	Selectivity	-
δ	Tolerance	-
ϵ	Void fraction	-
ϵ^{eq}	Relative mass balance error	-
η	Compression efficiency	-
γ	Adiabatic constant	-
γ_{cc}	Fitting parameter in capillary condensation	-
μ	Viscosity	kg m^{-1} s^{-1}
Ω	Dimensionless grouped energy balance term	-
ϕ	Relative humidity	-
Π	Dimensionless grouped energy balance term	-
ψ	Dimensionless grouped mass balance term	-
ρ	Density	kg m^{-3}
σ	Dimensionless energy balance term	-
τ	Dimensionless time	-
τ’	Turtrosity	-
θ	Fraction of available sites	-
ζ	Fitting parameter in capillary condensation	-
Latin		
A	Area	m^2
b	Ratio of rate constants	-
c	Adsorbate gaseous concentration	mol/m^3
C	Equalization pressure adjustment factor	-
$\mathrm{C_p}$	Specific heat capacity	J kg^{-1} K^{-1}
D	Diameter	m
$\mathrm{D_m}$	Molecular diffusivity	m^2 s^{-1}
f	Sensitivity factor	-
H	Enthalpy	J mol^{-1}
h	Heat transfer coefficient	J m^{-2} K^{-1} s
$\mathrm{K_w}$	Thermal conductivity of the wall	J m^{-1} K^{-1} s^{-1}
$\mathrm{K_z}$	Effective gas thermal conductivity	J m^{-1} K^{-1} s^{-1}
L	Length	m
N	Number of cells	-
n	Amount of moles	mol
P	Pressure	Pa
$\bar{P}$	Dimensionless pressure	-
Pe	Peclet number	-
q	Adsorbent loading	mol/kg
q^*	Equilibrium adsorbent loading	mol/kg
R	Universal gas constant	Pa m^3 mol^{-1} K^{-1}
r	Radius	m
T	Column temperature	K
$\bar{T}$	Dimensionless temperature	-
t	Time	s
U	Internal energy	J/mol
V	Column Volume	m^3
v	Local velocity	m/s

$\bar{v}$	Dimensionless local velocity	-
x	Dimensionless adsorbent loading	-
x^*	Dimensionless equilibrium adsorbent loading	-
y	gaseous mole fraction	-
z	Bed coordinate	m
Subscripts		
0	Reference value for normalization	-
ads	Adsorption	-
bd	Blowdown	-
cc	Capillary condensation	-
des	Desorption	-
eq	Equalization	-
eq,d	Equalization down / depressurization	-
eq,u	Equalization up / pressurization	-
evac	Evacuation / Desorption	-
HP	High pressure	-
i	Index for species i	-
j	Index of cell volume	-
LP	Low pressure	-
p	Particle	-
press	Re-pressurization	-
w	Wall	-

References

[1] H. Ritchie, P. Rosado, and M. Roser, "Breakdown of carbon dioxide, methane and nitrous oxide emissions by sector," *Our World in Data*, 2020, https://ourworldindata.org/emissions-by-sector.

[2] "Net zero by 2050; a roadmap for the global energy sector," International Energy Agency, Tech. Rep., 2021.

[3] "Deployment of beccs/u value chains - technological pathways, policy optins and business models," *IEA Bioenergy, Technology Collaboration Programme*, accessed on 25-09-2024. DOI: `https://www.ieabioenergy.com`.

[4] I.-T. Chen, "Steam reforming of methane," *Stanford University*, Accessed on 25-09-2024.

[5] "Steam reforming of methane in a membrane reactor: An indurstial case study," *Inudstrial & Engineering Chemistry Research*, 2006.

[6] G. Collodi, "Hydrogen production via steam reforming with co2 capture," *Chemical Engineering Transactions*, vol. 19, pp. 37–42, Apr. 2010. DOI: `10.3303/CET1019007`.

[7] M. Katebah, M. Al-Rawashdeh, and P. Linke, "Analysis of hydrogen production costs in steam-methane reforming considering integration with electrolysis and co2 capture," *Cleaner Engineering and Technology*, vol. 10, p. 100 552, 2022, ISSN: 2666-7908. DOI: `https://doi.org/10.1016/j.clet.2022.100552`.

[8] "Emissions trading worldwide: 2024 icap status report," *International Carbon Action Partnership*, April 2024.

[9] C. Voss, "Co_2 removal by psa: An industrial view on opportunities and challenges," *Springer*, 2013.

[10] G. Collodi, "Hydrogen production via steam reforming with co2 capture," *Chemical Engineering Transactions*, vol. 19, pp. 37–42, Apr. 2010. DOI: `10.3303/CET1019007`.

[11] A. Mukherjee, J. A. Okolie, A. Abdelrasoul, C. Niu, and A. K. Dalai, "Review of post-combustion carbon dioxide capture technologies using activated carbon," *Journal of Environmental Sciences*, vol. 83, pp. 46–63, 2019, ISSN: 1001-0742. DOI: `https://doi.org/10.1016/j.jes.2019.03.014`.

[12] D. D'Alessandro, B. Smit, and J. Long, "Carbon dioxide capture: Prospects for new materials," *Angewandte Chemie International Edition*, vol. 49, no. 35, pp. 6058–6082, 2010. DOI: `https://doi.org/10.1002/anie.201000431`.

[13] G. Mittal, V. Dhand, K. Y. Rhee, S.-J. Park, and W. R. Lee, "A review on carbon nanotubes and graphene as fillers in reinforced polymer nanocomposites," *Journal of Industrial and Engineering Chemistry*, vol. 21, pp. 11–25, 2015, ISSN: 1226-086X. DOI: `https://doi.org/10.1016/j.jiec.2014.03.022`.

[14] J. Du, W. Yang, L. Xu, *et al.*, "Review on post-combustion co2 capture by amine blended solvents and aqueous ammonia," *Chemical Engineering Journal*, vol. 488, p. 150 954, 2024, ISSN: 1385-8947. DOI: `https://doi.org/10.1016/j.cej.2024.150954`.

[15] C. Gouedard, D. Picq, F. Launay, and P.-L. Carrette, "Amine degradation in co2 capture. i. a review," *International Journal of Greenhouse Gas Control*, vol. 10, pp. 244–270, 2012, ISSN: 1750-5836. DOI: `https://doi.org/10.1016/j.ijggc.2012.06.015`.

[16] R. Cockeril, *Hygear signs long-term hydrogen supply contract with saint gobain*, Accessed on 25-09-2024.

[17] G. Ji and M. Zhao, "Membrane separation technology in carbon capture," in *Recent Advances in Carbon Capture and Storage*, Y. Yun, Ed., Rijeka: IntechOpen, 2017, ch. 3. DOI: `10.5772/65723`.

[18] J. Wilcox, *Carbon Capture - 5. Membrane Technology*. Springer, 2012.

[19] J. Wilcox, *Carbon Capture - 4. Adsorption*. Springer, 2012.

[20] W. J. Thomas and B. Crittenden, “2 - adsorbents,” in *Adsorption Technology & Design*, W. J. Thomas and B. Crittenden, Eds., Oxford: Butterworth-Heinemann, 1998, pp. 8–30, ISBN: 978-0-7506-1959-2. DOI: https://doi.org/10.1016/B978-075061959-2/50003-3.

[21] A. Gabelman, “Adsorption basics: Part 1,” *American Institute of Chemical Engineers*, 2017.

[22] K. Sing, “Reporting physisorption data for gas/solid systems,” in *Handbook of Heterogeneous Catalysis*, IUPAC, 2008.

[23] A. Centineo and S. Brandani, “Measurement of water vapor adsorption isotherms in mesoporous materials using the zero length column technique,” *Chemical Engineering Science*, vol. 214, p. 115 417, 2020, ISSN: 0009-2509. DOI: https://doi.org/10.1016/j.ces.2019.115417.

[24] Y. Mochizuki, J. Bud, E. Byambajav, and N. Tsubouchi, “Pore properties and co2 adsorption performance of activated carbon prepared from various carbonaceous materials,” *Carbon Resources Conversion*, p. 100 237, 2024, ISSN: 2588-9133. DOI: https://doi.org/10.1016/j.crcon.2024.100237.

[25] B. Dziejarski, J. Serafin, K. Andersson, and R. Krzyżyńska, “Co2 capture materials: A review of current trends and future challenges,” *Materials Today Sustainability*, vol. 24, p. 100 483, 2023, ISSN: 2589-2347. DOI: https://doi.org/10.1016/j.mtsust.2023.100483.

[26] A. Shamiri and M. S. Shafeeyan, “Evaluation of adsorbent materials for carbon dioxide capture,” *Materialwissenschaft und Werkstofftechnik*, vol. 53, no. 11, pp. 1392–1409, 2022. DOI: https://doi.org/10.1002/mawe.202100332.

[27] *Pressure Swing Adsorption*. Wiley-VCH, 1994.

[28] B. Ramani, “Development of a dynamic mult-bed pressure swing adsorption process for high purity hydrogen production from coke oven gas: A mathematical modeling approach,” M.S. thesis, Process, Energy (Mechanical, Maritime, and Materials Engineering), 2016.

[29] A. Boonchuay and P. Worathanakul, “The diffusion behavior of co2 adsorption from a co2/n2 gas mixture on zeolite 5a in a fixed-bed column,” *Atmosphere*, vol. 13, no. 4, 2022, ISSN: 2073-4433. DOI: 10.3390/atmos13040513.

[30] F. V. S. Lopes, “New pressure swing adsorption cycles for hydrogen purification from steam reforming off-gases,” 2010. [Online]. Available: https://api.semanticscholar.org/CorpusID:92930049.

[31] H. Swenson and N. P. Stadie, “Langmuir’s theory of adsorption: A centennial review,” *Langmuir*, vol. 35, no. 16, pp. 5409–5426, 2019, PMID: 30912949. DOI: 10.1021/acs.langmuir.9b00154.

[32] Y. Y. You and X. J. Liu, “Modeling of co2 adsorption and recovery from wet flue gas by using activated carbon,” *Chemical Engineering Journal*, vol. 369, pp. 672–685, 2019, ISSN: 1385-8947. DOI: https://doi.org/10.1016/j.cej.2019.03.118.

[33] “Optimization of two-stage pressure/vacuum swing adsorption with variable dehydration level for postcombustion carbon capture,” *Industrial & Engineering Chemistry Research*, vol. 55, no. 12, pp. 3338–3350, 2016. DOI: 10.1021/acs.iecr.5b03122.

[34] R. Haghpanah, A. Majumder, R. Nilam, *et al.*, “Multiobjective optimization of a four-step adsorption process for postcombustion co2 capture via finite volume simulation,” *Industrial & Engineering Chemistry Research*, vol. 52, no. 11, pp. 4249–4265, 2013. DOI: 10.1021/ie302658y.

[35] “Cycle synthesis and optimization of a vsa process forpostcombustion co_2 capture,” *American Institute of Chemical Engineers*, 2013.

[36] “Co2 capture by vacuum swing adsorption: Role of multiple pressure equalization steps,” *Adsorption*, vol. 21, pp. 509–522, 2015.

[37] N. Casas, J. Schell, L. Joss, and M. Mazzotti, “A parametric study of a psa process for pre-combustion co2 capture,” *Separation and Purification Technology*, vol. 104, pp. 183–192, 2013, ISSN: 1383-5866. DOI: https://doi.org/10.1016/j.seppur.2012.11.018.

[38] S. Krishnamurthy, R. Haghpanah, A. Rajendran, and S. Farooq, "Simulation and optimization of a dual-adsorbent, two-bed vacuum swing adsorption process for co2 capture from wet flue gas," *Industrial & Engineering Chemistry Research*, vol. 53, no. 37, pp. 14 462–14 473, 2014. DOI: 10.1021/ie5024723.

[39] K. T. Leperi, R. Q. Snurr, and F. You, "Optimization of two-stage pressure/vacuum swing adsorption with variable dehydration level for postcombustion carbon capture," *Industrial & Engineering Chemistry Research*, vol. 55, no. 12, pp. 3338–3350, 2016. DOI: 10.1021/acs.iecr.5b03122.

[40] C. Shen, Z. Liu, P. Li, and J. Yu, "Two-stage vpsa process for co2 capture from flue gas using activated carbon beads," *Industrial & Engineering Chemistry Research*, vol. 51, no. 13, pp. 5011–5021, 2012. DOI: 10.1021/ie202097y.

[41] Y. Takakura, S. Sugimoto, J. Fujiki, H. Kajiro, T. Yajima, and Y. Kawajiri, "Model-based analysis of a highly efficient co2 separation process using flexible metal–organic frameworks with isotherm hysteresis," *ACS Sustainable Chemistry & Engineering*, vol. 10, no. 45, pp. 14 935–14 947, 2022. DOI: 10.1021/acssuschemeng.2c05058.

[42] A. Kværnø, "Singly diagonally implicit runge–kutta methods with an explicit first stage," *BIT Numerical Mathematics*, vol. 44, no. 3, pp. 489–502, 2004.

[43] J. A. Delgado and A. Rodrigues, "Analysis of the boundary conditions for the simulation of the pressure equalization step in psa cycles," *Chemical Engineering Science*, vol. 63, no. 18, pp. 4452–4463, 2008, ISSN: 0009-2509. DOI: https://doi.org/10.1016/j.ces.2008.06.016.

[44] K. Warmuzinski and M. Tanczyk, "Calculation of the equalization pressure in psa systems," *Chemical Engineering Science*, vol. 58, no. 14, pp. 3285–3289, 2003, ISSN: 0009-2509. DOI: https://doi.org/10.1016/S0009-2509(03)00170-2.

[45] J. A. Delgado and A. Rodrigues, "Analysis of the boundary conditions for the simulation of the pressure equalization step in psa cycles," *Chemical Engineering Science*, vol. 63, no. 18, pp. 4452–4463, 2008, ISSN: 0009-2509. DOI: https://doi.org/10.1016/j.ces.2008.06.016.

[46] N. Susarla, R. Haghpanah, I. Karimi, *et al.*, "Energy and cost estimates for capturing co2 from a dry flue gas using pressure/vacuum swing adsorption," *Chemical Engineering Research and Design*, vol. 102, pp. 354–367, 2015, ISSN: 0263-8762. DOI: https://doi.org/10.1016/j.cherd.2015.06.033.

[47] M. H. Zarghampoor, M. Mozaffarian, M. Soleimani, and M. Takht Ravanchi, "Modeling of co2 adsorption on activated carbon and 13x zeolite via vacuum swing adsorption," *IOP Conference Series: Materials Science and Engineering*, vol. 206, no. 1, p. 012 004, Jun. 2017. DOI: 10.1088/1757-899X/206/1/012004. [Online]. Available: https://dx.doi.org/10.1088/1757-899X/206/1/012004.

[48] N. S. Wilkins, J. A. Sawada, and A. Rajendran, "Measurement of competitive CO_2 and H_2O adsorption on zeolite 13x for post-combustion CO_2 capture," *Adsorption*, vol. 26, no. 5, pp. 765–779, 2020. DOI: 10.1007/s10450-020-00199-3.

[49] H. Ahn and C.-H. Lee, "Effects of capillary condensation on adsorption and thermal desorption dynamics of water in zeolite 13x and layered beds," *Chemical Engineering Science*, vol. 59, no. 13, pp. 2727–2743, 2004, ISSN: 0009-2509. DOI: https://doi.org/10.1016/j.ces.2004.04.011.

[50] G. Li, P. Xiao, P. Webley, J. Zhang, R. Singh, and M. Marshall, "Capture of co2 from high humidity flue gas by vacuum swing adsorption with zeolite 13x," *Adsorption*, vol. 14, no. 2, pp. 415–422, Jun. 2008, ISSN: 1572-8757. DOI: 10.1007/s10450-007-9100-y.

[51] G. N. Nikolaidis, E. S. Kikkinides, and M. C. Georgiadis, "An integrated two-stage p/vsa process for postcombustion co2 capture using combinations of adsorbents zeolite 13x and mg-mof-74," *Industrial & Engineering Chemistry Research*, vol. 56, no. 4, pp. 974–988, 2017. DOI: 10.1021/acs.iecr.6b04270.

[52] E. V. .-. A. C. Group, *Vacuum solutions for carbon capture technologies*, Accessed on 14-02-2025.

[53] H. P. Loh, J. Lyons, and C. W. White, “Process equipment cost estimation, final report,” National Energy Technology Lab. (NETL), Morgantown, WV (United States), Tech. Rep., Jan. 2002. DOI: 10.2172/797810.

[54] R. Sinnott and G. Towler, “Chapter 10 - equipment selection, specification and design,” in *Chemical Engineering Design (Sixth Edition)*, ser. Chemical Engineering Series, R. Sinnott and G. Towler, Eds., Sixth Edition, Butterworth-Heinemann, 2020, pp. 525–644, ISBN: 978-0-08-102599-4.

[55] R. Sinnott and G. Towler, “Chapter 6 - costing and project evaluation,” in *Chemical Engineering Design (Sixth Edition)*, ser. Chemical Engineering Series, R. Sinnott and G. Towler, Eds., Sixth Edition, Butterworth-Heinemann, 2020, pp. 275–369, ISBN: 978-0-08-102599-4.

[56] *Zakelijke energietarieven - grootverbruik energie*, Accessed on 24-03-2025. [Online]. Available: https://zakelijkeenergietarieven.nl/grootverbruik-energie/prijs-per-kwh-elektriciteit/.

[57] N. Susarla, R. Haghpanah, I. Karimi, *et al.*, “Energy and cost estimates for capturing co2 from a dry flue gas using pressure/vacuum swing adsorption,” *Chemical Engineering Research and Design*, vol. 102, pp. 354–367, 2015, ISSN: 0263-8762. DOI: https://doi.org/10.1016/j.cherd.2015.06.033.

[58] R. Haghpanah, A. Majumder, R. Nilam, *et al.*, “Multiobjective optimization of a four-step adsorption process for postcombustion co2 capture via finite volume simulation,” *Industrial & Engineering Chemistry Research*, vol. 52, no. 11, pp. 4249–4265, 2013. DOI: 10.1021/ie302658y.

[59] A. Khabra, G. A. Pinhasi, and T. Zidki, “Nox and sox flue gas treatment system based on sulfur-enriched organic oil in water emulsion,” *ACS Omega*, vol. 6, no. 4, pp. 2570–2575, 2021, PMID: 33553875. DOI: 10.1021/acsomega.0c04485.

[60] “Treatment of flue gas in a co2 capture pilot plant for a commercial cfb boiler,” *Energies*, vol. 14, no. 9, 2021, ISSN: 1996-1073. DOI: 10.3390/en14092458. [Online]. Available: https://www.mdpi.com/1996-1073/14/9/2458.

[61] F. Rezaei, A. A. Rownaghi, S. Monjezi, R. P. Lively, and C. W. Jones, “Sox/nox removal from flue gas streams by solid adsorbents: A review of current challenges and future directions,” *Energy & Fuels*, vol. 29, no. 9, pp. 5467–5486, 2015. DOI: 10.1021/acs.energyfuels.5b01286.

[62] I.-C. Marcu and S. IOAN, “Study of sulfur dioxide adsorption on y zeolite,” *Journal of the Serbian Chemical Society*, vol. 69, pp. 563–569, Jul. 2004. DOI: 10.2298/JSC0407563M.

[63] *Chemical Engineering Volume 2: Particle technology adn Separation Processes*. Butterworth-Heinemann, 2003.

A Additional Sections

A.1 Details on HyGear's adsorption model

Two additional topics are discussed in detail to explain the added scheme to the Finite Volume Method, as well as the dimensionless groups that are used in the five main balance equations of the PSA model.

A.1.1 WENO Scheme

As mentioned, the model used for this study is based on a staggered grid approach, making sure that the scalars are stored on the cell's centers and vectors on the edges. With this approach, and the governing formulae, it becomes clear that spatial derivatives are derived through integrating over every cell and their boundaries: $j-0.5$ & $j+0.5$. This is made clear in the five main balance equations below:

Discretization of the component mass balance:

$$\frac{\partial y_{i,j}}{\partial t} = D_L \frac{T_j}{P_j}\frac{1}{\Delta z}\left(\frac{P_{j+0.5}}{T_{j+0.5}}\frac{y_{i,j+1}-y_{i,j}}{\Delta z} - \frac{P_{j-0.5}}{T_{j-0.5}}\frac{y_{i,j}-y_{i,j-1}}{\Delta z}\right) - \frac{T_j}{P_j}\frac{1}{\Delta z}\left(\frac{P_{j+0.5}}{T_{j+0.5}} y_{i,j+0.5} v_{j+0.5} - \frac{P_{j-0.5}}{T_{j-0.5}} y_{i,j-0.5} v_{j-0.5}\right) - \frac{1-\epsilon}{\epsilon}\frac{RT_j}{P_j}\frac{\partial q_{i,j}}{\partial t} - \frac{y_{i,j}}{P_j}\frac{\partial P_j}{\partial t} + \frac{y_{i,j}}{T_j}\frac{\partial T_j}{\partial t} \tag{39}$$

Discretization of the total mass balance in terms of pressure:

$$\frac{\partial P_j}{\partial t} = -T_j \frac{1}{\Delta z}\left(\frac{P_{j+0.5}}{T_{j+0.5}} v_{j+0.5} - \frac{P_{j-0.5}}{T_{j-0.5}} v_{j-0.5}\right) - \frac{1-\epsilon}{\epsilon} RT_j \sum_{i=1}^{N_{\text{comp}}} \frac{\partial x_{i,j}}{\partial t} \tag{40}$$

Discretization of the moment balance:

$$v_{j+0.5} = \frac{D_p^2}{150\mu L}\left(\frac{\epsilon}{1-\epsilon}\right)^2 \left(-\frac{P_{j+1}-P_j}{\Delta z}\right) \tag{41}$$

Discretization of the energy balance in the column:

$$\frac{\partial T_j}{\partial t} = \Omega_1 \frac{1}{\Delta z}\left(\frac{T_{j+1}-T_j}{\Delta z} - \frac{T_j - T_{j-1}}{\Delta z}\right) - \Omega_2 \frac{1}{\Delta z}\left(v_{j+0.5}P_{j+0.5} - v_{j-0.5}P_{j-0.5}\right) - \Omega_3 T \sum_{i=1}^{N_{\text{comp}}} \frac{\partial x_{i,j}}{\partial t} + \sum_{i=1}^{N_{\text{comp}}}\left(\sigma_i \frac{\partial x_{i,j}}{\partial t}\right) - \Omega_4 (T_j - T_{w,j}) - \Omega_2 \frac{\partial P_j}{\partial t} \tag{42}$$

Discretization of of the energy balance for the column wall:

$$\frac{\partial T_{w,j}}{\partial t} = \Pi_1 \frac{1}{\Delta z}\left(\frac{T_{w,j+1}-T_{w,j}}{\Delta z} - \frac{T_{w,j}-T_{w,j-1}}{\Delta z}\right) + \Pi_2 (T_j - T_{w,j}) - \Pi_3 (T_{w,j} - T_{amb}) \tag{43}$$

From the discretization of the governing balance equations can be seen that scalar quantities are also accessible on the cell boundaries. This is achieved using a weighted essentially non-oscillatory (WENO) interpolation scheme, a method integrated in the finite volume method (FVM) to dampen non-physical oscillations around sharp concentration fronts, that propagate through the column, to maintain accuracy[58]. This scheme relation is written as:

$$f_{j+0.5} = \frac{\alpha_{0,j}}{\alpha_{0,j}+\alpha_{1,j}}\left(\frac{1}{2}(f_j + f_{j+1})\right) + \frac{\alpha_{1,j}}{\alpha_{0,j}+\alpha_{1,j}}\left(\frac{3}{2} f_j - \frac{1}{2} f_{j-1}\right) \tag{44}$$

Where $\alpha_{0,j}$ and $\alpha_{1,j}$ are written as:

$$\alpha_{0,j} = \frac{2/3}{(f_j + 1 - f_j + \delta)^4} \tag{45}$$

$$\alpha_{1,j} = \frac{1/3}{(f_j - f_{j-1} + \delta)^4} \tag{46}$$

This approach allows the balance equations to be readily calculated at the cell boundaries. On the other hand, at the ends of the column there is no available data for the interpolation. In other words, to interpolate to $j = 1$ and $j = N$ there is information required at $j = 0$ and $j = N+1$ that is missing. this is solved with a half-cell approximation:

$$f_1 - f_0 = 2(f_1 - f_{0.5}) \tag{47}$$

$$f_{N+1} - f_N = 2(f_{N+0.5} - f_N) \tag{48}$$

A.1.2 Dimensionless Groups

Besides the dimensionless variables for pressure, temperature, loading, velocity, and mass transfer coefficient, the governing equations make use of a number of dimensionless groups that are specified below.

Dimensionless variables:

$$\bar{P} = \frac{P}{P_0}, \quad \bar{T} = \frac{T}{T_0}, \quad \bar{T}_w = \frac{T_w}{T_0}, \quad \bar{T}_{amb} = \frac{T_{amb}}{T_0}, \quad \bar{x}_i = \frac{q_i}{q_{s,0}}, \quad \bar{v} = \frac{v}{v_0}, \quad \alpha_i = \frac{k_i L}{v_0} \tag{49}$$

Dimensionless groups:

$$P_e = \frac{v_0 L}{0.7 D_m + 0.5 v_0 D_p} \tag{50}$$

$$P_{eh} = \frac{\epsilon v_0 L}{\frac{K_z}{\rho_g C_{p,g}}} \tag{51}$$

$$\psi = \frac{R T_0 q_{s,0}}{P_0} \frac{1-\epsilon}{\epsilon} \tag{52}$$

$$\Omega_1 = \frac{\frac{K_z}{v_0 \epsilon L}}{\frac{1-\epsilon}{\epsilon}\left(\rho_s C_{p,s} + q_{s,0} C_{p,a} \sum_{i=1}^{n_{comp}} x_i\right)} \tag{53}$$

$$\Omega_2 = \frac{\frac{C_{p,a}}{R}\frac{P_0}{T_0}}{\frac{1-\epsilon}{\epsilon}\left(\rho_s C_{p,s} + q_{s,0} C_{p,a} \sum_{i=1}^{n_{comp}} x_i\right)} \tag{54}$$

$$\Omega_3 = \frac{C_{p,a} q_{s,0}}{\frac{1-\epsilon}{\epsilon}\left(\rho_s C_{p,s} + q_{s,0} C_{p,a} \sum_{i=1}^{n_{comp}} x_i\right)} \tag{55}$$

$$\Omega_4 = \frac{\frac{2h_{in}}{r_{in}}\frac{L}{v_0}}{\frac{1-\epsilon}{\epsilon}\left(\rho_s C_{p,s} + q_{s,0} C_{p,a} \sum_{i=1}^{n_{comp}} x_i\right)} \tag{56}$$

$$\sigma_i = \frac{\frac{q_{s,0}}{T_0}(-\Delta H_i)}{\left(\rho_s C_{p,s} + q_{s,0} C_{p,a} \sum_{i=1}^{n_{comp}} x_i\right)} \tag{57}$$

$$\Pi_1 = \frac{K_w}{\rho_w C_{p,w} v_0 L} \tag{58}$$

$$\Pi_2 = \frac{2 r_{in} h_{in}}{r_{out}^2 - r_{in}^2} \frac{L}{\rho_w C_{p,w} v_0} \tag{59}$$

$$\Pi_3 = \frac{2 r_{out} h_{out}}{r_{out}^2 - r_{in}^2} \frac{L}{\rho_w C_{p,w} v_0} \tag{60}$$

A.2 Equalization pressure derivation

Unlike blowdown cycles, equalization cycles have a fixed intermediate pressure that needs to be derived to make sure mass is conserved during the simulation. For example, if the equalization pressure is chosen to low then too much mass will be transported to the lower pressure column compared to what would happen in real life. Hence, deriving the right pressure is essential. As discussed, an iterative process is modeled to converge an initial guess to the real equalization pressure within a given tolerance. This section shows how to derive the guessed pressure for a 2-step, and, 3-step equalization cycle in the case where CO_2 is adsorbed at $P_H = 1$ bar and desorbed at $P_L = 0.1$ bar. It must be noted that these derivations do not take adsorption effects in the lower pressure bed into a count. As was shown in this study, those effects cause the equalization pressure to be lower than the average value of the two pressures.

Beginning with the 2-step equalization cycle, and knowing that the equalization pressures is the guessed as the average pressure of the equalizing columns, two equations can be derived to determine P_1 and P_2:

$$P_1 = \frac{P_H + P_2}{2} \qquad \wedge \qquad P_2 = \frac{P_1 + P_L}{2} \tag{61}$$

Substituting one in the other gives:

$$P_2 = \frac{P_H + P_2}{2} \cdot \frac{1}{2} + \frac{P_L}{2} \tag{62}$$

$$P_2 = \left(\frac{P_H}{4} + \frac{P_L}{2}\right) \cdot \frac{4}{3} \tag{63}$$

Therefore, P_2 is equal to 0.4 bar, and P_1 is 0.7 bar which can also be seen from the pressure plot shown in Figure 44. Introducing additional equalization steps allows a deeper equalization that reaches closer to the desorption pressure. Purity is increased, similar to lower blowdown pressures but maintaining recovery, and the energy consumption is decreased as a consequence.

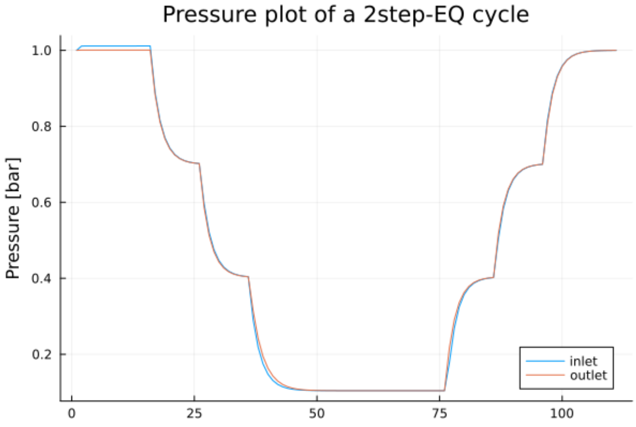

Figure 44: Pressure plot of a 2-step Equalization Cycle

This can be seen for a 3-step equalization cycle, of which the pressures, can be guessed through solving a set of 3 equations:

$$P_1 = \frac{P_H + P_2}{2} \qquad \wedge \qquad P_2 = \frac{P_1 + P_3}{2} \qquad \wedge \qquad P_3 = \frac{P_2 + P_L}{2} \tag{64}$$

Similarly, inserting substituting the first equation in the second gives:

$$P_2 = \left(\frac{P_H}{4} + \frac{P_3}{2}\right) \cdot \frac{4}{3} \tag{65}$$

Substituting the latter in the third equation gives:

$$P_3 = \left(\frac{P_H}{4} + \frac{P_3}{2}\right) \cdot \frac{4}{3} \cdot \frac{1}{2} + \frac{P_L}{2} \tag{66}$$

$$P_3 = \frac{4P_H}{24} + \frac{4P_3}{12} + \frac{P_L}{2} \tag{67}$$

$$P_3 = \left(\frac{4P_H}{24} + \frac{P_L}{2}\right) \cdot \frac{12}{8} \tag{68}$$

$$P_3 = \left(\frac{P_H}{6} + \frac{P_L}{2}\right) \cdot \frac{12}{8} \tag{69}$$

$$\tag{70}$$

As such P_3 is equal to 0.325 bar, P_2 = 0.55 bar, and P_1 is equal to 0.775 bar as shown in Figure 45. Knowing that the equalization depth went from 0.55 bar to 0.4 when using 2 equalization steps instead of 1, the result of going from 2 to 3 steps indicates a decrease in marginal impact per additional equalization step (this marginal impact continues to decrease as the depth is 0.28 bar and 0.25 bar for 4 and 5 step equalization respectively). This shows that there is a trade-off; adding equalizations steps improves the system's performance, although the benefit of each successive drops whilst the complexity and costs increase.

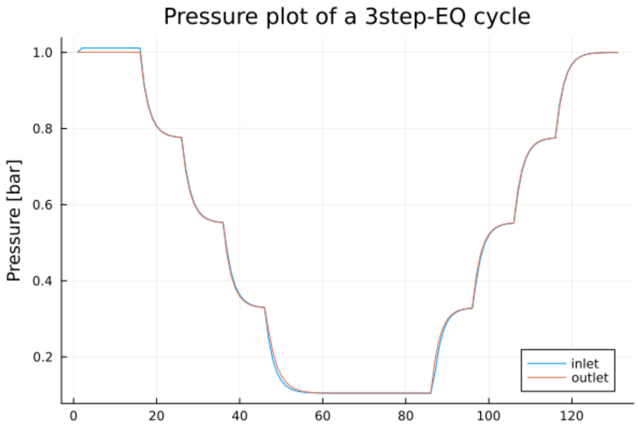

Figure 45: Pressure plot of a 3-step Equalization Cycle

A.3 Validation to reduce number of cells & cycles for each simulation

The PSA model that is used and further developed in this study uses a finite volume method, meaning that the total column is divided into a number of cells. Increasing the amount of cells increases the accuracy of the simulation, with the cost of computational power and time. Similarly, as the model solved the ODE problem a number of cycles is required in order to give a stable solution of the process. As mentioned in literature, the required number of cycles to reach steady state can vary from 40 to 400 cycles[34]. Subsequently, the required time to compute just a single solution for a parameter study can take up several hours. Therefore, time is a serious constraint for this type of research.

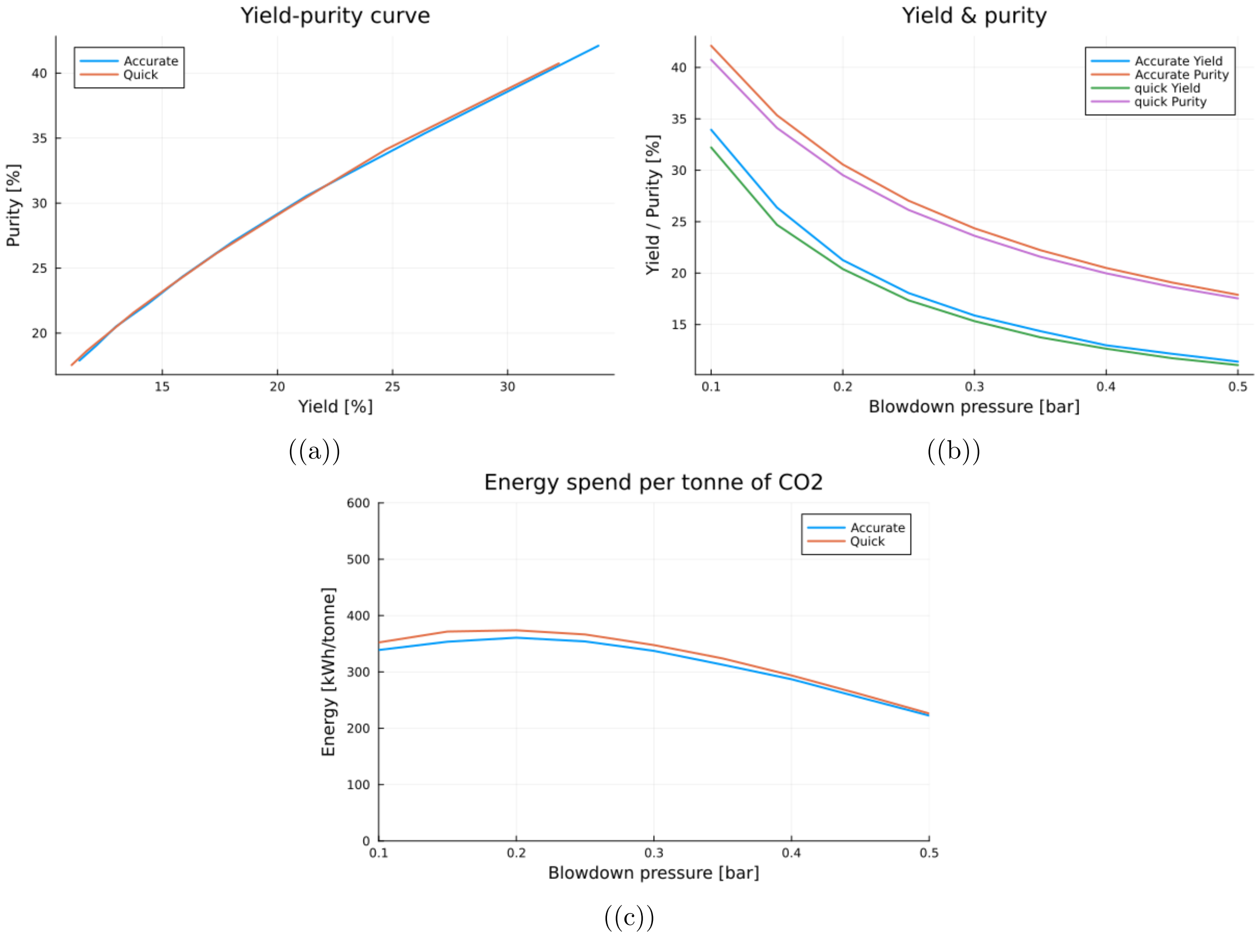

((a)) ((b))

((c))

Figure 46: Validation of simulation simplification, showing comparable results for a feed mixture of CO_2,O_2,N_2 [0.12,0.1,0.78] with an accurate simulation [16 cells, 50 cycles] and a quick simulation [8 cells, 6 cycles]

Since the primary objective is to identify a range of parameters, for which the PSA cycle is able to meet the performance indicators, the accuracy is lowered to save computational power. This is done through lowering the number of cells and cycles. Reducing the simulation accuracy requires validation, hence this has been tested and shown in Figures 46. In these results can be seen how a 30 minute simulation achieves significantly close results as that of one taking 6.25 hours. Therefore, decreasing accuracy as a means to study a broader range of parameters is validated.

A.4 Separation Methods for NO_x & SO_x treatment

Besides the carbon capture study, it is also of interest to identify suitable methods to treat NO_x and SO_x impurities in the flue gas. Researching such measures is important for the development of HyGear's blue hydrogen production technology, as well as a stand-alone carbon capture module for other flue gas types.

Typical examples of such purification technologies are Wet Flue Gas Desulfurization (FGD) and Selective Catalyc NO_x Reduction (SCR) [59]. For FGD, a solution with an alkaline chemical reagent is used to convert SO_x to either solid or liquid products. This chemical reaction can take place at low ($\leq$150 °C) and high temperatures (700-1200 °C), and the reaction can be enhanced using metal oxide or ammonia based surfaces. Regarding SCR, the technology revolves around splitting NO_x gasses to NO, N_2, and H_2O gasses at temperatures above 300°C. This is achieved using ammonia, hydrogen, or hydrocarbons on a catalyst. For both these technologies there are significant drawbacks in terms of left-over chemical (liquid) waste due to the nature of the nonregenerable nature of the process, and required process heat[60]. Therefore, implementing such measures would be counter productive to the goal of capturing CO_2 with as little energy as possible and produce sustainable blue hydrogen (in fact carbon neutral, but more sustainable then grey hydrogen).

Alternative methods are being widely researched, of which adsorption methods have gained interest and are closely bound to HyGear's expertise[61]. This also brings the possibility of expanding the current VSA model for this type of separation processes. Zeolite Y, for example, is reported as a suitable candidate for simultaneous $NO_x$and SO_x adsorption, and has been tested for a flue gas stream at comparable conditions to that of the SMR flue gas[62]. Although researched adsorbents show promising separation efficiencies, their stability in a cyclic process and optimal operating conditions are still two main challenges. The reaction kinetics are another topic of interest, because it is important for the adsorbent degradation and separation efficiency to promote reversible adsorption reactions and minimize irreversible chemical reactions with the adsorbent material. Also Activated Carbon has been researched for the SO_x and NO_2 removal. In low temperature systems, as for this context, it is preferred to adsorb these impurities in a 2 stage process because activated carbon has a greater affinity for SO_x[61]. Normally, NO_x promotes the SO_x adsorption, although, this is not the case for Activated Carbon due to the higher permanent dipole moment and polarizability of SO_2. Hybrid catalyst-adsorbent materials can also be used for simultaneous component separation, although this process remains challenging at low temperatures since the materials show more degradation effects[59]. As such, further studies could be done on solid SO_x and NO_x adsorption to asses both the feasibility of simultaneous and stage-wise adsorption as well as an adsorbent material analysis.

B Additional Figures

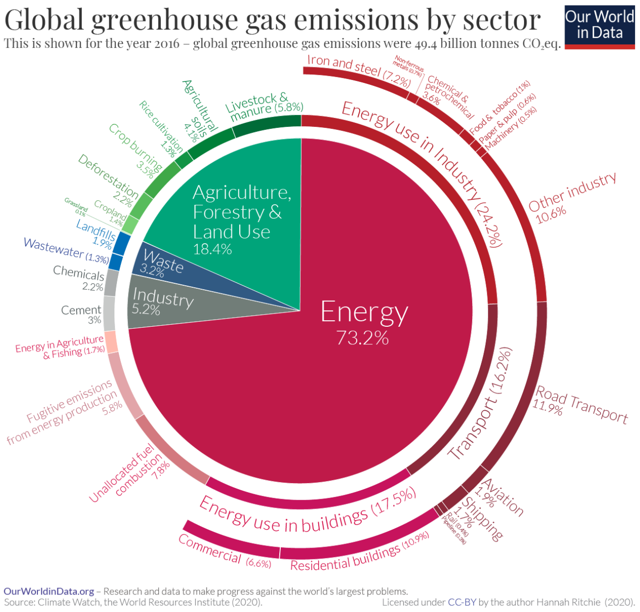

Figure 47: Overview of the global GHG emissions of 2016[1]

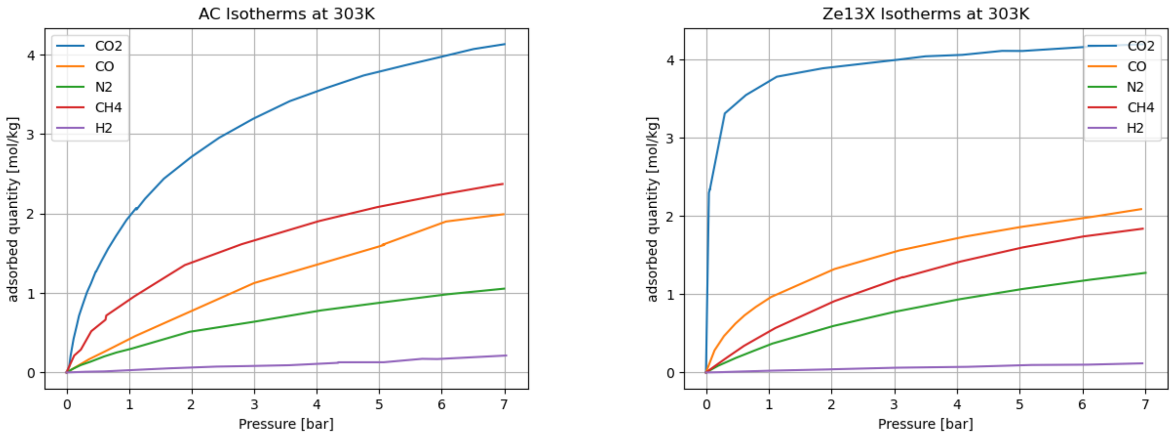

((a))

((b))

Figure 48: Isotherm adsorption loading on Activated carbon (a) and Zeolite 13X (b) at 303K for CO_2, CO, N_2, CH_4, and H_2[30]

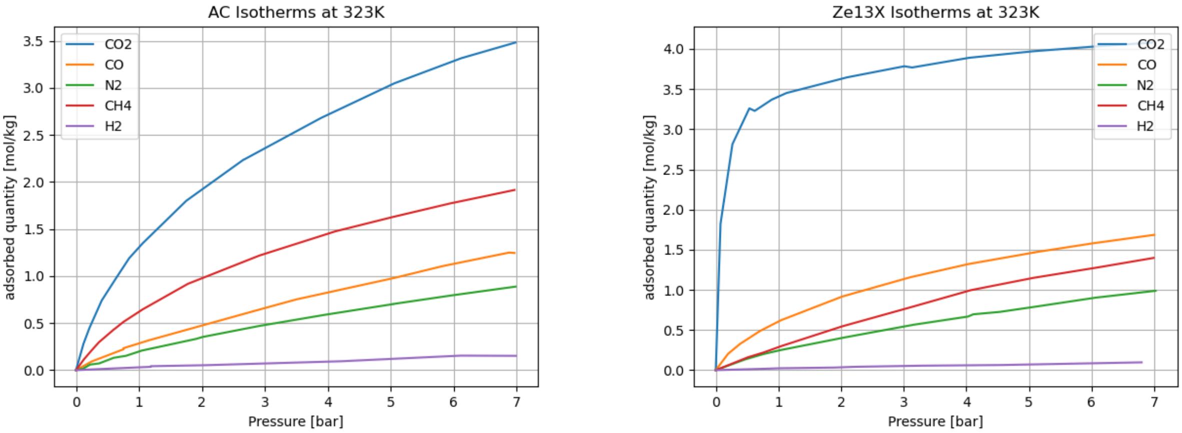

((a))

((b))

Figure 49: Isotherm adsorption loading on Activated carbon (a) and Zeolite 13X (b) at 323K for CO_2, CO, N_2, CH_4, and H_2[30]

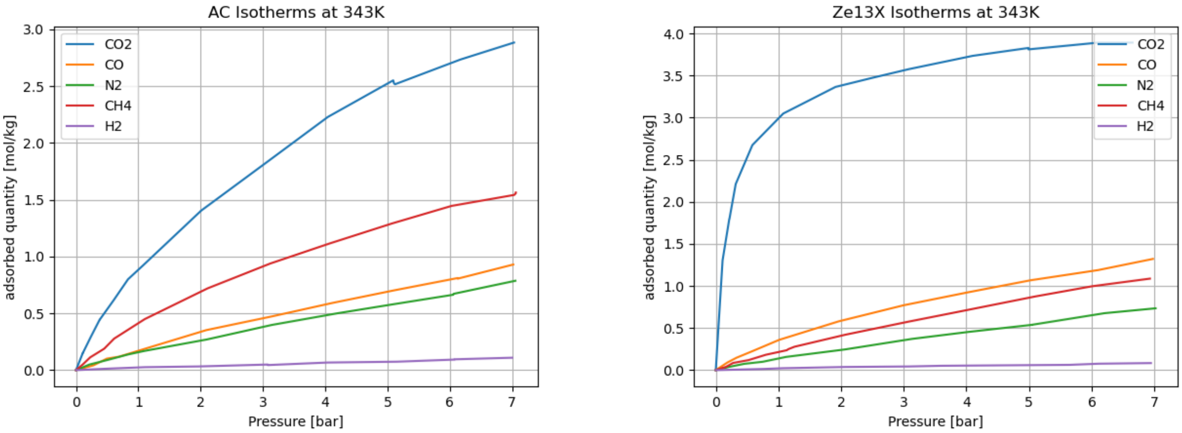

((a))

((b))

Figure 50: Isotherm adsorption loading on Activated carbon (a) and Zeolite 13X (b) at 343K for CO_2, CO, N_2, CH_4, and H_2[30]

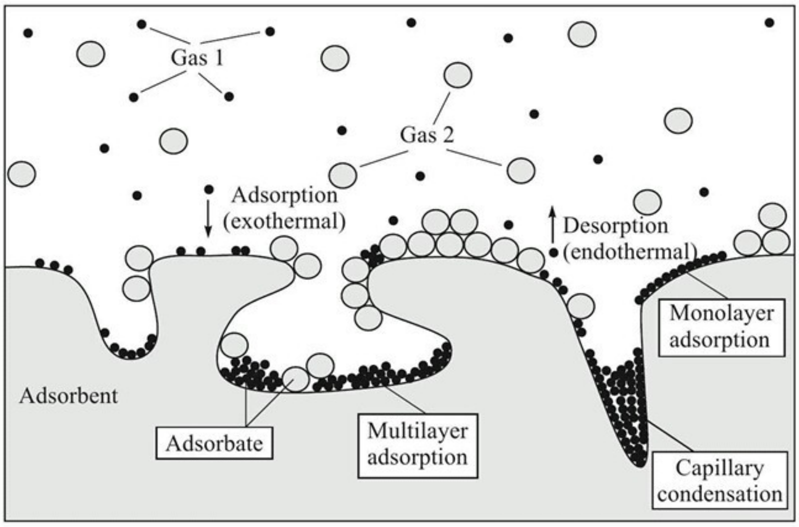

Figure 51: Visualization of the mono- and multilayer adsorption and capillary condensation processes[63]

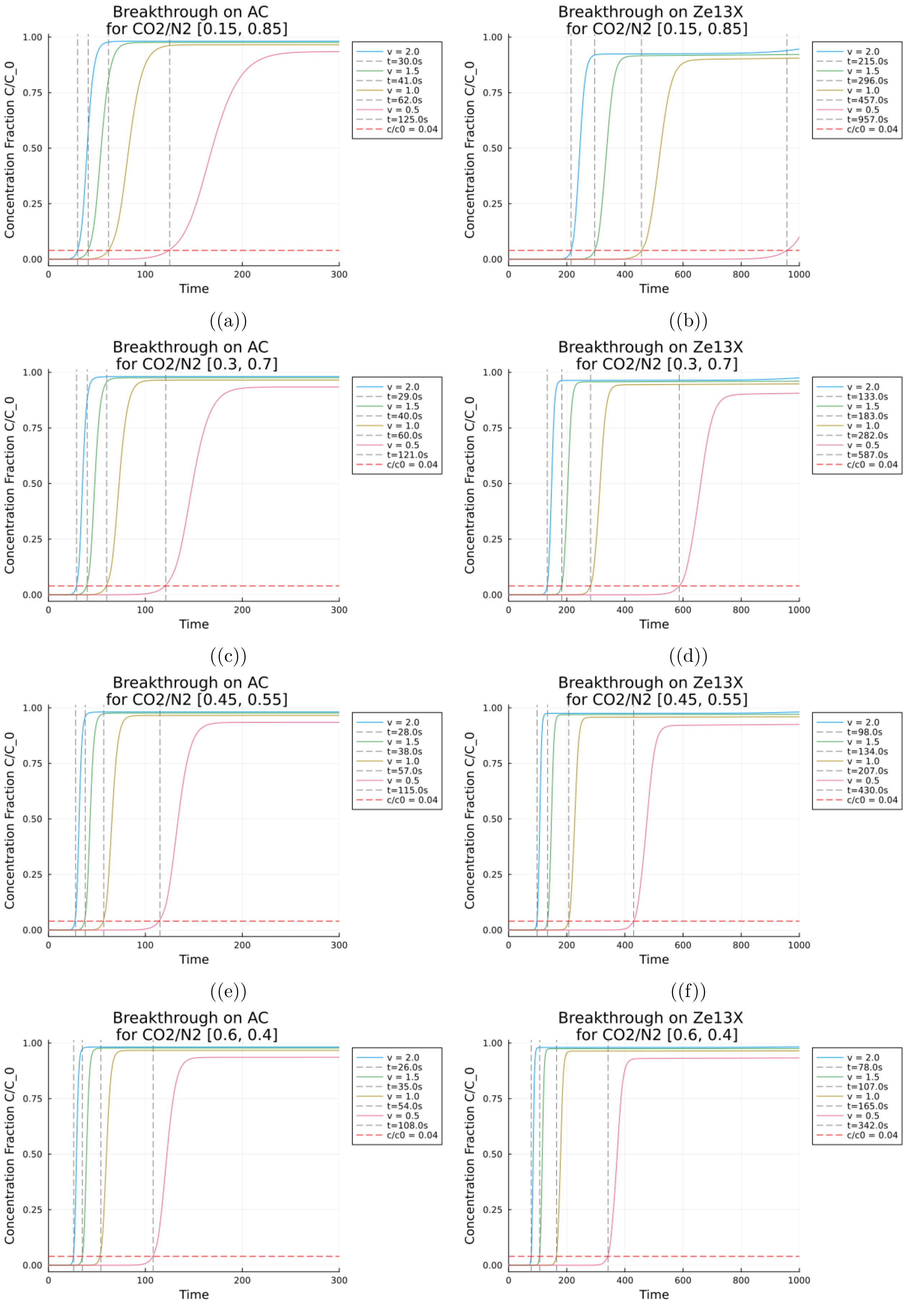

((a)) ((b))

((c)) ((d))

((e)) ((f))

((g)) ((h))

Figure 52: Effect of different feed velocities and compositions of CO_2/N_2 and their respective %4 breakthrough curves on, figures (a),(c),(e),(g) Active Carbon, and figures (b),(d),(f),(h) Zeolite 13X

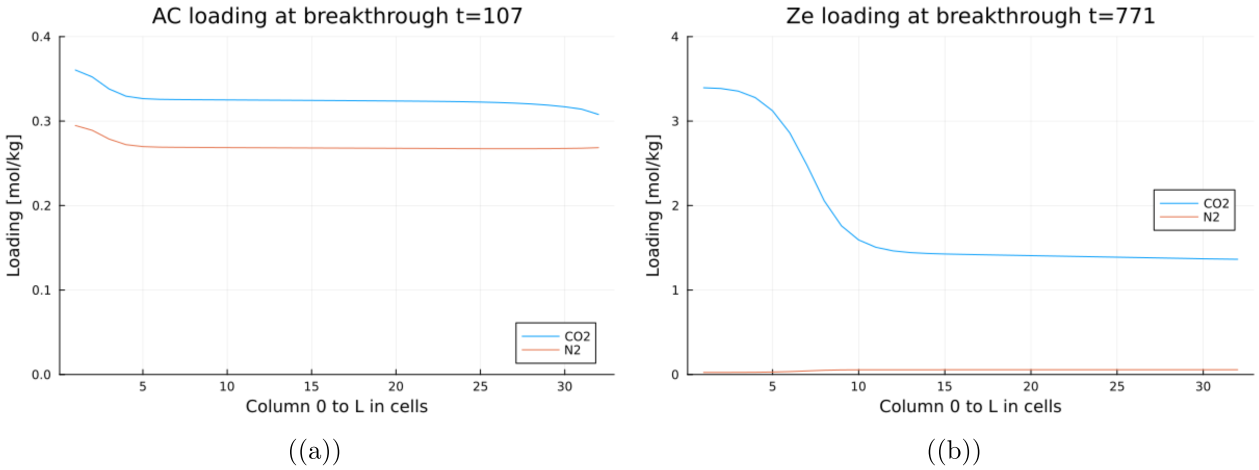

((a)) ((b))

Figure 53: Adsorbent loading on (a) Active Carbon, and (b) Zeolite 13X for the longest adsorption duration possible according to the minimum yield requirement of 80%

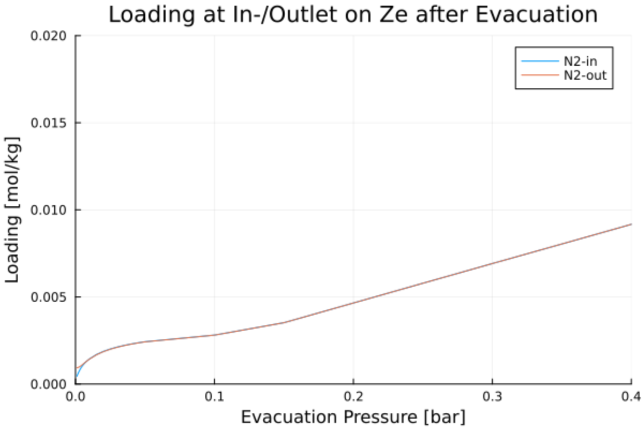

Figure 54: effect on N_2 loading on a saturated Ze13X adsorbent ben using different desorption pressures

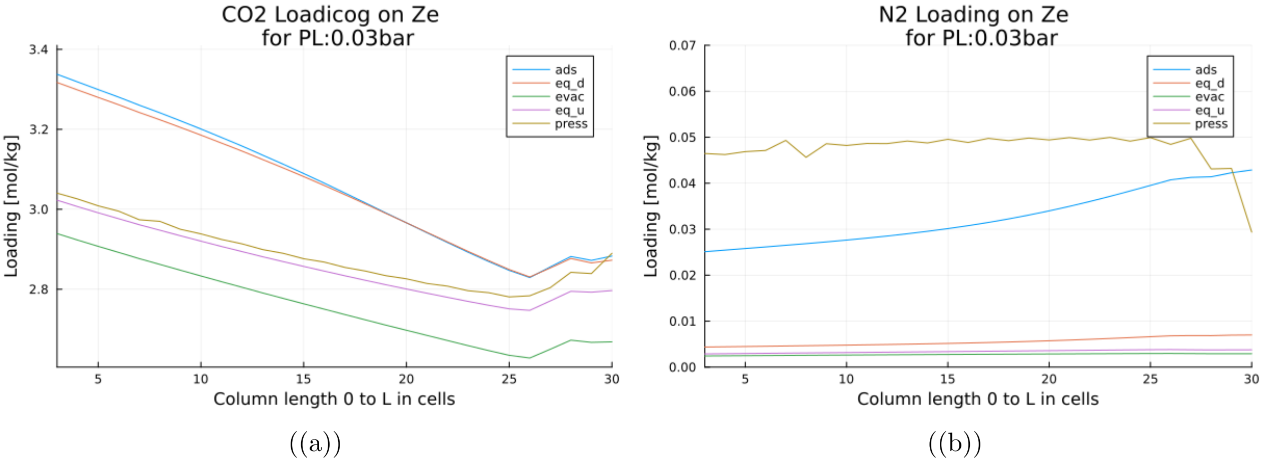

((a)) ((b))

Figure 55: Loading profiles of (a) CO_2 and (b) N_2 after adsorption, equalization, evacuation, pressurization on Ze13X using an adsorption time of 100 seconds and a desorption pressure of 0.03 bar

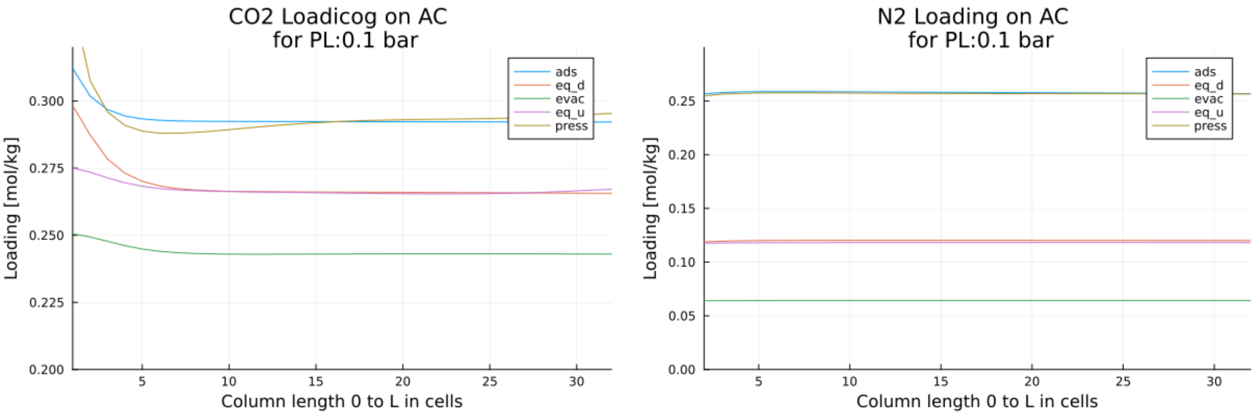

((a)) ((b))

Figure 56: Loading profiles of (a) CO_2 and (b) N_2 after adsorption, equalization, evacuation, pressurization on AC using minimized adsorption duration and a desorption pressure of 0.1 bar

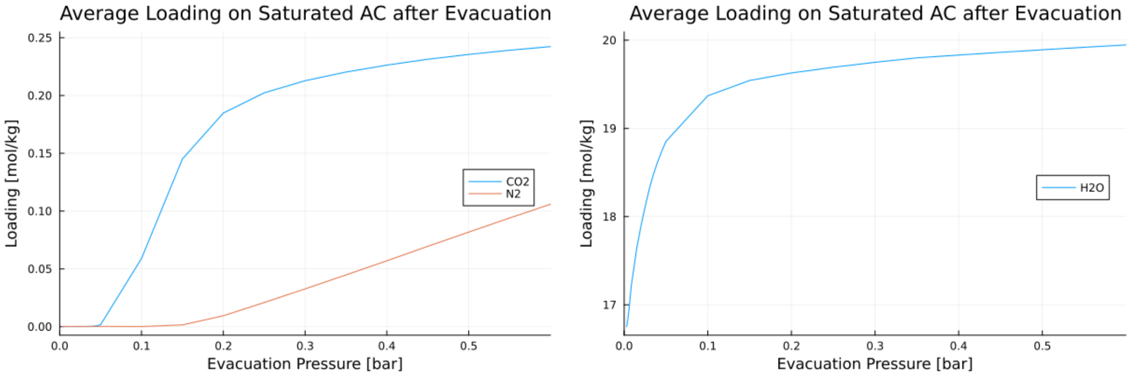

((a)) ((b))

Figure 57: Desorption analysis in humid conditions on Active Carbon, showing the reduction of (a) CO_2 and N_2 loading, (b) H_2O loading for different desorption pressures

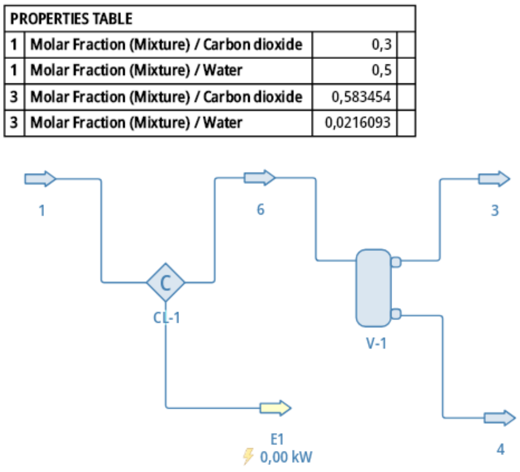

PROPERTIES TABLE

1	Molar Fraction (Mixture) / Carbon dioxide	0,3
1	Molar Fraction (Mixture) / Water	0,5
3	Molar Fraction (Mixture) / Carbon dioxide	0,583454
3	Molar Fraction (Mixture) / Water	0,0216093

Figure 58: Visualization of the flowsheet made in DWSIM to simulate the achievable water separation for a given cooling duty

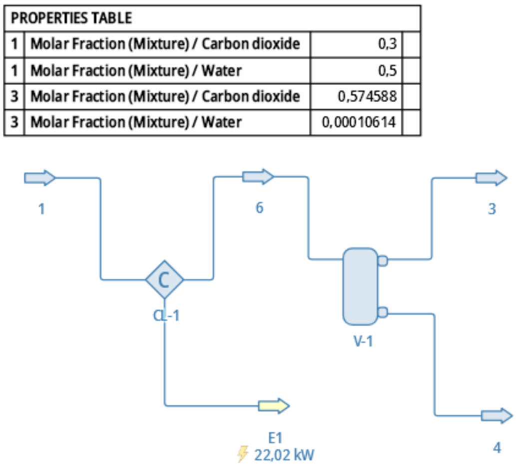

PROPERTIES TABLE		
1	Molar Fraction (Mixture) / Carbon dioxide	0,3
1	Molar Fraction (Mixture) / Water	0,5
3	Molar Fraction (Mixture) / Carbon dioxide	0,574588
3	Molar Fraction (Mixture) / Water	0,00010614

Figure 59: Visualization of the flowsheet made in DWSIM to calculate the required cooling duty to lower the water content to prevent adsorption onto the zeolite adsorbent used in the second VSA stage

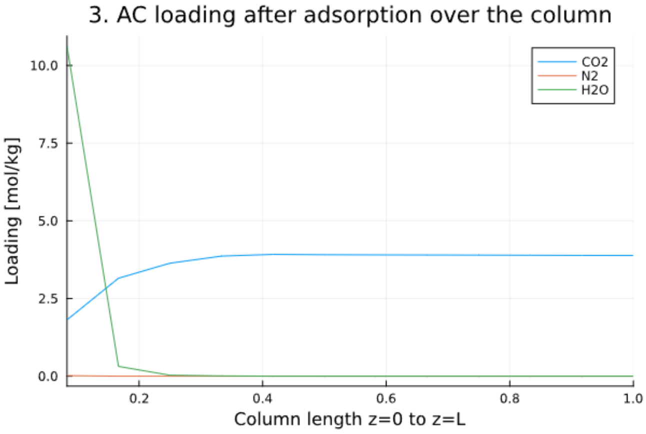

Figure 60: Loading profile on a multi-layered column after adsorption

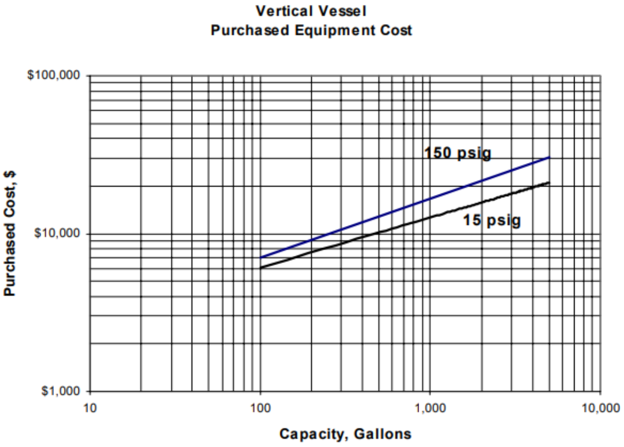

Figure 61: Cost relation for a vertical carbon steel vessel used to derive the costs of the gas-liquid separator operating at atmospheric pressure[54]

C Additional Tables

Table 9: Input parameters & operating conditions used in the dynamic VSA model, adapted from [35]

Parameter	**Value**	**Unit**
Column Settings		
L	1	m
r_{in}	0.1445	m
r_{out}	0.162	m
ϵ	0.37	-
ϵ_p	0.35	-
r_p	0.001	m
τ'	3	-
Process Properties and constants		
ρ_s (AC/Ze13X)	842/1130	kg m^{-3}
ρ_w	7800	kg m$_{-3}$
$C_{p,g}$	30.7	J mol^{-1} K^{-1}
$C_{p,a}$	30.7	J mol^{-1} K^{-1}
$C_{p,s}$	1070	J kg^{-1} K^{-1}
$C_{p,w}$	520	J kg^{-1} K^{-1}
μ	$1.72 \cdot 10^{-5}$	kg m^{-1} s^{-1}
D_m ($CO_2/N_2/H_2O$)	$1.6 / 2.1 / 2.4 \cdot 10^{-5}$	m^2 s^{-1}
γ	1.4	-
K_z	0.09	J m^{-1} K^{-1} s^{-1}
K_w	16	J m^{-1} K^{-1} s^{-1}
H_{in}	8.6	J m^{-2} K^{-1} s^{-1}
H_{out}	2.5	J m^{-2} K^{-1} s^{-1}
R	8.314	J mol^{-1} K^{-1}
Operating conditions		
P_{feed}	1	bar
P_H	1	bar
v_{feed}	0.25	m s^{-1}
T_{feed}	298.15	K
T_{amb}	299.15	K
P_0	P_H	bar
T_0	T_{feed}	K
v_0	v_{feed}	m s^{-1}

Table 10: HyGear's Dual site Langmuir adsorption parameters on Activated Carbon

	CO_2	**N_2**	**Unit**
$q_{b,m}$	1969.61	944.81	mol m^{-3}
$q_{d,m}$	1969.61	944.81	mol m^{-3}
Δ U_b	-17223.0	-16200	kJ mol^{-1}
Δ U_d	-17223.0	-16200	kJ mol^{-1}
d_0	$1.65 \cdot 10^{-5}$	$5.9064 \cdot 10^{-6}$	m^3 mol^{-1}
b_0	$1.65 \cdot 10^{-5}$	$5.9064 \cdot 10^{-6}$	m^3 mol^{-1}

Table 11: Dual site Langmuir adsorption parameters on Zeolite 13X[35],[48]

	$\mathbf{CO_2}$	$\mathbf{H_2O}$	$\mathbf{N_2}$	**Unit**
$q_{b,m}$	3491.7	5766.39	6599.2	mol m^{-3}
$q_{d,m}$	2870.2	14486.6	0	mol m^{-3}
$\Delta\ U_b$	-36641.21	-44210	-15800	kJ mol^{-1}
$\Delta\ U_d$	-35690.66	-40160	0	kJ mol^{-1}
d_0	$8.65 \cdot 10^{-7}$	$9.56 \cdot 10^{-8}$	$2.50 \cdot 10^{-6}$	m^3 mol^{-1}
b_0	$2.63 \cdot 10^{-8}$	$2.10 \cdot 10^{-5}$	$5.9064 \cdot 10^{-6}$	m^3 mol^{-1}

Table 12: Water vapor adsorption on Activated Carbon[38]

	$\mathbf{H_2O}$	**Unit**
$q_{b,m}$	15821.18	mol m^{-3}
$q_{d,m}$	0	mol m^{-3}
$\Delta\ U_b$	$-4.048 \cdot 10^4$	kJ mol^{-1}
$\Delta\ U_d$	0	kJ mol^{-1}
d_0	$5.660 \cdot 10^{-9}$	m^3 mol^{-1}
b_0	0	m^3 mol^{-1}
q_{cc}	8268.44	mol m^{-3}
β	422.1	
γ	0.03435	
ζ	0.04162	